THEORY OF TRIBOELECTRIC NANOGENERATORS FOR SELF-POWERED SYSTEMS

A Dissertation
Presented to
The Academic Faculty

by

Simiao Niu

In Partial Fulfillment
of the Requirements for the Degree
Doctor of Philosophy in the
School of Materials Science and Engineering

Georgia Institute of Technology

May 2016

THEORY OF TRIBOELECTRIC NANOGENERATORS FOR SELF-POWERED SYSTEMS

Approved by:

Dr. Zhong Lin (Z.L.) Wang, Advisor
School of Materials Science and Engineering
Georgia Institute of Technology

Dr. Russell D. Dupuis
School of Electrical and Computer Engineering
Georgia Institute of Technology

Dr. Meilin Liu
School of Materials Science and Engineering
Georgia Institute of Technology

Dr. Farrokh Ayazi
School of Electrical and Computer Engineering
Georgia Institute of Technology

Dr. John D. Cressler
School of Electrical and Computer Engineering
Georgia Institute of Technology

Date Approved: February 4th, 2016

To my beloved families and friends

ACKNOWLEDGEMENTS

First, I would like to express my sincere thanks to my Ph.D. advisor, Dr. Zhong Lin Wang, for his visional research guidance and wonderful care on my life. I still remember when I first came to the Georgia Institute of Technology, I was only 20 years old. From then on, Dr. Wang gave me his endless love, which helped me grow up both in my research and in my personal characteristics. I also want to express my sincere thanks to my committee members, including Dr. Meilin Liu, Dr. John D. Cressler, Dr. Farrokh Ayazi and Dr. Russell D. Dupuis, for their insightful advice on my doctoral research and thesis, without which the quality of this dissertation cannot be guaranteed.

It is my great honor to join Dr. Wang's research group with many kind and talented scholars. I also want to express my sincere thanks to my friends in this group. I still remember it is Dr. Youfan Hu who gave me her hand when I was frustrated during my 2nd year Ph.D. research. Without that, I may have been already given up and cannot finish this Ph.D. journey. Dr. Sihong Wang and Dr. Yusheng Zhou are two of my big brothers. I enjoyed discussing scientific research with them. I also want to share my feelings every time there is something happen and they can always give me their advice. I feel fortunate to meet Dr. Ying Liu and work with her on the development of TENG theoretical modeling method. I still remember the whole process that we have to rebuild the TENG simulation method for 4 times just for accuracy. Finally, it is really great for me to meet Dr. Xiaofeng Wang in my 4th Ph.D. year and we worked day and night to

realize the first TENG-based self-powered system. I still remember the night how we are excited when we first realized the sustainably drive of a calculator exploiting only human biomechanical energy. Besides, I would like to thank Drs. Long Lin, Fang Yi, Yannan Xie, Jianan Deng, Ying-chi Lai, Tiejun Zhang, Yong Ding, Jun Chen, Guang Zhu, Yunlong Zi, Wenzhuo Wu, Xiaonan Wen, Ruomeng Yu, Peng Bai, Shengming Li, Ken C. Pradel, Po-Kang Yang, Zong-Hong Lin, Fang Zhang, and many others, for their help in both my research and my personal life.

Last but most importantly, I would like to thank my loved ones. My parents, L. He and G. Niu, brought me up in my childhood, and also unconditionally supported me in my whole Ph.D. journey. Also my dear aunt, J. He, gave me spiritual support every time I feel uncomfortable. Without their support, I cannot achieve what I achieve today. Thank you!

Finally, I also want to state that all of the materials presented in this thesis have been published and proper references have been cited, and some published figures and possibly text have been used for this thesis.

TABLE OF CONTENTS

LIST OF TABLES

LIST OF FIGURES

SUMMARY

Energy science is becoming an increasingly important multi-disciplinary area, for not only addressing the worldwide energy crisis, but also realizing desired power sources with advanced features for portable electronic devices and sensor networks. As for energy generation from environment, mechanical energy is one of the most important forms, which has a wide range of existence and can potentially be the energy supply for the independent and portable operation of electronic devices at anywhere. Very recently, based on triboelectric effect and electrostatic induction, a fundamentally new technology, triboelectric nanogenerator (TENG), has been demonstrated which shows unique merits including large output power, high efficiency, cost effective materials, and simple fabrication. But so far, the main limitation for continuing optimizing their output performance is a lack of fundamental understanding of their core working mechanism. Although some experimental work has been demonstrated, there is neither any theoretical research nor any existing theoretical method to deal with systems like TENGs that includes the complex coupling of both electrostatic and circuit simulation. Thus, the aim of this research has three folds: (1) to develop a fundamentally new simulation method to solve this kind of systems; (2) to unveil the fundamental working mechanism of TENGs by utilizing this new method, so the unique TENG output characteristics can be theoretically explained and optimization strategy for the whole TENG systems can be proposed; (3) to develop the first rational designed TENG-based self-powered system to produce mW-level DC electricity from widely-accessible human biomechanical energy, which can put this technology into practical applications.

In this thesis research, we first unveil the inherent capacitor behavior of TENG from basic electrodynamics. Then we derive the first governing equation for triboelectric nanogenerators, which are their *V-Q-x* relationship. With the *V-Q-x* relationship, we propose the first lump-parameter triboelectric nanogenerator equivalent circuit model and build the first generalized simulation tool for triboelectric nanogenerators. With this powerful simulation tool, we study the intrinsic output characteristics and load characteristics for different fundamental modes. From this analysis, the TENG optimization technique and the first TENG standard and figure-of-merit for quantifying the TENG performance are first-time brought out.

Besides the theoretical research, we also apply the developed theory to TENG-based self-powered system design. We have developed the first genuine self-powered system to meet mW requirement of personal electronics. The system includes a multilayered TENG, a power management circuit with 60% total efficiency, and a low leakage energy storage device. Our power management circuit provides the total efficiency that is about two magnitudes higher than the traditional direct charging. And the total system performance is 330 times higher than the state-of-art designs. Driven by palm tapping, this power unit can provide a continuous DC electricity of 1.044 mW on average power in a regulated and managed manner that can be universally applied as a standard power source for continuously driving numerous conventional electronics, such as a thermometer, a heart rate monitor (electrocardiograph/ECG system), a pedometer, a wearable electronic watch, a scientific calculator, and a wireless radio-frequency communication system. Our study demonstrates the first power unit that utilizes widely accessible biomechanical energy source to sustainably drive a broad range of commercial

mobile and wearable electronic devices. This self-charging unit is a paradigm shift towards infinite-lifetime energy sources that can never be achieved solely by batteries.

CHAPTER 1

INTRODUCTION

1.1 Mechanical Energy Harvesting

Energy harvesting from natural environment has long been considered as a promising supplement to traditional fuel sources.[1] On the large scale, people have involved large amount of resources in finding alternative energy sources for tradition fuels. The new energy harvesting techniques, such as mechanical energy harvesting and photovoltaics can contribute to the hugely increased electricity demand of modern society.[2,3] Besides, these energy harvesting techniques can also solve the energy source problem for mobile electronics when the traditional energy source is unreachable. For example, since to change or recharge batteries for huge numbers of mobile sensor networks is nearly an impossible task, scavenging energy from the ambient environment may be the only option to extend their lifetime. Among all of the energy sources, mechanical energy has attracted much attention, mainly for its wide availability and high operability. In contrast to solar energy, the mechanical energy, such as air flow, vibration, ocean wave, and human motion, is almost available nearly anytime and anywhere and independent of time and weather. Many technologies can be utilized to harvest mechanical energy. During the decades of efforts, these technologies mainly utilize three major effects, including electromagnetic effect,[4] the electrostatic effect,[5,6] and the piezoelectric effect.[3,7] Below we will give a brief introduction for these mechanical energy harvesting techniques.

1.1.1 Electromagnetic generator

Electromagnetic induction is the basis of most current generators. When the magnetic flux of a closed coil changes due to the external mechanical motion, an induction current will be generated in the coil. This principle is widely used in almost all power plants and can also be utilized in energy scavenge from ambient environment.

One typical example of electromagnetic generator is the generator developed by the research team headed by Dr. Beeby.[4] Figure 1-1 shows the typical structure of their generator.[4] Four high energy density sintered magnets were manually bonded with Cyanoacrylate to the top and bottom surfaces of a cantilever beam with the aid of an alignment jig. The magnets were $1 \times 1 \times 1.5$ mm^3 in size, being 1.5 mm in the poled direction. The magnetic circuit is completed by zinc coated mild steel keepers which couple the flux between top and bottom magnets to produce an enhanced flux gradient through the stationary coil when the magnets start to vibrate. Some external mass is added to the generator attached to the end of the cantilever beam.

When their device is working, the generator produces a peak power of 46 μW from 60 mg acceleration across a 4000 Ω load. The power density is approximately 307 μWm^{-3} and the energy conversion efficiency is about 30%.

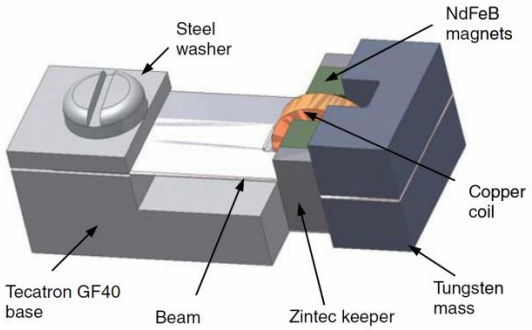

Figure 1-1. Device structure of a typical micro-electromagnetic generator. Reproduced from reference [4]. Copyright 2007 IOP publishing.

One main drawback of these electromagnetic generators is their necessary heavy permanent magnets, which are not favorable for mobile applications that require low weight generators. Besides, if these kinds of generators are utilized to harvest ocean wave energy, the density of these permanent magnets will make them sink into the ocean, where the kinetic energy density is very limited.

1.1.2 Electret generators

Electret generators are based on electrostatic induction. They utilize a kind of polymer called electrets, which are polymers that can nearly permanently conserve electrostatic charges on their surface.[6] Before putting the device to work, a precharge process is done to charge the electret surface with electrostatic charges. When this electret surface move in the space, the electrostatic effect will drive electrons to flow between the two electrodes under short-circuit conditions.

A typical example of electret generators is developed by research team headed by Prof. Yu-Chong Tai.[5] Figure 1-2 shows the working principle of their device and Figure 1-3 shows a fabricated device by their group.[5]

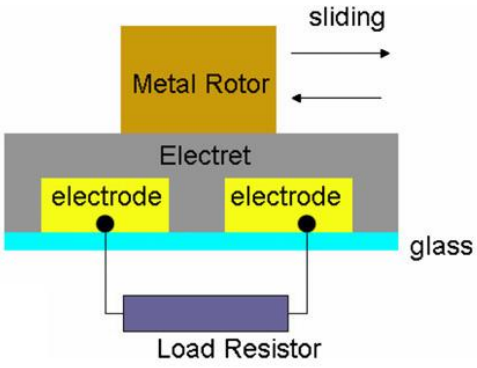

Figure 1-2**.** Schematics of designs of micro electret power generators demonstrated by Prof. Tai et al. Reproduced from reference [5]. Copyright 2008 IOP publishing.

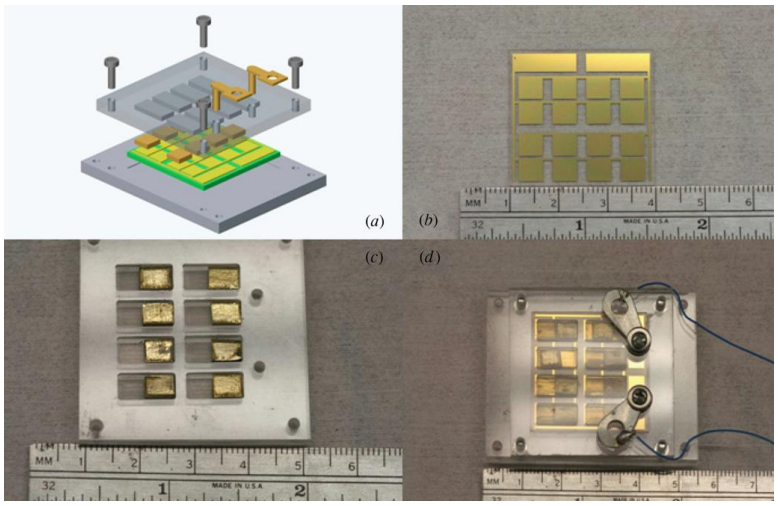

Figure 1-3. An electret generator with metal rotors demonstrated by Prof. Tai et al. (a) Schematic of the generator assembly, (b) a parylene HT-coated stator, (c) the metal rotors and (d) the final assembly. Reproduced from reference [5]. Copyright 2008 IOP publishing.

About 200 nm Au and 10 nm Cr were thermally evaporated and patterned as their output electrodes. The size of electrodes is 5mm×5mm with 2 mm spacing. Next, the glass wafer was diced into 30 mm × 30 mm stators. Then 7.32 μm parylene HT is deposited on the stator via the room temperature CVD process. Corona charging (pre-charging) is done through implanting electrons on parylene. The rotors are machined to be 4.5 mm × 4.5 mm ×2mm ($L \times W \times H$) brass blocks. The container is also machined out of acrylic material.

When an ET-132-2 electrodynamic shaker is utilized to drive the device, their maximum power output was 17.98 μW at 50 Hz with an optimum external load of 80 MΩ, showing good electrical output and energy conversion efficiency. However, for this kind of generator, the main drawback is the necessity of the pre-charging process, which is always undesirable in practical applications. Besides, the electrical output of their electrostatic generator remains low.

1.1.3 Piezoelectric Generator

Piezoelectric effect is also widely utilized in mechanical energy harvesting area. Materials, such as PVDF and PZT, are widely utilized in piezoelectric generators. A typical example of piezoelectric generators is shown in Figure 1-4, which is fabricated by the research team headed by Roundy. [8]

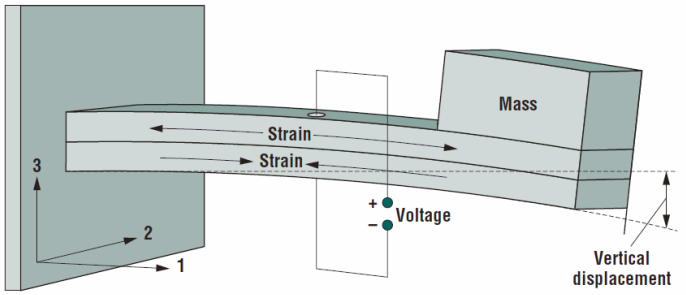

Figure 1-4**.** Structure of piezoelectric generators demonstrated by Roundy *et al*. A two-layer bimorph mounted as a cantilever. The top and bottom layers are piezoelectric; bending the beam creates tension in the top layer and compresses the bottom layer. Reproduced from reference [8]. Copyright 2005 IEEE.

The piezoelectric generator developed by Roundy *et al* is based on a two-layer bender (or bimorph) mounted as a cantilever beam.[8] The top and bottom layers of the device are composed of piezoelectric material. If the beam was bent down, a tension strain will be produced in the top layer and a compression strain will be produced in the bottom layer. Therefore, a piezoelectric voltage develops across each of the layers. When the device was driven by a vibration of 2.5 m/s^2 and 120 Hz frequency, the piezoelectric generator can produce an average power of 0.1 mW.

For the piezoelectric generators, the main drawback is still their low output. Besides, the most commonly utilized piezoelectric material PZT contains lead, which is toxic and may generate environment issues.

1.2 Triboelectric nanogenerators

From our above literature review of the long-existing mechanical energy techniques, we can easily observe each of them have their main drawbacks. In 2012, a newly invented technology, called triboelectric nanogenerators (TENGs), overcome the above drawbacks and exhibit unique figure of merits, including large output power, high efficiency, low weight and cost effective materials, simple fabrication, and high adaptability to different applications.[9] The main working principle of triboelectric generators is a conjugation between the contact electrification and electrostatic induction. When two dielectrics (or one dielectric and one metal) contact with each other, polarized triboelectric charge will be generated due to the contact electrification effect.[10-12] Then when the polarized triboelectric charges are separated by the external mechanical motion, external work will be done to overcome the attraction force between the polarized triboelectric charges. Through this process, the mechanical energy is converted into electricity.

Several experimental works of TENGs have been done for different applications. There are several fundamental operation modes available, which are attached-electrode contact-mode triboelectric nanogenerators,[13,14] attached-electrode sliding-mode triboelectric nanogenerators,[15-17] single-electrode triboelectric nanogenerators,[18,19] and freestanding triboelectric-layer-based nanogenerators.[20-23] Below we will use a few pages to talk about the experimental design of triboelectric nanogenerators for different applications.

1.2.1 Attached-electrode contact-mode triboelectric nanogenerators

A typical structure and experimental design of attached-electrode contact-mode triboelectric nanogenerators is the arch-shaped triboelectric nanogenerators finished by my college Sihong Wang and Long Lin.[14] The basic structure design of the arc-shaped TENG is shown in the figure below. A silicon oxide layer is deposited in the backside of the Kapton layer utilizing a high temperature PECVD technique. Due to the difference between the thermal expansion coefficient between the oxide and Kapton, at the room temperature, the Kapton will be curved, forming an arc-shape structure. Then back metal electrode was deposited utilizing ebeam-evaporation and a PDMS layer with specific nano-pattern is attached to the other side of the Kapton tape. Finally, an Al foil is bonded to the curved structure utilizing the tapes and the device is fabricated.[14]

Through external driving force from a mechanical motor, the maximum open-circuit voltage can reach about 200 V and the maximum short-circuit current can reach about 0.1 mA. The maximum transit power delivered to a resistive load can reach about 8 mW. The device can be utilized to directly drive tens of LEDs and charge a mobile phone battery. [14]

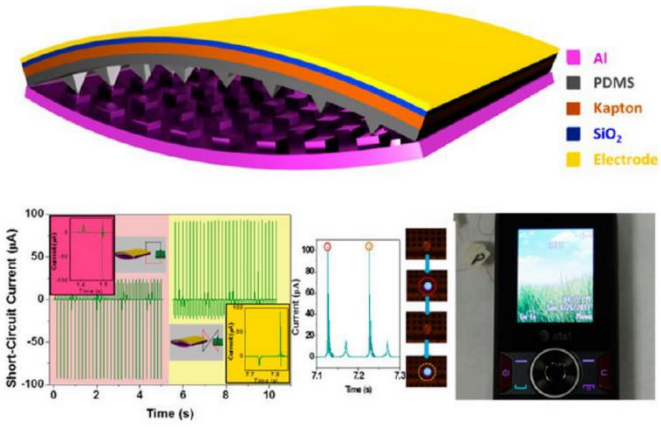

Figure 1-5. Schematic design and performance of arc-shaped triboelectric nanogenerators demonstrated by Wang *et al.* Reproduced from reference [14]. Copyright 2012 American Chemical Society.

1.2.2 Sliding-mode attached-electrode triboelectric nanogenerators

Besides the contact-mode attached-electrode triboelectric nanogenerators that are based on vertical charge separation, another important category of attached-electrode triboelectric generators is sliding-mode attached-electrode triboelectric nanogenerators. A typical attached-electrode sliding-mode triboelectric nanogenerator is shown in the following figure.[16] Two dielectrics Nylon and PTFE are shown as two tribo-pair materials. Two metal electrodes were sputtered to one side of the polymer. Two glass slides were employed to support the whole structure. The bottom plate is fixed on the measurement platform and the top plate is driven by a linear motor.

When a linear motor is moving under first uniform acceleration and then uniform deceleration, the open-circuit voltage of the TENG is measured to be around 1300 V and short-circuit transferred charge density is measured to be around 100 μCm^{-2}. On the matched resistance, the maximum transit power delivered to a resistive load is about 1.42 mW. Several LEDs can be directly driven by this generator.[16]

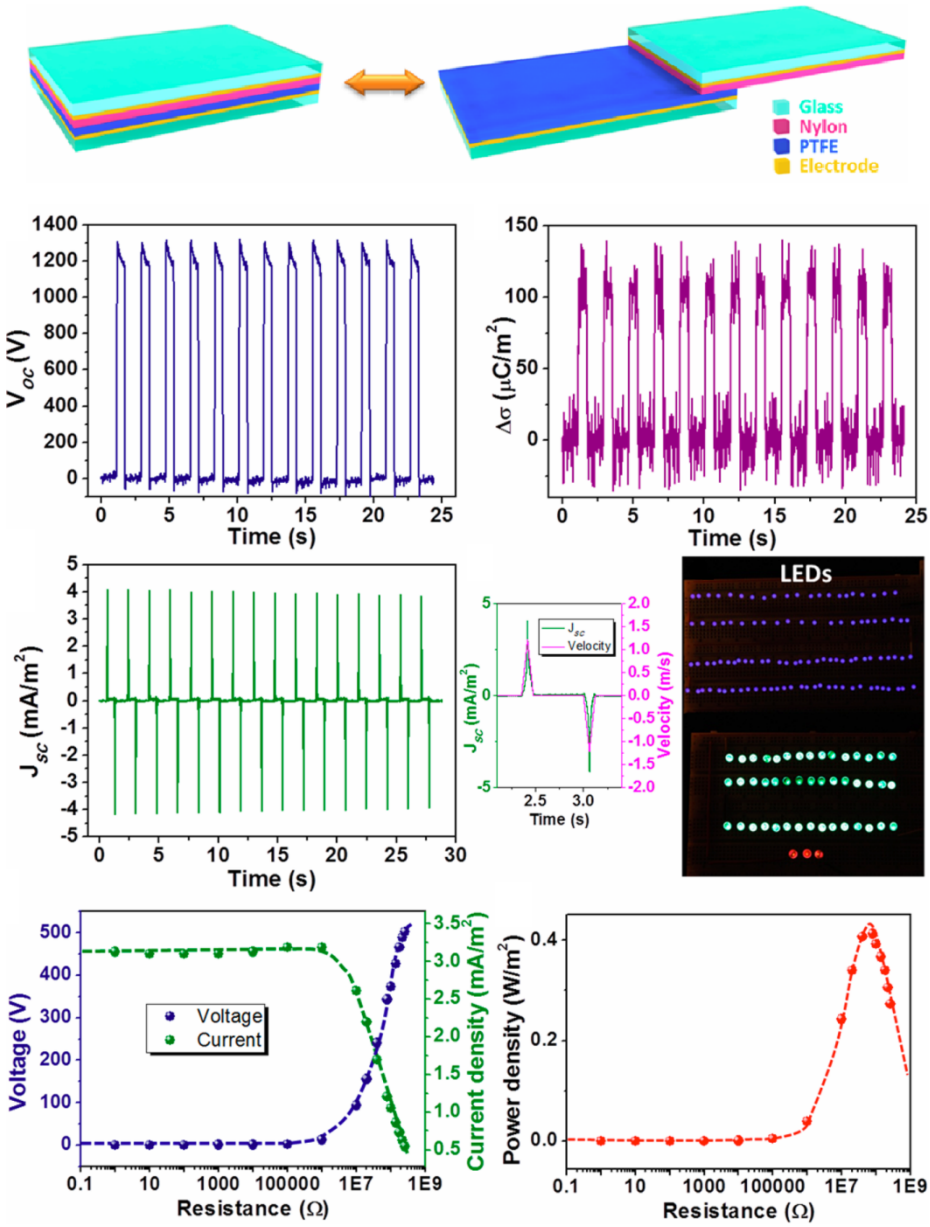

Figure 1-6. Schematic design and performance of attached-electrode sliding-mode triboelectric nanogenerators demonstrated by Wang *et al*. Reproduced from reference [16]. Copyright 2013 American Chemical Society.

Utilized similar mechanism, several other structure of sliding-mode attached-electrode TENG can be designed. Among them, attached-electrode disk TENGs[17] and attached-electrode grating TENGs[15] are two important categories. Attached-electrode disk TENGs can be utilized to harvest rotation energy. In addition, grating design can

significantly increase the output current and lower the matched load resistance, which can be utilized to increase the maximum output power.

1.2.3 Single-electrode triboelectric nanogenerators

In the above two attached electrode TENGs, the moving object both need to be bonded with an electrode and a lead wire. Such kind of design strongly limits the application of TENGs because the moving object of many practical applications does not belong to the device system. To overcome these problems, single-electrode TENGs[18,19] and freestanding-triboelectric-layer based nanogenerators[20-23] are designed with fixed electrodes.

A typical example of single-electrode TENGs is shown in the following figure.[19] A PET substrate of 50 μm thickness was utilized as the substrate. Then both side of the PET was deposited with 150 nm of ITO as electrodes. Finally, a nylon thin film (50 μm) was adhered on one side of the device as a protection layer and a FEP thin film (50 μm) was adhered on the other side of the device as an electrification layer. In this device, one electrode is more close to contact electrification surface (called primary electrode) and the other electrode just serves as an electrical potential reference (called reference electrode). The reference electrode can be placed anywhere downside and can even be directly the ground. This device can be directly utilized as flexible tactile sensors. When the human finger touches the surface of the FEP, an electrical potential difference will be generated between these two electrodes. At low pressure range, the touch sensitivity can reach about 1V/Pa.[19]

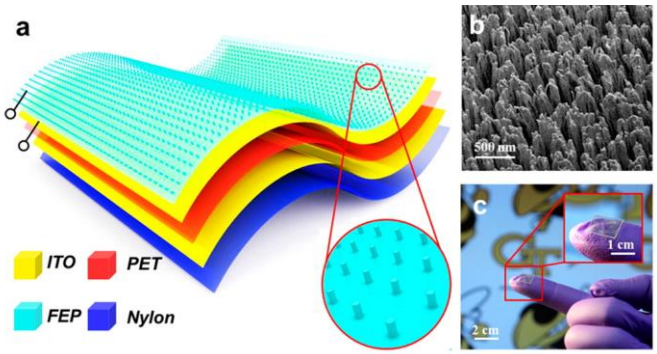

Figure 1-7. Schematic design of single-electrode triboelectric nanogenerators as a tactile sensor by Zhu *et al*. Reproduced from reference [19]. Copyright 2014 American Chemical Society.

1.2.4 Freestanding-triboelectric-layer based nanogenerators

Besides the single electrode TENGs, another important category of fixed electrode TENGs is the freestanding-triboelectric-layer based nanogenerators (FTENGs).[20-23] One typical structure of FTENGs is shown in the following figure. In FTENGs, the triboelectric layer will alternatively approach both the two electrodes while the triboelectric layer only approaches one electrode in single-electrode TENGs. Such kind of FTENG is very easy to fabricate.[22] Two pieces of acrylic sheets were tailored as the supporting substrates. Then a piece of FEP layer was attached to one acrylic sheet as the freestanding layer. The metal pattern was deposited on the second acrylic layer to form the two electrodes and the gap. Driven by a linear motor, this structure can provide a 16KV open-circuit voltage and 3 mAm^{-2} short-circuit current density. Under matched load condition, the optimum power density can reach about 6 Wm^{-2}. Some unique applications have also been demonstrated by this structure. This structure can be utilized to harvest energy from a walking human or a moving automobile.[22]

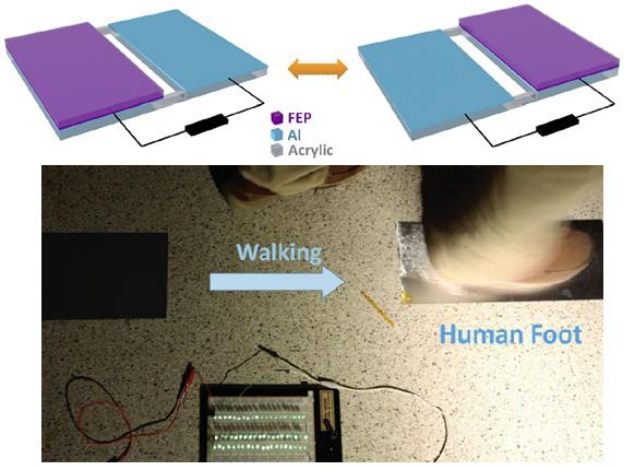

Figure 1-8. Schematic design of freestanding triboelectric nanogenerators by Wang *et al* and its application in harvesting mechanical energy from human walking. Reproduced from reference [22]. Copyright 2014 Wiley.

1.3 Objective of the current research

Although several experiments have already been demonstrated by some of our group members, there are still a lot of mysteries of fundamental understanding of triboelectric nanogenerators. First, the core working mechanism of triboelectric nanogenerators is still unclear. Second, as a basic electronic device, the governing equation of triboelectric nanogenerators needs to be unveiled and understood. Third, in the previous experiments, the resistive load effect of triboelectric nanogenerators is observed to be a "three-working-region" behavior and an optimum resistance to maximize the transit/average power is also observed. However, the fundamental understanding of the formation of this "three-working-region" behavior[23] is unclear and the dependence of the optimum resistance on the structural and motion parameters is unclear as well, which prohibits the rational design of TENGs for practical applications. Fourth, currently no simulation method exists for triboelectric nanogenerators and no models exist for these newly-invented devices. Fifth, due to the lack of basic theoretical

understanding, how to structurally optimize TENGs to reach the highest performance is still unknown. Finally and also the most importantly, experiments have observed that TENGs can only provide alternating currents, which means that TENGs cannot be directly utilized to drive commercial electronics that requires constant voltage power sources. Therefore, an energy storage unit is necessary to serve as a "reservoir" for collecting the generated charges and outputting them in a managed and regulated manner. However, a direct integration of a TENG with an energy storage device has shown extremely low charging efficiency and large power loss. Thus, although there are several TENG-based "self-powered" systems being reported, all of these systems either cannot work continuously due to the low level of generated DC power or the entire system cannot be exclusively driven by the harvested energy if the data measurement and processing systems as well as data transmission components are included.

The main objective of this research is to demonstrate the first genuine self-powered system that can provide mW-level DC power from ambient environment energy sources. However, to realize this goal, a thorough theoretical understanding of the fundamental physics of TENGs is completely necessary. My research first focuses on the fundamental physics and working principle of triboelectric nanogenerators. In my research, the governing equation and equivalent circuit model of a TENG is first-time brought out. With the equivalent circuit model, a systematical simulation method (TENG-simulator) is proposed to simulate output performance of TENGs, which combines complex coupling between electrostatic simulation and circuit simulation. Then, the intrinsic output characteristics (open-circuit voltage, short-circuit transferred charges, and inherent capacitance) of all fundamental TENG modes are discussed in detail and the

resistive load and capacitive load characteristics are shown, which finishes the discussion of TENG theoretical part. Finally, utilizing the above theoretical analysis knowledge, we have finally realized the first integrated TENG-based energy harvesting system. The system includes a TENG, a power management circuit, and a low leakage energy storage device. We perform system-level optimization to ensure the collaborative work of all the system components. Especially a power management circuit is designed to solve the impedance mismatch problem, which can achieve 90% board efficiency and 60% total efficiency, about two orders of magnitude improvement compared to direct charging. Driven by palm tapping, this power unit can provide a continuous DC electricity of 1.044 mW on average power in a regulated and managed manner that can be universally applied as a standard power source for continuously driving numerous conventional electronics, such as a thermometer, a heart rate monitor (electrocardiograph/ECG system), a pedometer, a wearable electronic watch, a scientific calculator, and a wireless radio-frequency communication system.

CHAPTER 2

FUNDEMENTALS OF TRIBOELECTRIC NANOGENERATORS

2.1 Inherent capacitive behavior and governing equations

The fundamental working principle of TENGs is a conjugation of contact electrification and electrostatic induction. Contact electrification provides static polarized charges and electrostatic induction is the main mechanism that converts mechanical energy to electricity. Since the most fundamental device based on electrostatics is a capacitor, fundamentally TENG will have inherent capacitive behavior.[24]

An arbitrary TENG is analyzed to unveil its inherent capacitive behavior. For any triboelectric generators, there are pair of materials which are face to each other (called tribo-pairs). The distance (x) between these two triboelectric layers can be varied under the agitation of mechanical force. After being forced to get into contact with each other, the contact surface of the two triboelectric layers will have opposite static charges (tribo-charges), as a result of contact electrification. Besides the tribo-pair layers, there are two electrodes that are carefully insulated inside the TENG system, which ensures the charges can only transfer between the two electrodes through external circuits. If we define the transferred charges from one electrode to another is Q, one electrode will have the transferred charge $-Q$ and the other electrode will have the transferred charge $+Q$.

The electrical potential difference between the two electrodes of any TENGs mainly contributes to two parts. The first part is from the polarized triboelectric charges and their contribution to the voltage is $V_{OC}(x)$, which is a function of separation distance

x. Besides, the already transferred charges Q will also contribute to an electric potential difference. If we assume no triboelectric charges exist in this structure, this structure is completely a typical capacitor, so the contribution of these already transferred charges is -$Q/C(x)$, where C is the capacitance between the two electrodes. Therefore, due to the electrical potential superposition principle, the total voltage difference between the two electrodes can be given by:[24]

$$V = -\frac{1}{C(x)}Q + V_{\mathrm{OC}}(x) \qquad (2.1)$$

Equation 2.1 (named as *V*-*Q*-*x* relationship) is the governing equation of any TENGs, clearly explaining its inherent capacitive behavior.[24] The separation of the polarized tribo-charges will generate an electrical potential difference between the two electrodes. If the external circuit exists between the two electrodes, this electrical potential will drive electrons to flow from one electrode to another. These already-transferred electrons can further screen the electrical potential between the two electrodes.[25] Under short-circuit (SC) conditions, these transferred charges (Q_{SC}) fully screen the electrical potential generated from polarized triboelectric charges. Therefore, the following equation can be easily derived for TENGs under short-circuit conditions.[26]

$$0 = -\frac{1}{C(x)}Q_{\mathrm{SC}}(x) + V_{\mathrm{OC}}(x) \qquad (2.2)$$

Thus, the fundamental relationship among Q_{sc}, C, and V_{oc} can be given by:[26]

$$Q_{\mathrm{SC}}(x) = C(x)V_{\mathrm{OC}}(x) \qquad (2.3)$$

2.2 First-order lumped-parameter equivalent circuit model

From the governing equation (*V*-*Q*-*x* relationship) of triboelectric nanogenerators, we can easily derive their lumped parameter equivalent circuit model.[27] From Equation 2.1 shown above, there are two terms at the right side, which can be represented by two circuit elements in the equivalent circuit model. The first one is a capacitance term, which is originated from the inherent capacitance between the two electrodes and can be represented by a capacitor (*C*). The other is an open-circuit voltage term, which is originated from the separation of the polarized tribo-charges and can be represented by an ideal voltage source (V_{OC}). In combination of these two, the whole lumped parameter equivalent circuit model can be represented by a serial connection of an ideal voltage source and a capacitor, as shown in Figure 2-1.[27]

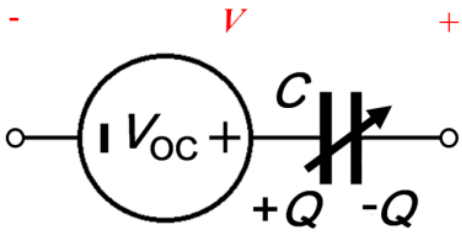

Figure 2-1. First-order lumped-parameter equivalent circuit model of any triboelectric nanogenerators. Reproduced from reference [27]. Copyright 2014 Elsevier.

Besides, it's valuable to note that the inherent impedance of TENG mainly comes from its inherent capacitance. For a rationally designed TENG, the internal resistance is close to infinity mainly for the excellent insulation between the two electrodes. So in the first-order equivalent circuit model, this resistance was not included.

Finally, we want to briefly discuss the difference between TENGs and traditional electromagnetic induction generators. First, their fundamental operating principles are different: TENGs rely on the conjugation effect of contact electrification and electrostatic

induction while electromagnetic induction generators rely on the electromagnetic induction. Second, TENGs are inherently capacitive and the internal resistance for rational designed TENGs is close to infinity. Their internal high impedance is mainly from their small inherent capacitance. However, electromagnetic induction generators are inherently resistive and their internal resistance is much lower than the impedance of TENGs. Third, the equivalent circuit model for TENGs is a serial connection of an ideal voltage source with a capacitor while that for electromagnetic induction generators is a serial connection of an ideal voltage source with a resistor. In summary, TENGs are high-impedance charge sources and electromagnetic generators are low-resistance voltage sources.

From the equivalent circuit model, we can summarize the fundamental simulation method for TENGs. The simulation of TENG-based energy harvesting systems mainly contains two parts, including electrostatic simulation and load circuit simulation, as summarized in Figure 2-2. [27]

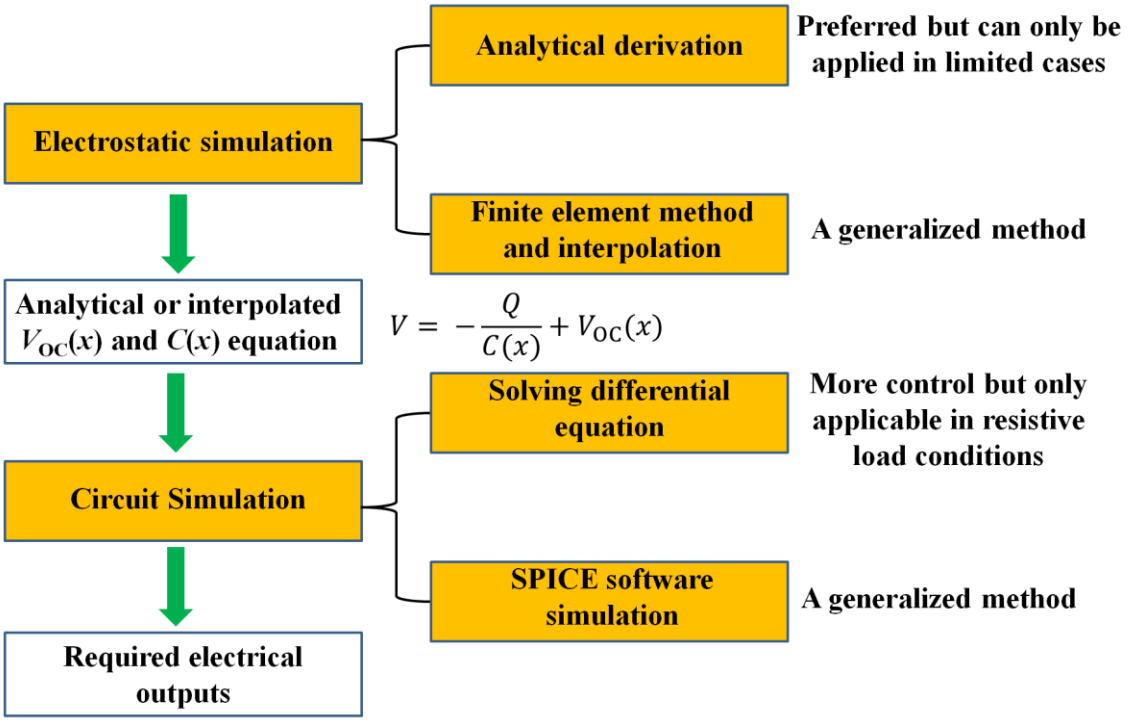

Figure 2-2. Flow chart of typical TENG simulation process.

The main objective of the electrostatic simulation is to obtain the $V_{oc}(x)$ and $C(x)$ functions in the V-Q-x relationship. Two methods are currently developed to specify the $V_{OC}(x)$ and $C(x)$ relationships. Analytical derivation is a preferred method but it only works for certain geometry features such as parallel-plate attached-electrode contact-mode and sliding-mode TENGs with appropriate approximations. A more general method which works for all TENGs is numerical calculation based on finite element method (FEM). The finite element calculation can be easily performed utilizing common FEM simulation software such as COMSOL and ANSYS. In this numerical method, the value of V_{OC} and C is first obtained at certain values of x. Then, from continuous fraction interpolation,[28] a numerical $V_{OC}(x)$ and $C(x)$ relationship can be generated in the entire x region.

Once the numerical $V_{OC}(x)$ and $C(x)$ relationship is obtained, the output characteristics can be numerically calculated through load circuit simulation. When the load is very simple, the governing differential equation of whole system can be easily derived through Kirchhoff's law. For example, when the load is purely resistive, the governing differential equation containing the TENG and the resistor can be given by:[27]

$$R\frac{\mathrm{d}Q}{\mathrm{d}t} = V = -\frac{1}{C}Q + V_{\mathrm{OC}} \quad (2.4)$$

Such a differential equation can be solved by numerical integration and for some specific TENG systems and motion conditions, even analytical results can also be obtained. However, this kind of differential equation can only be obtained for limited cases with very simple load circuits. When the load circuit is complicated, solving the differential equation set is nearly an impossible task.

A general method that works for all TENG systems is to utilize SPICE software.[27] From the above TENG equivalent circuit model, the TENG can be embedded into the SPICE software as a basic element consisting of a voltage source in serial connection with a capacitor. Then any other circuit elements, including resistors, capacitors, inductors, diodes, and transistors can be put into the software to form the entire TENG system. After specifying the motion process and the initial condition, the powerful SPICE software can be easily utilized to simulate the real-time output of any TENG systems.

2.3 Charge Reference State

The reason to define a charge reference state for TENG is simple. For any TENGs under short-circuit conditions, the charge distribution on the two electrodes is unique. However, the cases are completely different under open-circuit conditions. We only

know the total charges amount on the two electrodes as a combination and the charge amount on each electrode is a constant because of no charge transfer between the two electrodes. However, the detailed charge distribution on one electrode can be arbitrary and therefore the voltage between the two electrodes is arbitrary. Therefore, to facilitate theoretical calculation, we need to assign a charge reference state that one electrode has specific amount of charge (Q_0) and under this condition, we can calculate the basic characteristics of TENGs.[29]

2.3.1 Influence of charge reference state on the triboelectric nanogenerator intrinsic characteristics

For any TENGs, their intrinsic characteristics are their V_{OC}-x, Q_{SC}-x and C-x curves. Of course, the C-x curve is completely independent of the charge reference state. In fact, the charge reference state pick-up will not affect the magnitude and the shape of the Q_{SC}-x curve, but only translates them upside or downside. But the chosen of the charge reference state will strongly affect both the magnitude and the shape of the V_{OC}-x curve if the inherent TENG capacitance is not a constant and varies with x.

For example, we can analyze the metal SFTENG electrostatic system that will be discussed in detail in Chapter 3.4 (Figure 2-3a).[29] In the system under open-circuit (OC) condition, we only know that the total charge amount on metal 1 and metal 2 as a combination is σwl and the total charge amount on metal 3 is 0. Under short-circuit (SC) condition, the charge distribution on the two electrodes is unique, so the charge amount on metal 1 and metal 2 under short circuit conditions (Q_1 and Q_2, respectively) is a specific number if the position of the freestanding layer is given.

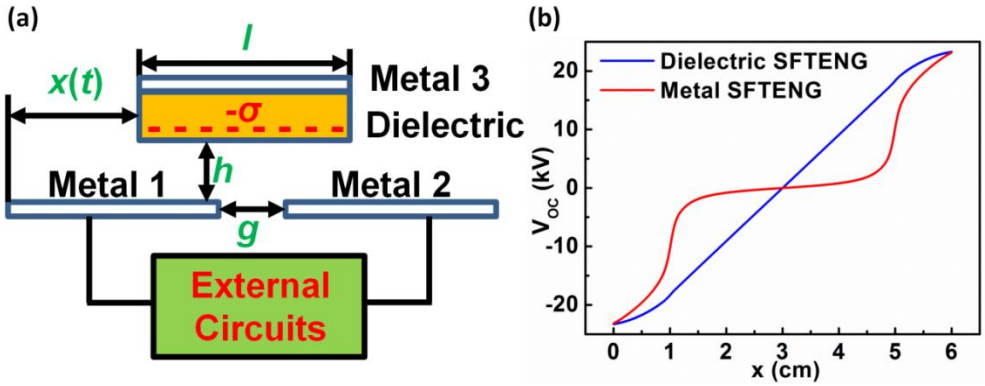

Figure 2-3. Influence of charge reference state on open-circuit voltage profile. (a) Structure of a dielectric freestanding-layer sliding-mode TENG. (b) Open-circuit profile of Dielectric freestanding sliding-mode TENG and metal freestanding sliding-mode TENG under symmetric reference state. Reproduced from reference [29]. Copyright 2014 Elsevier.

But the voltage between metal 1 and 2 relies on the charge reference state. If we assign a charge reference state A that the amount of charge on metal 2 is Q_{0A} (at the same time, the amount of charge on metal 1 is σwl-Q_{0A}), we can calculate the open-circuit voltage between metal 1 and 2 (V_{OCA}) through FEM calculation. Besides, the short-circuit transferred charges under charge reference state A (Q_{SCA}) can also be calculated as Q_2-Q_{0A}.

If we choose a new reference state B that the amount of charge on metal 2 is Q_{0B}, we can analyze its influence on the calculated V_{OC} and Q_{SC}. Under this condition, the voltage is contributed from two parts of the charges. One part is the same as the case of charge reference state A and the voltage generated by these charge is also V_{OCA}. The other part is the extra Q_{0A}- Q_{0B} charges on metal 1 and the extra Q_{0B}- Q_{0A} charges on metal 2 and the voltage generated by these charges is -(Q_{0B}- Q_{0A})/C, where C is the total capacitance between metal 1 and metal 2. Therefore, because of the electric potential

superposition principle, the open-circuit voltage between metal 1 and 2 (V_{OCB}) under charge reference state B can now be given by:

$$V_{OCB} = V_{OCA} - \frac{Q_{0B} - Q_{0A}}{C} \quad (2.5)$$

Besides, the short-circuit transferred charges under charge reference state B (Q_{SCB}) can be given by:

$$Q_{SCB} = Q_2 - Q_{0B} = Q_2 - Q_{0A} - (Q_{0B} - Q_{0A}) = Q_{SCA} - (Q_{0B} - Q_{0A}) \quad (2.6)$$

Therefore, from the above two equations, we can fully understand the influence of charge reference state on the Q_{SC}-x and V_{OC}-x curve. From equation 2.6, we know that the Q_{SC}-x curve under charge reference state B is just a vertical translation of the curve under charge reference state A. However, the V_{OC}-x curve change is much more complicated because that the capacitance may also be a function of x. Therefore, both the magnitude and the shape of the V_{OC}-x curve may change if a different charge reference state is picked up. But if the capacitance is a constant, the V_{OC}-x curve under charge reference state B will also be a vertical translation of the curve under charge reference state A.

2.3.2 Influence of charge reference state on the triboelectric nanogenerator output characteristics

The chosen of the charge reference state will not affect the calculated voltage and current output when a resistance load is connected with the TENG as long as right boundary condition for solving the differential equation is picked up as well.

For example, we can still analyze the above case. To calculate the output characteristics, we need to specify the motion condition which is $x = x(t)$ and the boundary condition which is the amount of charges on metal 1 when $t = 0$ ($Q_{initial}$).

If we choose the charge reference state A, the differential equation is:

$$R\frac{\mathrm{d}Q_A}{\mathrm{d}t} = -\frac{1}{C}Q_A + V_{\mathrm{OCA}} \quad (2.7)$$

And the corresponding boundary condition that the amount of charges on metal 2 when $t = 0$ is Q_{initial} is mathematically shown as the following equation under charge reference state A.

$$Q_A(t=0) = Q_{\mathrm{initial}} - Q_{0A} \quad (2.8)$$

Under charge reference state B, the differential equation and corresponding boundary condition can be given by:

$$R\frac{\mathrm{d}Q_B}{\mathrm{d}t} = -\frac{1}{C}Q_B + V_{\mathrm{OCB}} \quad (2.9)$$

$$Q_B(t=0) = Q_{\mathrm{initial}} - Q_{0B} = Q_A(t=0) - (Q_{0B} - Q_{0A}) \quad (2.10)$$

And utilizing equation 2.5, equation 2.9 can be simplified to:

$$R\frac{\mathrm{d}(Q_B + (Q_{0B} - Q_{0A}))}{\mathrm{d}t} = R\frac{\mathrm{d}Q_B}{\mathrm{d}t} = -\frac{1}{C}Q_B + V_{\mathrm{OCA}} - \frac{Q_{0B} - Q_{0A}}{C} \quad (2.11)$$

Thus,

$$R\frac{\mathrm{d}(Q_B + (Q_{0B} - Q_{0A}))}{\mathrm{d}t} = -\frac{1}{C}\left(Q_B + (Q_{0B} - Q_{0A})\right) + V_{\mathrm{OCA}} \quad (2.12)$$

Compare equation 2.12 and 2.7 with equation 2.10 and 2.8, we can easily obtain that:

$$Q_B = Q_A - Q_{0B} + Q_{0A} \quad (2.13)$$

Since the current and voltage output on the resistor is the differential of Q_{A} and Q_{B} by t, the calculated current and voltage output will be independent of the choice of charge reference state. Similarly, if the periodic boundary condition is utilized to solve

the equation, the calculated current and voltage output will also be independent of the choice of charge reference state.

2.3.3 Typical charge reference states

The most commonly utilized charge reference state is called minimum achievable charge reference state (MACRS), which utilizes the amount of charge on metal 2 under SC condition when $x = 0$ as Q_0 (which is also the minimum achievable amount of charges on metal 2 under SC conditons).[29] The main advantage to utilize the minimum achievable charge reference state is to set both $Q_{SC}(x=0)$ and $V_{OC}(x=0)$ to 0 and this time Q_{SC} stands for the total transferred charges amount from one electrode to another under short-circuit conditions.

FEM results from other charge reference states can be easily converted to the MACRS. From the above derivation, we can easily get the below conversion equation.

$$V_{\mathrm{OC,MACRS}}(x) = V_{\mathrm{OC,other}}(x) - \frac{V_{\mathrm{OC,other}}(0)C(0)}{C(x)} \qquad (2.14)$$

Although the minimum achievable charge reference state is the most commonly utilized charge reference state in TENGs, utilizing this charge reference state in freestanding TENGs will lead to a nonsymmetrical calculated V_{OC}. However, an inherent symmetry can be easily observed in the structure for both contact-mode freestanding TENGs and sliding-mode freestanding TENGs. The reason that the calculated V_{OC} are nonsymmetrical under MACRS is mainly because the amount of charges assigned on metal 1 and metal 2 are different. To maintain the symmetry, we can assign both metal 1 and metal 2 have the same amount of charges ($\sigma wl/2$). Then the calculated V_{OC} will be fully symmetric. Figure 2-3b shows the FEM calculation result of V_{OC} under symmetric

charge reference state for both dielectric SFTENG and metal SFTENG. Compare to the results under MACRS, the curve shape of the dielectric SFTENG is similar mainly because its capacitance is nearly a constant. The curve shape of the metal SFTENG changes a lot and now has odd symmetry.

CHAPTER 3

INTRINSIC TRIBOELECTRIC NANOGENERATOR OUTPUT CHARACTERISTICS AND FUNDEMENTAL MODES

In Chapter 2, we have discussed the fundamental knowledge and simulation method of triboelectric generators. In this chapter, we will move one-step further. From basic electrodynamics, we will classify the TENGs by different modes from their fundamental electrostatic induction process. And for each TENG mode, we will discuss their intrinsic output characteristics (open-circuit voltage V_{OC}, short-circuit transferred charges Q_{SC}, inherent capacitance C) in detail.

3.1 Attached-electrode contact-mode triboelectric generators

The first fundamental TENG working mode is called attached-electrode contact-mode TENG, which is based on vertical charge separation mechanism.[25] This is also the earliest experimentally demonstrated TENG mode.[9,13,14] Based on the materials for the triboelectric pairs, the attached-electrode contact-mode TENG is mainly divided into two categories: dielectric-to-dielectric and conductor-to-dielectric types. The model built for a dielectric-to-dielectric contact-mode TENG is shown in Figure 3-1a.[25] The two dielectric plates, with thicknesses of d_1 and d_2 and the relative dielectric constants ε_{r1} and ε_{r2}, respectively, are stacked face to face as two triboelectric layers. At the outer surface of these two dielectrics, two metal layers are deposited as two electrodes. The distance (x) between the two triboelectric layers can be varied under the agitation of mechanical

force. After being forced to get in contact with each other, the inner surfaces of the two triboelectric layers will have opposite static charges (tribo-charges) with equal density of σ, as a result of contact electrification. For insulators as discussed, it is reasonable to assume that the tribo-charges are uniformly distributed at the two surfaces with negligible decay.[30,31] When the two triboelectric layers start to separate from each other, with increased x, a potential difference (V) between the two electrodes will be induced. The amount of transferred charges between the two electrodes, as driven by the induced potential, is defined as Q. We choose the minimum achievable charge reference state (MACRS) discussed in last chapter, so the instantaneous amount of charges on the electrode is Q and $-Q$, respectively.

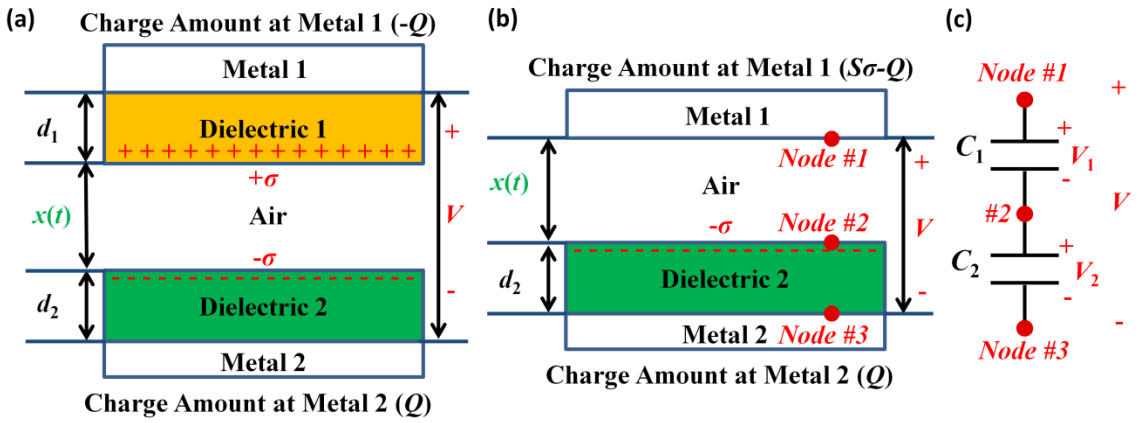

Figure 3-1. Theoretical models for (a) Dielectric-to-dielectric attached-electrode parallel-plate contact-mode TENG and (b) Conductor-to-dielectric attached-electrode parallel-plate contact-mode TENG. (c) Equivalent circuit diagram for Conductor-to-dielectric attached-electrode parallel-plate contact-mode TENG. Reproduced from reference [25]. Copyright 2013 Royal Society of Chemistry.

Similarly, the model for conductor-to-dielectric type is built, as shown in Figure 3-1b. In this structure, we no longer have the Dielectric 1 and now the metal 1 plays two roles: both as the top triboelectric layer and as the top electrode. Therefore, the total

charges in the metal 1 now have two parts: one is the triboelectric charges ($S\cdot\sigma$), the other is the transferred charges between the two electrodes ($-Q$). Thus, the total charges in the metal 1 are ($S\sigma$ - Q).

Since the area size (S) of the metals is several orders of magnitude larger than their separation distance ($d_1 + d_2 + x$) in the experimental case, it is reasonable to assume that the two electrodes can be seen as infinitely large. Under this assumption, the charges on the metal electrodes will uniformly distribute on the inner surfaces of the two metals. Inside the dielectrics and the air gap, the electric field only has the component in the direction perpendicular to the surface, with the positive value pointing to metal 2. From Gauss theorem, the electric field strength at each region is given by:

Inside Dielectric 1: $E_1 = -\frac{Q}{S\varepsilon_0\varepsilon_{r1}}$ (3.1)

Inside the air gap: $E_{\text{air}} = \frac{-\frac{Q}{S} + \sigma}{\varepsilon_0}$ (3.2)

Inside Dielectric 2: $E_2 = -\frac{Q}{S\varepsilon_0\varepsilon_{r2}}$ (3.3)

The voltage between the two electrodes can be given by:

$$V = E_1 d_1 + E_2 d_2 + E_{\text{air}} x \quad (3.4)$$

Therefore, we can get obtain the V-Q-x relationship for dielectric-to-dielectric TENGs in attached-electrode contact-mode, which is given by:

$$V = -\frac{Q}{S\varepsilon_0}\left(\frac{d_1}{\varepsilon_{r1}} + \frac{d_2}{\varepsilon_{r2}} + x(t)\right) + \frac{\sigma x(t)}{\varepsilon_0} \quad (3.5)$$

From the similar derivation, the V-Q-x relationship for the conductor-to-dielectric TENG is given by:

$$V = E_2 d_2 + E_{air} x = -\frac{Q}{S\varepsilon_0}\left(\frac{d_2}{\varepsilon_{r2}} + x(t)\right) + \frac{\sigma x(t)}{\varepsilon_0} \quad (3.6)$$

Equation 3.6 is exactly the same equation as Equation 3.5 if $d_1 = 0$. We define the effective thickness constant d_0 as the summation of all the thickness of the dielectric d_i between the two metal electrodes divided by its relative effective thickness ε_{ri}, as shown below.

$$d_0 = \sum_{i=1}^{n} \frac{d_\mathrm{i}}{\varepsilon_\mathrm{ri}} \qquad (3.7)$$

From the *V*-*Q*-*x* relationship, the intrinsic output characteristics (V_{OC}, Q_{SC}, and C) of such a contact-mode attached-electrode TENG can be shown as: [25]

$$V_{OC} = \frac{\sigma x(t)}{\varepsilon_0} \quad (3.8a) \qquad Q_{SC} = \frac{S\sigma x(t)}{d_0 + x(t)} \quad (3.8b) \quad C = \frac{\varepsilon_0 S}{d_0 + x(t)} \quad (3.8c)$$

Besides utilizing the Gauss Theorem, we can derive its *V*-*Q*-*x* relationship from the detailed electrostatic induction mechanism, through which we can show the fundamental working principle of such triboelectric generators.

We first need to define the nodes in this electrostatic system. A node in an electrostatic system corresponds to a surface/volume with the same electrical potential. Since the area size is assumed to be infinitely large and all the dielectric layers are uniform, the whole tribo-charged dielectric 2 surface is with the same electrical potential and can be thought as one node (Node 2). Since the electrical potential of the whole metal electrode is also the same, the electrode 1 and electrode 2 are other two nodes in this electrostatic system (Node 1 and Node 3, respectively), as shown in Figure 3-1b. Since every two nodes are connected by electric field lines, an equivalent capacitance is formed between each of them. However, since dielectric 2 surface is assumed to be infinitely large, the electrical line connection of Node 1 and Node 3 is fully blocked by the Node 2.

Therefore only two capacitances exist in this electrostatic system, as shown in Figure 3-1c.

Now we consider this system under short-circuit conditions, when the Node 1 and Node 3 has the same electrical potential. Under this condition, the total amount of charges on Node 1 and Node 3 is σS while that on Node 2 is $-\sigma S$. From charge conservation and Kirchhoff's Law, the amount of charges on Node 3 is easily given by:

$$Q_{\text{node3}} = \frac{\sigma S}{1 + \frac{C_1(x)}{C_2(x)}} \qquad (3.9)$$

So when x is changing from 0, the short circuit transferred charges from Node 3 to Node 1 (Q_{SC}) can be given by:

$$Q_{SC} = \frac{\sigma S}{1 + \frac{C_1(x)}{C_2(x)}} - \frac{\sigma S}{1 + \frac{C_1(x=0)}{C_2(x=0)}} \qquad (3.10)$$

Utilizing the parallel-plate capacitance mode, Equation 3.10 can be easily derived to be the same with Equation 3.8b. Through the above derivation, it is clearly observed that the core working mechanism of TENGs is that the change of the capacitance ratio C_1/C_2 due to the change of the position of tribo-charged surface will induce electron transfer between the electrodes under SC condition.

When the x is sufficiently large, the charge transfer efficiency η_{CT} (defined as the ratio between the final transferred charges and the total triboelectric charges) can be given by:

$$\eta_{CT} = \frac{Q_{SC,final}}{\sigma S} = \frac{1}{1 + \frac{C_1(x=x_{max})}{C_2(x=x_{max})}} - \frac{1}{1 + \frac{C_1(x=0)}{C_2(x=0)}} \qquad (3.11)$$

For the above attached-electrode contact-mode TENGs, when $x = 0$, C_1 ($\varepsilon_0 S/x$) is close to infinity while C_2 is a finite number $\varepsilon_0 S/d_0$, which ensures the amount of charge on Node 3 at this time is 0. When x is sufficiently large (larger than 10 d_0), C_1 ($\varepsilon_0 S/x$) is close to 0 while C_2 is still $\varepsilon_0 S/d_0$, which ensures the amount of charge on Node 3 at this time is σS. Therefore, the maximum charge transfer efficiency for an attached-electrode contact-mode TENG can be reach 100%.

From the above derivation, the intrinsic output characteristics of attached-electrode contact-mode TENGs have the following properties. Their open-circuit voltage is linearly proportional to the separation distance x while their inherent capacitance is inversely proportional to the separation distance x. For short-circuit transferred charges, it has a saturation trend. Q_{SC} quickly reaches 90% of the final saturation value σS when x only changes from 0 to $10d_0$. (Shown in Figure 3-3 with a comparison to single-electrode TENGs) Since the dielectric thickness is usually very small, the minimum separation distance must be effectively reduced to 0 to reach high charge transfer efficiency. If the minimum separation distance is comparable to $10d_0$, $C_1(x)$ ($\varepsilon_0 S/x$) will always be much smaller than $C_2(x)$ ($\varepsilon_0 S/d_0$). Under this condition, the capacitance ratio $C_1(x)/C_2(x)$ will always be close to 0 and changes little when x further increases, which will lead to no charge transfer between the electrodes. Besides, when x is already comparable to the size of the device, the device can be no longer seen as infinitely large and edge effect will dominate the performance. Under this condition, the open-circuit voltage will deviate from the linear relationship.

3.2 Attached-electrode sliding-mode triboelectric generators

The second fundamental working mode is called attached-electrode sliding-mode triboelectric generators, which is based on in-plane charge separation mechanism.[24] Several previous experimental works have also been demonstrated[15-17,32,33]. If we consider the materials to be used as the triboelectric layers, the attached-electrode sliding-mode TENG also has two types: dielectric-to-dielectric and conductor-to-dielectric. We first take the dielectric-to-dielectric category as an example. The model for this type of TENG was built with dimensions close to those of the real device, as shown in Figure 3-2a. Considering that the width w of the whole structure is much larger than the thickness, a 2D model is utilized to simplify the calculation. The geometric size of the two dielectrics is l in longitudinal direction and d_i (i = 1, 2) in thickness direction. Two metal electrodes are bonded with the two dielectrics layers. The bottom part is fixed while the top can slide through the longitudinal direction. The lateral separation distance is defined as x. When the two dielectrics are separated, the lower surface of Dielectric 1 and the upper surface of Dielectric 2 have charges with different signs at the non-overlapped regions, which are because of the triboelectric effect. Same as attached-electrode contact-mode TENGs, it is reasonable to assume that those triboelectric charges are uniformly distributed on these two surfaces, which is an excellent approximation for insulators. Also, the decay of tribo-charges with time can be neglected on these insulating polymers. The surface density of the tribo-charges is defined as σ at surface of Dielectric 1 and $-\sigma$ at surface of Dielectric 2. The overall density of tribo-charges on the overlapped surface can be regarded as 0 because the distance between the center of the positive charges and the negative charges are in atomic level. Under MACRS and OC conditions, the total charge

at each metal electrode was assigned as 0. If the transferred charges amount is defined by Q, the total charge amount on metal 1 and metal 2 is $-Q$ and Q, respectively. For conductor-to-dielectric attached-electrode sliding-mode TENGs, the only geometrical structure difference is the absence of Dielectric 1. In this case, Metal 1 is not only the top triboelectric layer, but also the top electrode itself. When Metal 1 and Dielectric 2 are separated, due to the triboelectric effect, the upper surface at the separated region of Dielectric 2 has the uniform tribo-charges (surface density is $-\sigma$) and the same amount of tribocharges with opposite sign will exist on the surface of Metal 1. Therefore, at the OC condition (MACRS), the total amount of charges on the bottom electrode is 0. For the ease of physical understanding, the tribo-charges on the dielectric surface in the overlapped region has been deemed to cancel the opposite tribo-charge portions on the top metal layer, with the density of σ and amount of $\sigma w(l-x)$. Thus, in our model, the total amount of charges on the top electrode is σwx.

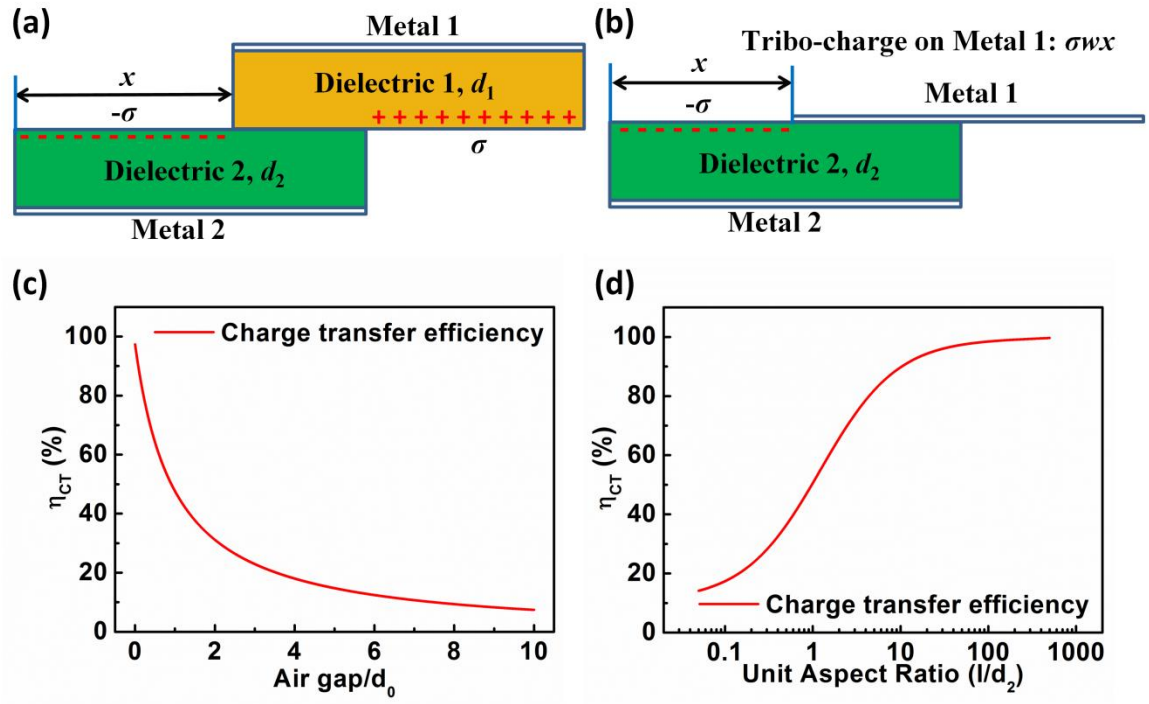

Figure 3-2. Theoretical models for (a) Dielectric-to-dielectric attached-electrode parallel-plate sliding-mode TENG and (b) Conductor-to-dielectric attached-electrode parallel-plate sliding-mode TENG. (c-d) Influence of (c) air gap size and (d) dielectric aspect ratio on the charge transfer efficiency of conductor-to-dielectric sliding-mode TENG when a full separation has been reached. The dielectric constant is 2 in this calculation. Reproduced from reference [24]. Copyright from 2013 Wiley.

The analytical equation for the general case of attached-electrode sliding-mode TENGs cannot be derived and rigorous theoretical analysis can only base on the numerical method. But in the practical applications, since l is always much larger than d_1 and d_2 and x is always smaller than $0.9l$ (because of the difficulty of perfect alignment of the two dielectric surfaces), an approximate analytical V-Q-x relationship can be derived when the edge effect can be neglected under the above conditions.

To derive the V-Q-x relationship, the analytical estimation of $C(x)$ and $V_{OC}(x)$ must first be obtained. We take the dielectric-to-dielectric case as an example. The capacitance C is first deducted. Since the thickness of the dielectrics is much smaller than their length, the capacitor between the overlapped region is the dominate part of the total

capacitance as long as the two dielectrics are not close to thoroughly separated. Therefore, utilizing the parallel-plate capacitor model, the total capacitance C can be estimated by the following equation:

$$C = \frac{\varepsilon_0 w(l-x)}{d_0} \qquad (3.12)$$

where d_0 is the effective dielectric thickness as defined in equation 3.7.

V_{OC} can be estimated by understanding the charge distribution. Since the length of the dielectrics is much larger than the thickness, we can assume in each region, the metal electrodes work as infinite plates. Under this approximation, the charge distribution is uniform in each region, and the electric field is uniform along the Y-direction inside the dielectrics. (This conclusion can also be verified through FEM calculation results[24]). Therefore, in an ideal case, the absolute value of surface charge density is σ for the non-overlapped region. For the overlapped region, the charge density is still uniform. Thus, the charge density at the overlapped region can be calculated through the 0 total charges at each electrode under OC conditions. The ideal charge distribution under OC condition (utilizing MACRS) can be approximated by the following equations:

For the non-overlapped region of the bottom electrode: $\rho = \sigma$ (3.13a)

For the overlapped region of the bottom electrode: $\rho = -\frac{\sigma x}{l-x}$ (3.13b)

For the non-overlapped region of the top electrode: $\rho = -\sigma$ (3.13c)

For the overlapped region of the top electrode: $\rho = \frac{\sigma x}{l-x}$ (3.13d)

Utilizing the charge distribution shown above and Gauss Theorem, V_{OC} can be easily estimated as:

$$V_{OC} = \frac{\sigma x d_0}{\varepsilon_0 (l-x)} \qquad (3.14)$$

So the *V*-*Q*-*x* relationship for attached-electrode sliding-mode TENGs when the edge effect can be neglected can be shown as:

$$V = -\frac{1}{C}Q + V_{OC} = -\frac{d_0}{w\varepsilon_0(l-x)}Q + \frac{\sigma d_0 x}{\varepsilon_0(l-x)} \quad (3.15)$$

For conductor-to-dielectric TENGs when the edge effect can be neglected, similar analysis shows the same results.

The electrostatic induction process of attached-electrode sliding-mode TENGs can also be thoroughly understood through the node discussion similar to the attached-electrode contact-mode TENGs. For simplicity, we take the conductor-to-dielectric attached-electrode sliding-mode TENGs as an example mainly because it only has one tribo-charged surface and we only analyze the capacitance distribution at the two ends ($x = 0$ and $x = x_{max} > l$). When $x = 0$, the capacitance between the tribo-charged dielectric surface and the top electrode is infinity while the capacitance between the tribo-charged dielectric surface and the bottom electrode is a finite large number, so the ratio between these two capacitances is infinity. When a full separation has already been reached, the capacitance between the tribo-charged dielectric surface and the top electrode is nearly 0 while the capacitance between the tribo-charged dielectric surface and the bottom electrode maintains still same, so the ratio between these two capacitances is now 0. This change of capacitance ratio due to the change of the relative position of tribo-charged surface will induce electron transfer between the electrodes under SC condition, as shown in equation 3.10. From the above discussion, the detailed working mechanism of attached-electrode sliding-mode TENGs is almost the same as that of attached-electrode contact-mode TENGs and the maximum charge transfer efficiency for this kind of TENG can also reach 100%.

From the above derivation, the intrinsic output characteristics of attached-electrode sliding-mode TENGs have the following properties. Their Q_{SC} is linearly proportional to the separation distance x while their inherent capacitance is linearly proportional to the length of the overlapped region (l-x). For open-circuit voltage, it increases dramatically when x is close to l due to the quick decrease of the capacitance.

One important consideration for attached-electrode sliding-mode TENGs is that their output is very sensitive to the gap between the surfaces of the two triboelectric layers. For example, if the thickness of such gap is the same as d_0, the capacitance between the tribo-charged dielectric surface and the top electrode when $x = 0$ is the same with the other capacitance. And the capacitance ratio can only change from 1 to 0 when x changes from 0 to x_{max}. Therefore, the charge transfer efficiency will be degraded to only 50%, as shown in Figure 3-2c. Since d_0 is always a small number, the gap tolerance of attached-electrode sliding-mode TENGs is poor, which can be improved by utilizing sliding-mode freestanding TENGs described in the following section.

Besides, another important consideration for attached-electrode sliding-mode TENGs is the edge effect.[24] When the thickness of the dielectrics is comparable to their length, strong edge effect will dominate the output and the charge transfer efficiency will be strongly degraded. Figure 3-2d shows the FEM simulation results for a conductor-to-dielectric attached-electrode TENG whose dielectric constant is 2. When the aspect ratio of length and dielectric thickness reduces from 500 to 0.05, the charge transfer efficiency reduces from nearly 100% to about 14%. Usually the edge effect can be ignored in practical attached-electrode sliding-mode TENGs with only one unit. However, this

effect will become dominant in attached-electrode grating-structured TENGs when the grating is fine enough, which we will discuss in detail in the following section.

3.3 Single-electrode triboelectric generators

Traditional attached-electrode contact-mode or sliding-mode TENGs require one electrode and the corresponding lead to be attached to the moving part of the devices, which limits their applicability. To overcome this drawback, some new structure of TENGs that eliminates the moving electrode has been demonstrated, which include single-electrode TENGs (SETENGs) and freestanding-triboelectric-layer nanogenerators (FTENGs). In this section, we will discuss the fundamental working mechanism of SETENGs.[26] There are also many experimental demonstrations for SETENGs.[18,19] In SETENGs, only one electrode is attached to (or serves as) the triboelectric layer (called primary electrode). The other electrode serves as an electric potential reference and can be placed anywhere in the space, even directly be the ground (called reference electrode). The function of the two electrodes in SETENGs is not equal to each other. Similar to attached-electrode triboelectric generators, SETENGs also have contact-mode and sliding-mode, which shows almost the same characteristics. Therefore, we mainly focus on the contact-mode SETENGs in the following discussions.

We first take the conductor-to-dielectric contact-mode SETENGs as an example. Its finite element model was built in 2-Dimensional to simplify the numerical calculation without losing its inherent physics meaning, as shown in Figure 3-3a. One dielectric plate and one metal electrode (primary electrode) are stacked face to face to form the triboelectric pair, with the same length of l and width of w. The thickness is d_1 for

Dielectric 1 and d_m for the primary electrode. As one typical configuration, the reference electrode of the same geometric size locates underneath the primary electrode, with a gap of g. The two electrodes are fixed and Dielectric 1 can move along the vertical direction under external mechanical force, with the distance between the two triboelectric layers defined as x. As a result of contact-electrification with the primary electrode, Dielectric 1 carries net negative charges with a density of $-\sigma$ on its bottom surface. Considering the excellent insulation properties of the polymer and the nature of contact electrification, it can be assumed that the charges are uniformly distributed on the surface at macro scale with negligible decay. At the same time, there will be equal amount (σwl) of positive charges injected to the primary electrode through contact electrification. With Q defined as the transferred charges from the primary electrode to the reference electrode, the total amount of charges at the primary electrode and reference electrode under MACRS are σwl-Q and Q, respectively. [26]

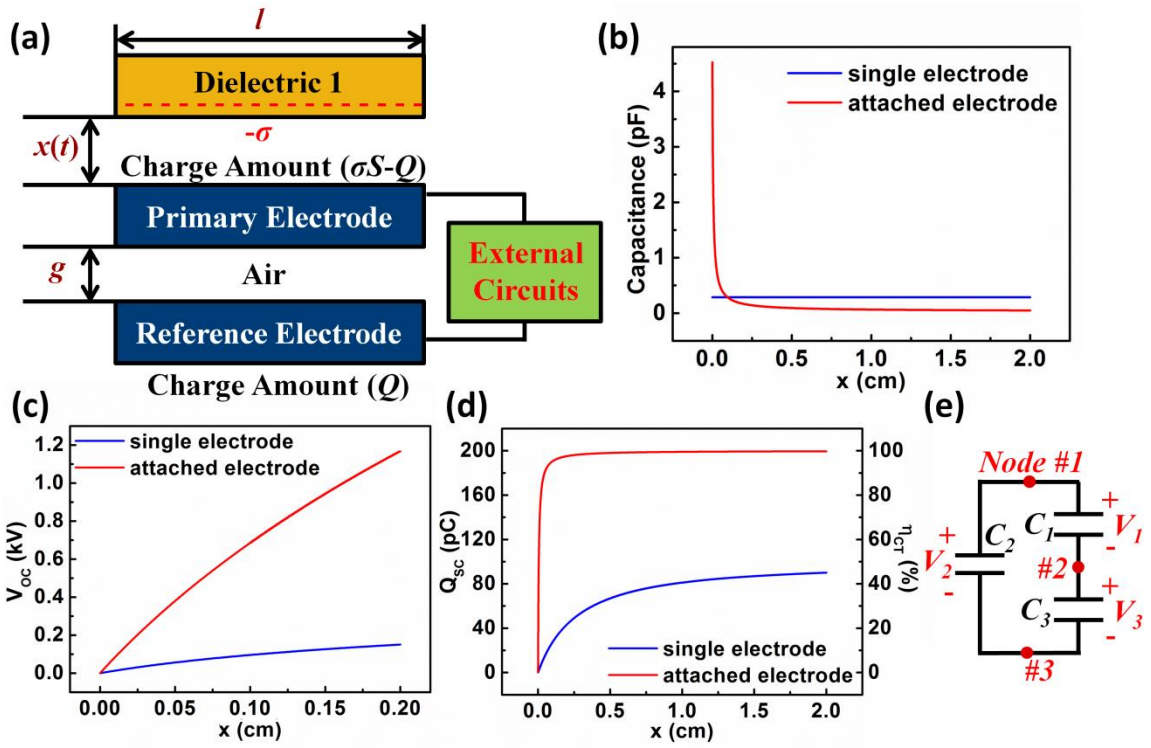

Figure 3-3. Intrinsic output characteristics of conductor-to-dielectric contact-mode SETENGs. (a) Structure of the FEM model. (b–d) Calculated (b) capacitance between the two electrodes, (c) open circuit voltage, and (d) transferred charges at short circuit condition of SETENGs at different *x*, together with comparison with results of attached-electrode TENGs. (e) Equivalent circuit model containing three capacitances for the SETENGs under open-circuit (OC) condition. Reproduced from reference [26]. Copyright from 2014 Wiley.

The FEM calculation results of C, V_{OC}, and Q_{SC} for the contact-mode SETENG are plotted in Figure 3-3b-d, in comparison with the corresponding results of the attached-electrode contact-mode TENG with the same size. (Detailed calculation parameter is listed in Table 3.1). Their characteristics are completely different. First, due to the fixture of the SETENG's electrodes, its C is nearly a constant (C_0) with the increase of x. However, for the attached-electrode structure, its C decreases quickly when the distance between the two electrodes is increasing. Secondly, in the SETENG, its V_{OC} quickly gets saturated at a value much lower than that of the attached-electrode structure. This is because when Dielectric 1 is far away from the electrodes, the influence of

Dielectric 1 on the electric field distribution around the electrodes is little. Therefore, further increase in x will contribute little to the increase of V_{OC}. Finally, in the SETENG, Q_{SC} slowly reached its saturation value, which is only half of the value for the attached-electrode structured TENG. When Dielectric 1 is far away from the electrodes, the tribo-charges generated are equally distributed between the two electrodes to maintain the two electrodes at the same electric potential. The maximized η_{CT} can only reach 50%, while η_{CT} for the attached-electrode TENGs can reach nearly 100% even when x is relatively small.

Table 3.1. Utilized parameters in the calculation of SETENG's output characteristics

Dielectric 1	$\varepsilon_{r1} = 2$, $d_1 = 100$ μm
Thickness of electrodes d_m	1 μm
Width of the structrue w	5 mm
Length of Dielectrics l	5 mm
Gap distance between electrodes g	1 mm
Tribo-charge surface density σ	8 μCm^{-2}
Maximum separation distance x_{max}	0.01 m
Average Velocity v	1 ms^{-1}

The degradation of output performance of SETENGs mainly comes from the electrostatic shield effect of the primary electrode, which can be analyzed from their equivalent circuit model.[26] The nodes are still first analyzed in the electrostatic system. For the above system in OC condition, the electric potential across the whole bottom surface of Dielectric 1 is nearly constant. Thus, the whole surface can be assumed as a node (Node 1). Similarly, the primary electrode and the reference electrode also serve as two nodes, which can be named as Node 2 and Node 3, respectively. Since every two nodes are connected by electric field lines, an equivalent capacitance is formed between

each of them, as shown in Figure 3-3e. Their capacitances C_1, C_2, and C_3 in the equivalent circuit only represent the capacitive effects from the direct electric line connection between every two nodes without crossing any charged objects (without electrostatic shield of the third obeject), so they are not actual capacitances that reflects all the electric line connection (both direct and non-direct) between the two nodes and can be directly measured.

As a quantitative relationship between the two categories of capacitance, the actual capacitance is the combination of these three capacitances. For example, the actual capacitance (C_b) between Node 1 and Node 3 contains two parts: C_2 and the serial connection of C_1 and C_3 that shows the capacitance effect of non-direct electric lines connection through Node 2, as given by:

$$C_b = C_2 + \frac{C_1 C_3}{C_1 + C_3} \qquad (3.16)$$

Similarly, the actual capacitances between Node 1 and Node 2 (C_a) and between Node 2 and Node 3 (C_0) can also be given as below:

$$C_a = C_1 + \frac{C_2 C_3}{C_2 + C_3} \qquad (3.17)$$

$$C_0 = C_3 + \frac{C_1 C_2}{C_1 + C_2} \qquad (3.18)$$

Under OC conditions (MACRS), the total charges on Node 1, 2, and 3 are -σwl, σwl, and 0, respectively. Thus, from basic characteristics of capacitances and charge conservation on each node, V_{OC}, Q_{SC} and η_{CT} can be given by ($C_1(x = 0)$ is close to infinity in the following equation):[26]

$$Q_{SC} = \frac{\sigma wl}{1 + \frac{C_1(x)}{C_2(x)}} - \frac{\sigma wl}{1 + \frac{C_1(x=0)}{C_2(x=0)}} = \frac{\sigma wl}{1 + \frac{C_1(x)}{C_2(x)}} \qquad (3.19)$$

$$\eta_{CT} = \frac{Q_{SC}}{\sigma w l} = \frac{1}{1 + \frac{C_1(x)}{C_2(x)}} - \frac{1}{1 + \frac{C_1(x=0)}{C_2(x=0)}} = \frac{1}{1 + \frac{C_1(x)}{C_2(x)}} \qquad (3.20)$$

$$V_{OC} = \frac{\sigma w l C_2}{C_1 C_2 + C_2 C_3 + C_3 C_1} \qquad (3.21)$$

Equation 3.19 and 3.20 are the same as the above equation in the attached-electrode case, which shows that the core electrostatic induction principle of SETENGs is the same with attached-electrode TENGs. However, in SETENGs, the trend of the capacitance is different from the attached-electrode TENG case. When x = 0, C_a goes to infinity while C_b and C_0 become equal with each other. Therefore, from Equation 3.16 – 3.18, C_1 goes to infinity while C_2 and C_3 are equal to $C_0/2$, which is a finite number. Therefore, the ratio C_1/C_2 is infinity. When x approaches to infinity, both C_a and C_b approach to 0 at the same rate. Therefore, both C_1 and C_2 approach to 0 with the ratio of C_1/C_2 approaching to 1. Thus, under this condition, the transferred charges is only half amount of the tribo-charges and the maximum charge transfer efficiency is only 50%.

From Equation 3.19-3.21, we observe that the capacitance C_2 is critically important for both V_{OC} and Q_{SC}. C_2 represents the portion of the electric lines directly connecting Node 1 and Node 3, without being electrostatically shielded by Node 2. If all the electric lines connections between the reference electrode and Dielectric 1 needs to come through the primary electrode (electrostatic shielded by the primary electrode), C_2 will be equal to 0, which will lead to no output from the SETENG. Therefore, SETENG with infinite area size will lead to zero output due to the fully electrostatic shield condition.

3.4 Freestanding-triboelectric-layer based triboelectric generators

The output performance of SETENGs is limited by the electrostatic shield effect of their primary electrodes and the maximum charge transfer efficiency can only reach 50%.[26] To overcome this drawback, another kind of fixed-electrode TENGs are designed with the tribo-charged surface alternatively approaching the two electrodes, which is the freestanding-triboelectric-layer based triboelectric generators (FTENGs).[29] Same as SETENGs, the moving object of an FTENG does not need to be connected to the TENG system as well.[20-23] FTENGs can also be utilized to harvest mechanical energy from any moving object. [22]However, unlike the SETENGs, FTENGs don't have this electrostatic shield effect problem. Besides, the output characteristics of contact-mode FTENGs (CFTENGs) and sliding-mode FTENGs (SFTENGs) are completely different and we will discuss their characteristics separately.

3.4.1 Contact-mode freestanding-triboelectric-layer based triboelectric generators

Two typical structures of CFTENGs are shown in Figure 3-4. [29] Figure 3-4a shows a typical structure for dielectric-freestanding-layer CFTENGs. A dielectric plate (thickness: d_1, relative dielectric constant: ε_{r1}) and two metal plates are stacked face to face, forming two triboelectric pairs. The two metal plates also serve as two electrodes. The total air gap thickness between these two metal plates is defined as g. After the dielectric plate being forced to contact with the two metal plates, both the top and the bottom surfaces of Dielectric 1 will have static triboelectric charges due to contact electrification. For simplicity, we assume the triboelectric charge density of both surfaces

is the same (-σ). At the same time, the two metal plates will have the same amount of positive charges in total because of charge conservation.

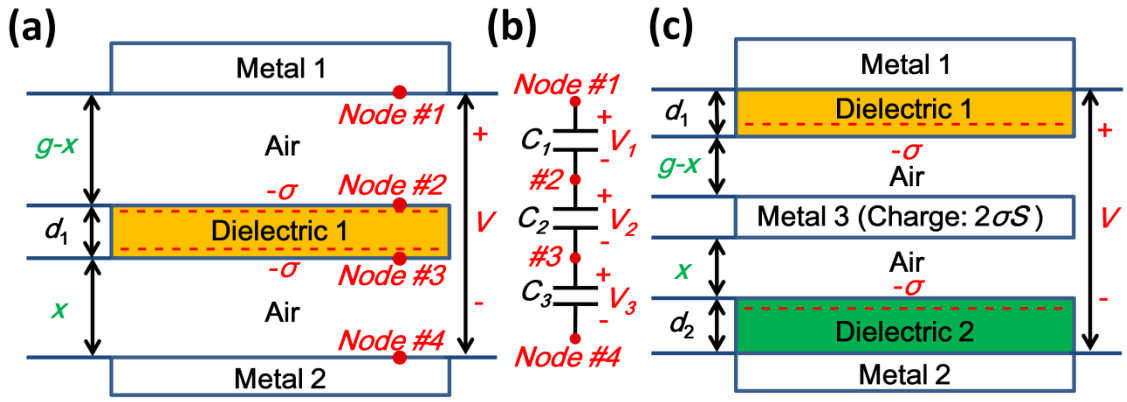

Figure 3-4. Theoretical models of contact-mode freestanding TENGs. (a) Model of a typical dielectric freestanding layer CFTENG. (b) Equivalent circuit model of the dielectric CFTENG electrostatic system. (c) Model of a typical metal freestanding layer CFTENG. Reproduced from reference [29] Copyright 2014 Elsevier.

The above system can be easily solved through Gauss's Law. But to fully show its inherent physics and working behavior, we still try to utilize the concept of nodes to analyze this electrostatic system. In practical applications, the size of the metal electrode is always much larger than the air gap. Therefore, the area size of the freestanding contact-mode TENG (S) is seen as infinitely large and the edge effect can be ignored. As a result, the electric potential on metal 1, metal 2, the top and bottom surface of dielectric 1 are all constant, so these 4 surfaces can be seen as 4 nodes in this electrostatic system. The electrical line connection between every two nodes forms an equivalent capacitance between them. Since the area size (S) is assumed as infinitely large, the electrical line connection between every two non-adjacent nodes (for example, Node 1 & 3) is fully blocked by the intermediate node (for example, Node 2). Therefore, only three capacitances exist in the equivalent circuit model of this electrostatic system, as shown in

Figure 3-4b. The total capacitance between the two electrodes (Node 1 & 4) is the serial connection of C_1, C_2, and C_3, which can be easily given by the following equation.

$$C = \frac{1}{\frac{1}{C_1} + \frac{1}{C_2} + \frac{1}{C_3}} = \frac{\varepsilon_0 S}{d_0 + g} \quad (3.22)$$

Inside equation 3.22, the definition of the effective dielectric thickness d_0 is the same with the previous definition.

The charge distribution under short circuit (SC) condition when Node 1 and Node 4 have the same electrical potential is then analyzed. The charges on each node need to be deducted to solve this electrostatic system. For both Node 2 and 3, the amount of charges on the node is $-\sigma S$. In addition, because of charge conservation, we only know that the total charges on Node 1 and 4 are $2\sigma S$, but the detailed charge distribution is still unknown. Under SC condition, we set the total charges on metal 1 (Node 1) is Q_1 and the total charges on metal 2 (Node 4) is Q_2 ($Q_2 = 2\sigma S - Q_1$). From the basic electrodynamics theory and charge conservation, the total charges on metal 1 and 2 can be easily solved as:

$$Q_1 = \sigma S \frac{\frac{1}{C_2} + \frac{2}{C_3}}{\frac{1}{C_1} + \frac{1}{C_2} + \frac{1}{C_3}} \quad (3.23a) \qquad Q_2 = \sigma S \frac{\frac{2}{C_1} + \frac{1}{C_2}}{\frac{1}{C_1} + \frac{1}{C_2} + \frac{1}{C_3}} \quad (3.23b)$$

In practical applications, the effective dielectric thickness of the dielectrics d_1/ε_{r1} is always negligible compared to the air gap and C_2 can be seen as infinitely large. Thus, equation (3.23a and b) can be further simplified to:

$$Q_1 \approx \sigma S \frac{\frac{2}{C_3}}{\frac{1}{C_1} + \frac{1}{C_3}} = \frac{2\sigma S}{1 + \frac{C_3}{C_1}} \quad (3.24a) \qquad Q_2 \approx \frac{2\sigma S}{1 + \frac{C_1}{C_3}} \quad (3.24b)$$

From Equation 3.24a and 3.24b, the basic working mechanism of CFTENGs can be easily observed. When $x = 0$, C_3 is infinity, as a result, Q_1 is close to 0 and Q_2 is approximately $2\sigma S$. Under this condition, all the positive tribo-charges are attracted to the bottom electrode by the negative charges on the surface of dielectric 1. While when $x = g$, C_1 is infinity and all the positive charges on the electrodes are attracted to Metal 1. Therefore, if Dielectric 1 is under a vibration inside the air gap, charges will alternatively flow between Metal 1 and Metal 2 due to the change of C_1/C_3, forming an AC short circuit current. Same as all previous TENGs, the change of this capacitance ratio induced by the change of Dielectric 1 position can drive electrons to flow under SC conditions between the two electrodes.

Under MACRS, the short circuit transferred charges (Q_{SC}) and open-circuit voltage can be easily obtained as:

$$Q_{\mathrm{SC}} = Q_1(x) - Q_1(x = 0) = \frac{2\sigma S x}{d_0 + g} \quad (3.25)$$

$$V_{OC} = \frac{2\sigma x}{\varepsilon_0} \quad (3.26)$$

Therefore, the governing equation for this CFTENG, which is its *V*-*Q*-*x* relationship, can be shown as:[29]

$$V = -\frac{1}{C}Q + V_{\mathrm{OC}} = -\frac{d_0 + g}{\varepsilon_0 S}Q + \frac{2\sigma x}{\varepsilon_0} \quad (3.27)$$

Besides the dielectric-freestanding-layer CFTENGs, another important category is metal-freestanding-layer CFTENGs, as shown in Figure 3-4c. The working principle of metal-freestanding-layer CFTENGs is very similar to the dielectric-freestanding-layer case. Similar to the previous discussed attached-electrode contact-mode TENGs, metal

can be simply seen as dielectrics with 0 thickness to calculate d_0 and the derived equations above are all applicable to metal CFTENGs.

With the above information, the comparison of the intrinsic output characteristics of CFTENGs and attached-electrode contact-mode TENGs can be provided. Their V_{OC} characteristics are similar to each other, which are both linearly proportional to x. However, their inherent capacitance and short-circuit transferred charges characteristics are completely different. First, the inherent capacitance of CFTENGs is constant and independent of x while that of contact-mode attached-electrode TENGs decreases when x increases. In addition, Q_{SC} of CFTENGs is also linearly proportional to x while that of attached-electrode TENGs has a saturation trend.

3.4.2 Sliding-mode freestanding-triboelectric-layer based triboelectric generators

Besides CFTENGs, another important category is the sliding-mode FTENGs (SFTENGs) based on in-plane charge separation mechanism.[29] Based on the freestanding material, SFTENGs have two subcategories, dielectric SFTENGs whose freestanding materials only contain dielectrics and metal SFTENGs whose freestanding materials contains metal. The basic model of these two SFTENGs is shown in Figure 3-5a and b. In the SFTENGs, Metal 1 and 2 are placed in the same plane with a gap g to form two electrodes. A freestanding layer with the same size of Metal 1 stands on the top of the metal electrodes and the distance between the bottom surface of freestanding layer and Metal 1 is defined as the freestanding height h. The width of this structure is defined as w. For dielectric SFTENGs shown in Figure 3-5a, the freestanding layer only contains a layer of dielectrics. And for metal SFTENGs, a thin layer of metal is deposited at the

backside of the dielectric freestanding layer. These two structures look very similar, but unlike CFTENGs, the freestanding material will strongly influence the output characteristics of the SFTENGs.

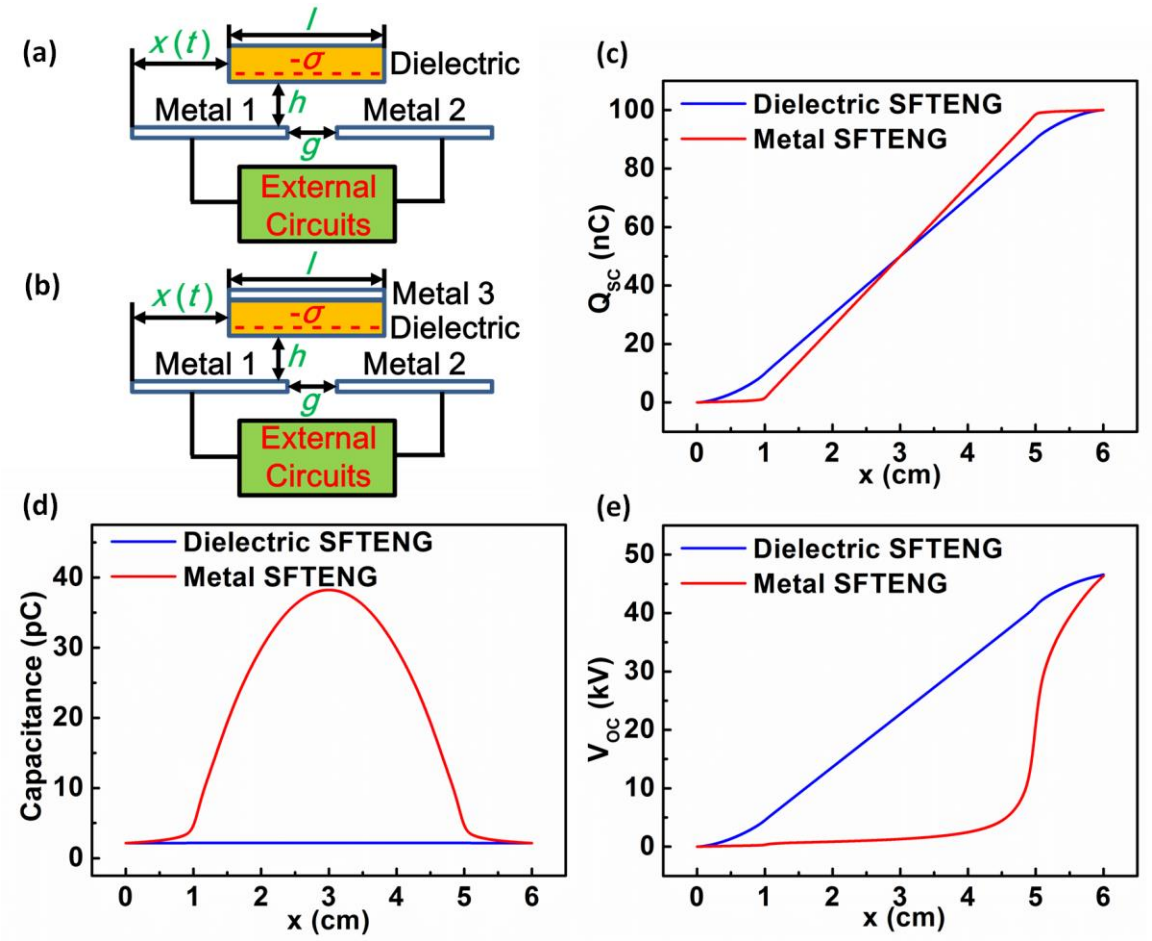

Figure 3-5. Models and basic output characteristics of sliding-mode freestanding TENGs. (a) FEM model of a typical dielectric SFTENG. (b) FEM model of a typical metal SFTENG. (c-e) Influence of freestanding layer material on the basic output characteristics: (c) short-circuit transferred charges under MACRS, (d) total capacitance between the two electrodes, and (e) open-circuit voltage under MACRS. Reproduced from reference [29]. Copyright 2014 Elsevier.

The main working principle of SFTENGs is very similar to that of CFTENGs. The node concept can still be utilized to analyze their working principle. We first analyze dielectric SFTENGs. In contrast to CFTENGs, since the electrical potential of the dielectric bottom surface is not a constant, this surface could not be seen as a single node.

The electric potential superposition principle is utilized to solve this problem. First, we assume that only a small region of dk in the bottom dielectric surface (the distance of this region to the left edge of the bottom dielectric surface is k) contains the tribo-charges with a density of $-\sigma$, and correspondingly the total charges on metal 1 and 2 are σwdk. Utilizing the similar derivation method we utilized above, the total charges on metal 1 and 2 (dQ_1 and dQ_2) under SC conditions because of these tribo-charges can be given by the following equations, where $C_i(k)$ states for the capacitance between this small surface σwdk and metal i:

$$\mathrm{d}Q_1 = \frac{\sigma w \mathrm{d}k}{1+\frac{C_2(k)}{C_1(k)}} \quad (3.28a); \qquad \mathrm{d}Q_2 = \frac{\sigma w \mathrm{d}k}{1+\frac{C_1(k)}{C_2(k)}} \quad (3.28b)$$

Because of the superposition principle of the electrostatic field, the total charges on metal 1 and metal 2 considering the whole charges on the dielectric surface is the integration of each small tribo-charged region, which can be shown as:

$$Q_1 = \sigma w \int_0^l \frac{\mathrm{d}k}{1+\frac{C_2(k)}{C_1(k)}} \quad (3.29a); \quad Q_2 = \sigma w \int_0^l \frac{\mathrm{d}k}{1+\frac{C_1(k)}{C_2(k)}} \quad (3.29b)$$

Therefore, $Q_{SC,final}$ can be shown as:

$$Q_{SC,final} = \int_0^l \frac{\sigma w \mathrm{d}k}{1+\left(\frac{C_2(k)}{C_1(k)}\right)_{x=g+l}} - \int_0^l \frac{\sigma w \mathrm{d}k}{1+\left(\frac{C_2(k)}{C_1(k)}\right)_{x=0}} \quad (3.30)$$

When $x = 0$, the tribo-charged dielectric surface is much closer to metal 1 than to metal 2, so the ratio $C_2(k)/C_1(k)$ is close to 0 for all the k values. Therefore, Q_1 will be approximately σwl and Q_2 will be approximately 0 from equation 3.29. On the contrast, the ratio $C_2(k)/C_1(k)$ is close to infinity for all the k values when $x = g+l$. Therefore, Q_1 will be approximately 0 and Q_2 will be approximately σwl. Thus, $Q_{SC,final}$ can reach σwl

and the charge-transfer efficiency (η_{CT}) can reach 100%. Same as CFTENGs, the change of the ratio of these two capacitances with the change of x serves as the driving force for electrons to transfer between the two electrodes.

For metal SFTENGs, the basic electrostatic induction principle is the same as the dielectric SFTENGs. Therefore, as shown in Figure 3-5c, the numerically calculated trend of Q_{SC} profile (under MACRS) is quite similar to that of dielectric SFTENGs. (Detailed numerical calculation parameter is listed in Table 3.2). However, unlike CFTENGs, their characteristics of capacitance and V_{OC} are completely different from each other, as shown in the numerical results presented in Figure 3-5d and e. The capacitance profile of dielectric SFTENGs is nearly constant when the position of the freestanding layer changes. However, for metal SFTENGs, the capacitance when the freestanding layer is in the middle is several orders larger than that when the freestanding layer is at the two ends. This capacitance difference leads to the difference of their V_{OC} profile. Since the capacitance of metal-SFTENGs in the middle region is much larger than that of dielectric-SFTENGs, so from equation 2.3, the open-circuit voltage of metal-SFTENGs in this region will be much smaller than that of dielectric-SFTENGs. And when x is close to $g+l$, since the capacitance of the metal-SFTENG quickly dropped to the value close to the dielectric-SFTENG, the open-circuit voltage of the metal-SFTENG also quickly increase to a value close to the dielectric-SFTENG. Therefore, although the final open-circuit voltage values of the two SFTENGs are almost the same, the metal-SFTENG curve is much more non-linear than the dielectric-SFTENG curve and the maximum slope of the metal-SFTENG curve is much larger than that of the dielectric-SFTENG curve.

Table 3.2. Parameters utilized in the calculation of output characteristics for both dielectric and metal SFTENGs

Structure Component	Parameter Utilized
Dielectric	d = 500 μm, ε_r = 2
Width of the structure w	0.1 m
Length of electrode l	0.05 m
Thickness of metal electrode and freestanding layer	d_m = 10 μm
Tribo-charge surface density σ	20 μCm^{-2}
Electrode gap g	1 cm
Freestanding height h	0 mm
Motion average velocity v	1 ms^{-1}

These differences in capacitance and V_{OC} profiles are mainly from the charge redistribution inside the metal freestanding layer. In dielectric-SFTENGs, the charges are not free to move. Since the relative dielectric constant of the commonly utilized dielectrics is not much larger than the relative dielectric constant of the air (always in the range of 2-4), the change of the capacitances due to the change of the freestanding-layer position is little. However, the charge on the surface of metal freestanding layer can redistribute to keep the electrical potential of the metal freestanding layer constant, which will lead to huge disturbance of the electrostatic field distribution. Therefore, the capacitance of metal-SFTENGs has two parts. The first part is the direct parasitic capacitance between these two electrodes, which can be analogous to the capacitance of dielectric SFTENGs. The second part is the serial connection of the capacitance between metal 1 and metal 3 (C_{f1}) and metal 3 and metal 2 (C_{f2}), which is the unique capacitance part of metal SFTENGs. When both the dielectric thickness and the freestanding height h are not too large, the contribution of this serial connection is very significant to the total capacitance. At the two ends, either C_{f1} or C_{f2} will close to 0 because the metal freestanding layer only have overlapping region with one electrode, so the total

capacitance of metal SFTENGs is close to the capacitance of dielectric SFTENGs. When x equals to $(g+l)/2$, C_{f1} and C_{f2} will be the same and their serial connection gets its maximum, leading to the largest total capacitance under this condition. At the same time, strong charge redistribution has been observed in the inner surface of the metal freestanding layer.

3.5 Summary of the triboelectric nanogenerator fundamental modes

In summary, the fundamental working mechanism of TENGs is a conjugation of contact electrification and electrostatic induction. Through contact electrification, electrostatic charges can be generated and kept on the dielectric surface. There are two equivalent capacitances that will form between the tribo-charged dielectric surface and the two metal electrodes, respectively. The change of the ratio of these two capacitances due to the change of the position of the dielectric will induce electrons to transfer between the two metal electrodes under SC condition. The difference of the capacitances' changing behavior gives rise to the different TENG fundamental modes. The capacitance changing trend of all TENG fundamental modes is summarized in Table 3.3.

Table 3.3. Comparison of different TENG fundamental modes

	Attached electrode contact-mode and sliding-mode TENGs	Single electrode TENGs	Freestanding TENGs
Core working mechanism	$\eta_{CT} = \frac{1}{1+\frac{C_1(x=x_{max})}{C_2(x=x_{max})}} - \frac{1}{1+\frac{C_1(x=0)}{C_2(x=0)}}$		
$C_1(x=0)$	infinity	infinity	infinity
$C_2(x=0)$	Finite non-zero value	Finite non-zero value	Finite non-zero value
$C_1(x=x_{max})$	infinitesimal	infinitesimal	Finite non-zero value
$C_2(x=x_{max})$	Finite non-zero value	infinitesimal	infinity
$C_1(x=0)/ C_2(x=0)$	infinity	infinity	infinity
$C_1(x=x_{max})/C_2(x=x_{max})$	0	1	0
η_{CT}	100%	50%	100%

CHAPTER 4

TRIBOELECTRIC NANOGENERATOR RESISTIVE LOAD CHARACTERISTICS

4.1 Resistive load characteristics and "three-working-region" behavior

Resistive load is the simplest load case for TENGs. When TENGs are connected with a resistive load *R*, the equivalent circuit of the whole system is shown in Figure 4-1a. Utilizing Kirchhoff's law, the governing equation can be easily given by: [24,25]

$$V = R\frac{\mathrm{d}Q}{\mathrm{d}t} = -\frac{1}{C}Q + V_{\mathrm{OC}} \qquad (4.1)$$

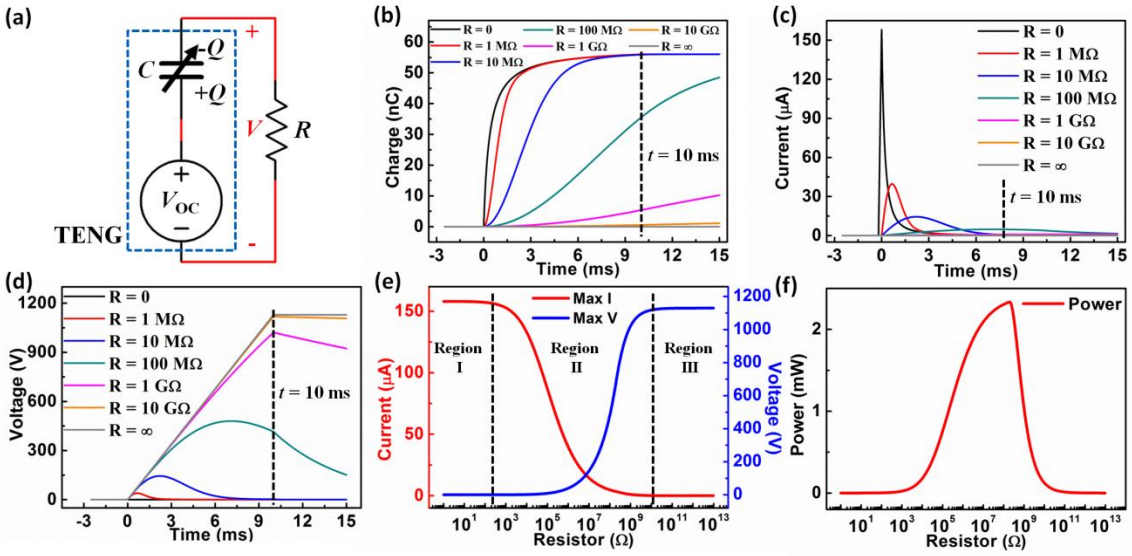

Figure 4-1. Theoretical calculated TENG resistive-load output characteristics under uniform velocity separation. The top plate reaches the maximum separation distance and stops moving at t = 10 ms. (a) Equivalent circuit model of the whole TENG system. (b) Real-time transferred charge-time relationship at different load resistances. (c) Real-time current-time relationship at different load resistances. (d) Real-time voltage-time relationship at different load resistances. (e) The influence of the load resistance on the magnitude of the output current and voltage. Three working regions are marked. (f) The influence of the load resistance on the instantaneous power output. Reproduced from reference [25]. Copyright 2013 Royal Society of Chemistry.

The above equation is a first-order differential equation and can be easily solved by specifying the initial boundary condition $Q(t = 0)$. There are two types of boundary conditions that are most commonly utilized. First, we can consider a very common case that the device has stopped at the equilibrium position ($x = 0$) for a long time and electrostatic equilibrium has been reached before the motion process. If V_{OC} are utilized its value under MACRS, the boundary condition is $Q\ (t = 0) = 0$. Second, if the TENG is under a periodic motion with a specific period, output from any initial boundary condition will gradually converge to a periodic output wave after the first few periods, which is the steady-state. To solve the steady-state solution, periodic boundary condition must be utilized, which is $Q\ (t = 0) = Q\ (t = T)$, where T is the period of the motion process. For simplicity, in this section, we mainly utilized the boundary condition $Q\ (t = 0) = 0$, which will not affect the main conclusion. Under this boundary condition, equation 4.1 can be solved as:

$$Q(t) = \frac{1}{R}\exp\left[-\frac{1}{R}\int_0^t \frac{\mathrm{d}t}{C(x(t))}\right]\int_0^t V_{OC}(x(t))\exp\left[\frac{1}{R}\int_0^t \frac{\mathrm{d}t}{C(x(t))}\right]\mathrm{d}t \qquad (4.2a)$$

$$I(t) = \frac{V_{OC}}{R} - \frac{1}{R^2C}\exp\left[-\frac{1}{R}\int_0^t \frac{\mathrm{d}t}{C(x(t))}\right]\int_0^t V_{OC}(x(t))\exp\left[\frac{1}{R}\int_0^t \frac{\mathrm{d}t}{C(x(t))}\right]\mathrm{d}t \quad (4.2b)$$

$$V(t) = V_{OC} - \frac{1}{RC}\exp\left[-\frac{1}{R}\int_0^t \frac{\mathrm{d}t}{C(x(t))}\right]\int_0^t V_{OC}(x(t))\exp\left[\frac{1}{R}\int_0^t \frac{\mathrm{d}t}{C(x(t))}\right]\mathrm{d}t \quad (4.2c)$$

The above equations are a bit complicated. As a typical example, we can consider an attached-electrode contact-mode TENG under a constant velocity motion process.[25] For attached-electrode contact-mode TENG, the above equations can be simplified as:

$$Q(t) = \sigma S - \sigma S\exp[-\tfrac{1}{RS\varepsilon_0}(d_0 t + \textstyle\int_0^t x(t)\mathrm{d}t)] - \tfrac{\sigma d_0}{R\varepsilon_0}\exp[-\tfrac{1}{RS\varepsilon_0}(d_0 t + \int_0^t x(t)\mathrm{d}t)] \times \int_0^t \exp\left[\tfrac{1}{RS\varepsilon_0}\left(d_0 z + \textstyle\int_0^z x(z)\mathrm{d}z\right)\right]\mathrm{d}z \qquad (4.3a)$$

$$I(t) =$$

$$-\frac{\sigma d_0}{R\varepsilon_0} + \frac{\sigma(d_0+x(t))}{R\varepsilon_0}\exp[-\frac{1}{RS\varepsilon_0}(d_0 t + \int_0^t x(t)\mathrm{d}t)] + \frac{\sigma d_0}{R\varepsilon_0} \times \frac{d_0+x(t)}{RS\varepsilon_0}\exp[-\frac{1}{RS\varepsilon_0}(d_0 t +$$

$$\int_0^t x(t)\mathrm{d}t)] \times \int_0^t \exp\left[\frac{1}{RS\varepsilon_0}\left(d_0 z + \int_0^z x(z)\mathrm{d}z\right)\right]\mathrm{d}z \qquad (4.3b)$$

$$V(t) =$$

$$-\frac{\sigma d_0}{\varepsilon_0} + \frac{\sigma(d_0+x(t))}{\varepsilon_0}\exp[-\frac{1}{RS\varepsilon_0}(d_0 t + \int_0^t x(t)\mathrm{d}t)] + \frac{\sigma d_0}{\varepsilon_0} \times \frac{d_0+x(t)}{RS\varepsilon_0}\exp[-\frac{1}{RS\varepsilon_0}(d_0 t +$$

$$\int_0^t x(t)\mathrm{d}t)] \times \int_0^t \exp\left[\frac{1}{RS\varepsilon_0}\left(d_0 z + \int_0^z x(z)\mathrm{d}z\right)\right]\mathrm{d}z \qquad (4.3c)$$

In a special case of uniform motion at a constant velocity *v* (shown as equation 4.4), the above equations can be further simplified to Equation 4.5a-c, as shown below.

$$x = vt \ \left(t < \frac{x_{max}}{v}\right) \quad (4.4a) \qquad x = x_{\max} \ \left(t \geq \frac{x_{max}}{v}\right) \quad (4.4b)$$

$$Q(t) = \sigma S[1 - \exp(-At - Bt^2) + \sqrt{2}F\exp(-At - Bt^2) \times \mathrm{Dawson}\left(\frac{F}{\sqrt{2}}\right) -$$

$$\sqrt{2}F \times \mathrm{Dawson}(\frac{F}{\sqrt{2}} + \sqrt{B}t)] \qquad (4.5a)$$

$$I(t) = \sigma S\left[\exp(-At - Bt^2)(A + 2Bt) - \sqrt{2}F \times \exp(-At - Bt^2)(A + 2Bt) \times\right.$$

$$\left.\mathrm{Dawson}\left(\frac{F}{\sqrt{2}}\right) - A + 2A(\frac{F}{\sqrt{2}} + \sqrt{B}t) \times \mathrm{Dawson}(\frac{F}{\sqrt{2}} + \sqrt{B}t)\right] \qquad (4.5b)$$

$$V(t) = \sigma SR\left[\exp(-At - Bt^2)(A + 2Bt) - \sqrt{2}F \times \exp(-At - Bt^2)(A +\right.$$

$$\left.2Bt) \times \mathrm{Dawson}\left(\frac{F}{\sqrt{2}}\right) - A + 2A(\frac{F}{\sqrt{2}} + \sqrt{B}t) \times \mathrm{Dawson}(\frac{F}{\sqrt{2}} + \sqrt{B}t)\right] \qquad (4.5c)$$

The constants *A*, *B*, and *F* are defined by:

$$A = \frac{d_0}{RS\varepsilon_0} \quad (4.6a) \qquad B = \frac{v}{2RS\varepsilon_0} \quad (4.6b) \qquad F = \frac{A}{\sqrt{2B}} = \frac{d_0}{\sqrt{RS\varepsilon_0 v}} \quad (4.6c)$$

The Dawson's integral (Dawson(*x*)) in the above expressions is shown as:

$$\mathrm{Dawson}(x) = \exp(-x^2)\int_0^x \exp(y^2)\,\mathrm{d}y \qquad (4.7)$$

The numerical calculated results are shown in Figure 4-1b-f. (Parameters utilized are listed in Table 4.1) The detailed profiles of the charge, current, and voltage relationships at different loads are shown in Figure 4-1b-d. Under short-circuit conditions, the charge transfers at the fastest speed. For a relatively small R, Q can still get its saturation value when the top electrode stops moving (t= 10 ms). However, when R is more than 100 MΩ, at t= 10 ms, the charge cannot get saturated due to the limit of the charge transfer rate by the resistor, resulting in the unstopped charge transfer from metal 1 to metal 2 after t= 10 ms. Therefore, the current is a peak-shape when R is small while the current continues increasing during the plate movement when R is large. The voltage has the same profile with the current, but a different trend in magnitude. The peak values of the voltage, current and power on different loads are displayed in Figure 4-1e and f. It can be clearly observed that the operation of the TENG can be divided into three working regions. First, In Region I where the resistance is low (0.1-1000 Ω), the peak current has little drop from the short-circuit condition, which is due to the similar charge transfer process in comparison with that of the short-circuit condition. As a result, the maximum voltage is approximately proportional to the external resistance. On the other hand, when the resistor is larger than 1 GΩ (Region III), the output characteristics are close to the open-circuit condition, in which the maximum voltage saturates at V_{OC}. The medium range of the resistance is Region II, where the maximum current drops dramatically but the maximum voltage increases at a reverse trend. Around 100 MΩ inside this region, the TENG reaches its maximum instantaneous output power.

Table 4.1. Parameters utilized in the resistive-load characteristic calculation

Structure Component	Parameter Utilized
Dielectric 1	Metal, $d_1 = 0$ μm
Dielectric 2	$d_2 = 125$ μm, $\varepsilon_{r2} = 3.4$
Area size of Dielectrics S	58.0644 cm^2 (9 $inch^2$)
Tribo-charge surface density σ	10 μCm^{-2}
Maximum separation distance x_{max}	0.001 m
Average Velocity v	0.1 m/s

This unique output characteristic of TENGs can be interpreted both physically and mathematically.[25] In physics, we can understand this unique characteristic from two different views. As an intuitive sense, we can explain this three-working-region behavior from the charge transfer rate point of view. The working principle of the TENG is a conjunction of the triboelectric process and the electrostatic induction. When the tribo-charges are separated, an induced voltage will be generated between the two electrodes, which will drive the electrons to flow from electrode 2 to electrode 1. The electric field from these transferred charges will screen the original electric field from the tribo-charges. The charge accumulation rate at SC condition is the maximum charge transfer rate, which is determined by the mechanical motion. However, as there is an external load with certain resistance, the resistor will limit the real charge transfer rate, making it lower than that at the SC condition. When the load resistance is very small, this limitation is not obvious so that the rate can still catch up with the maximum rate determined by the moving mode, enabling the Q to stay close to Q_{SC} in Region I. When the load resistance continues to increase and gets into Region II, it begins to significantly limit the charge flow rate, making the charge accumulation curve deviate downward from Q_{SC}. As the load resistance is large enough, the transfer of electrons from metal 2 to metal 1 is rather slow, which results in a very small current. The induced voltage between the two

electrodes will hold for a long time due to the little screening effect, with the magnitude approaching V_{OC}. This is the Region III of the TENG.

Besides the explanation from charge transfer rate, this unique three-working-region behavior can also be understood from the impedance match between the inherent TENG capacitance and the load resistance, although now there is no strict definition of the impedance of the inherent TENG capacitance because the TENG capacitance is time-variant and V_{OC} is also not a pure harmonic function. When the load resistance is small, its impedance is much smaller than the impedance of the TENG capacitance. Thus, the total impedance is dominated by the TENG inherent capacitance and the output current remains almost unchanged when the resistance increases. When the load resistance is large enough, its impedance is much larger than the impedance of the TENG capacitance. Thus, almost all of the V_{OC} is applied on the load resistance and the TENG is working under a quasi-OC condition. When the load resistance is in the middle region (matches the TENG impedance), the maximum transit power can be reached.

Mathematically, this can be interpreted by considering the two limitation conditions. When R approaches 0, equation 4.2a can be easily simplified to be CV_{OC}, which is just the same equation with Q_{SC}. The TENG is now in the quasi-SC condition (Region I). When R approaches infinity, equation 4.2c can be easily simplified to be V_{OC}, which is just the open-circuit voltage. The TENG is now in the quasi-OC condition, which is the Region III. When R is neither too large nor too small, the behavior of the TENG is in the transitional region between short-circuit and open-circuit conditions (Region II), within which the maximum power is reached.

4.2 Optimum resistance

In this three-working-region behavior of the TENG, the optimum resistance for the maximum instantaneous power is a key parameter to maximize the effective efficiency of the TENG. Therefore, the position of the optimum resistance needs to be systematically studied to find its relationship with the TENG's structural parameters and operational conditions, so that the TENG can be rationally controlled for different application purposes.

From the impedance match process we discussed above, the influence of structural parameters and motion condition on the optimum resistance can be easily addressed. For a TENG, its average impedance is approximately $1/(\omega C_{avg})$, where ω is the angular frequency of the signal source V_{OC} and C_{avg} is the average TENG inherent capacitance. Any structural parameters that can increase C_{avg} will lower the TENG impedance and lower the optimum resistance. Increasing the motion velocity is equivalent to the increase of ω, which will also lower the optimum resistance.

As a typical example, we can analyze the optimum resistance of an attached-electrode contact-mode TENG.[25] The optimum resistance can be mathematically investigated under an arbitrary motion for an attached-electrode TENG model built above. We first decompose an arbitrary smooth moving mode with an average velocity v into a series of polynomial moving-mode, which is shown in the equations below.

$$x = \sum_{n=1}^{\infty} \alpha_n \frac{v^n}{x_{\max}^{n-1}} t^n \quad \left(\mathrm{t} < \frac{x_{\max}}{\mathrm{v}}\right) \quad (4.8a)$$

$$x = x_{\max} \left(\mathrm{t} \geq \frac{x_{\max}}{\mathrm{v}}\right) \quad (4.8b)$$

α_n is the coefficient of n^{th} polynomial moving-mode, and satisfies the following equation.

$$\sum_{n=1}^{\infty} \alpha_n = 1 \qquad (4.8c)$$

If we substitute this equation into the general equation of the current (Equation 4.3b), the current under arbitrary moving mode can be given as:

$$I(t) =$$

$$-\frac{\sigma d_0}{R\varepsilon_0} + \frac{\sigma d_0}{R\varepsilon_0}\left(1 + \sum_{n=1}^{\infty} \frac{\alpha_n v^n}{d_0 x_{max}^{n-1}} t^n\right) \exp\left[-\frac{1}{RS\varepsilon_0}\left(d_0 t + \sum_{n=1}^{\infty} \frac{\alpha_n v^n}{(n+1)x_{max}^{n-1}} t^{n+1}\right)\right] + \frac{\sigma d_0}{R\varepsilon_0} \times$$

$$\frac{d_0}{RS\varepsilon_0}\left(1 + \sum_{n=1}^{\infty} \frac{\alpha_n v^n}{d_0 x_{max}^{n-1}} t^n\right) \exp\left[-\frac{1}{RS\varepsilon_0}\left(d_0 t + \sum_{n=1}^{\infty} \frac{\alpha_n v^n}{(n+1)x_{max}^{n-1}} t^{n+1}\right)\right] \times$$

$$\int_0^t \exp\left[\frac{1}{RS\varepsilon_0}\left(d_0 z + \sum_{n=1}^{\infty} \frac{\alpha_n v^n}{(n+1)x_{max}^{n-1}} z^{n+1}\right)\right] \mathrm{d}z \ \left(t \le \frac{x_{max}}{\mathrm{v}}\right) \quad (4.9)$$

Since the current starts to decay exponentially when t is larger than x_{max}/v (the external motion stops), the peak value of the current can only exist inside the closed interval [0, x_{max}/v]. In order to find the time (t_{max}) of the current peak, we take the differentiation of the $I(t)$ and the time t_0 satisfies the following equation.

$$\left(\frac{\mathrm{d}I}{\mathrm{d}t}\right)_{t=t_0} = 0 \qquad (4.10)$$

Therefore, we can derive that:

$$\sum_{n=1}^{\infty} \frac{n\alpha_n v^n}{x_{max}^{n-1} d_0} {t_0}^{n-1} \times \exp\left[-\frac{d_0^2}{RS\varepsilon_0 v}\left(\frac{vt_0}{d_0} + \sum_{n=1}^{\infty} \frac{\alpha_n v^{n+1}}{(n+1)x_{max}^{n-1} d_0^2} {t_0}^{n+1}\right)\right] + (1$$

$$+ \sum_{n=1}^{\infty} \frac{\alpha_n v^n}{x_{max}^{n-1} d_0} {t_0}^n) \times \exp\left[-\frac{d_0^2}{RS\varepsilon_0 v}\left(\frac{vt_0}{d_0} + \sum_{n=1}^{\infty} \frac{\alpha_n v^{n+1}}{(n+1)x_{max}^{n-1} d_0^2} {t_0}^{n+1}\right)\right]$$

$$\times \left(-\frac{d_0^2}{RS\varepsilon_0 v}\right) \times (\frac{v}{d_0} + \frac{v}{d_0} \sum_{n=1}^{\infty} \frac{\alpha_n v^n}{x_{max}^{n-1} d_0} {t_0}^n) + \frac{d_0^2}{RS\varepsilon_0 v} \sum_{n=1}^{\infty} \frac{n\alpha_n v^{n+1}}{x_{max}^{n-1} d_0^2} {t_0}^{n-1}$$

$$\times \exp\left[-\frac{d_0^2}{RS\varepsilon_0 v}\left(\frac{vt_0}{d_0} + \sum_{n=1}^{\infty} \frac{\alpha_n v^{n+1}}{(n+1)x_{max}^{n-1} d_0^2} {t_0}^{n+1}\right)\right]$$

$$\times \int_0^{t_0} \exp\left[\frac{d_0^2}{RS\varepsilon_0 v}\left(\frac{vz}{d_0} + \sum_{n=1}^{\infty} \frac{\alpha_n v^{n+1}}{(n+1)x_{max}^{n-1} d_0^2} \mathrm{z}^{n+1}\right)\right] dz - \left(\frac{d_0^2}{RS\varepsilon_0 v}\right)^2 (\frac{v}{d_0}$$

$$+ \sum_{n=1}^{\infty} \frac{\alpha_n v^{n+1}}{x_{max}^{n-1} d_0^2} {t_0}^n) \exp\left[-\frac{d_0^2}{RS\varepsilon_0 v}\left(\frac{vt_0}{d_0} + \sum_{n=1}^{\infty} \frac{\alpha_n v^{n+1}}{(n+1)x_{max}^{n-1} d_0^2} {t_0}^{n+1}\right)\right]$$

$$\times (\frac{v}{d_0} + \frac{v}{d_0} \sum_{n=1}^{\infty} \frac{\alpha_n v^n}{x_{max}^{n-1} d_0} {t_0}^n)$$

$$\times \int_0^{t_0} \exp\left[\frac{d_0^2}{RS\varepsilon_0 v}\left(\frac{vz}{d_0} + \sum_{n=1}^{\infty} \frac{\alpha_n v^{n+1}}{(n+1)x_{max}^{n-1} d_0^2} \mathrm{z}^{n+1}\right)\right] dz + \frac{d_0^2}{RS\varepsilon_0 v} (\frac{v}{d_0}$$

$$+ \frac{v}{d_0} \sum_{n=1}^{\infty} \frac{\alpha_n v^n}{x_{max}^{n-1} d_0} {t_0}^n) = 0 \quad (4.11)$$

The parameter *w* inside equation 4.11 was defined as $t_0 v / x_{max}$,

Noting that (The parameter *y* is defined as x_{max}/d_0)

$$\int_0^{t_0} \exp\left[\frac{d_0^2}{RS\varepsilon_0 v}\left(\frac{vz}{d_0}+\sum_{n=1}^{\infty}\frac{\alpha_n v^{n+1}}{(n+1)x_{max}^{n-1}d_0^2}z^{n+1}\right)\right]\mathrm{d}z$$

$$=\int_0^{\mathrm{w}} \exp\left[\frac{d_0^2}{RS\varepsilon_0 v}\left(\frac{x_{max}}{d_0}z+\frac{x_{max}^2}{d_0^2}\sum_{n=1}^{\infty}\frac{\alpha_n z^{n+1}}{n+1}\right)\right]\frac{x_{max}}{v}\mathrm{d}z$$

$$=\frac{x_{max}}{v}\int_0^{\mathrm{w}} \exp\left[F^2\left(yz+y^2\sum_{n=1}^{\infty}\frac{\alpha_n z^{n+1}}{n+1}\right)\right]\mathrm{d}z \quad (4.12)$$

The above equation can be simplified as

$$\frac{1}{F^2}\sum_{n=1}^{\infty} n\alpha_n w^{n-1}\exp[-F^2(yw+y^2\sum_{n=1}^{\infty}\frac{\alpha_n}{n+1}w^{n+1})]$$

$$-\exp[-F^2(yw+y^2\sum_{n=1}^{\infty}\frac{\alpha_n}{n+1}w^{n+1})]\left(1+y\sum_{n=1}^{\infty}\alpha_n w^n\right)^2$$

$$+y\sum_{n=1}^{\infty} n\alpha_n w^{n-1}\exp[-F^2(yw+y^2\sum_{n=1}^{\infty}\frac{\alpha_n}{n+1}w^{n+1})]$$

$$\times\int_0^{w}\exp\left[F^2\left(yz+y^2\sum_{n=1}^{\infty}\frac{\alpha_n z^{n+1}}{n+1}\right)\right]\mathrm{d}z$$

$$-F^2\,y\left(1+y\sum_{n=1}^{\infty}\alpha_n w^n\right)^2\exp[-F^2(yw$$

$$+y^2\sum_{n=1}^{\infty}\frac{\alpha_n}{n+1}w^{n+1})]\int_0^{w}\exp\left[F^2\left(yz+y^2\sum_{n=1}^{\infty}\frac{\alpha_n z^{n+1}}{n+1}\right)\right]\mathrm{d}z+1$$

$$+y\sum_{n=1}^{\infty}\alpha_n w^n=0 \quad (4.13)$$

Therefore, we know that *w* is only a function (*f*) of *F* and *y*

$$w=f(F,\mathrm{y}) \qquad (4.14)$$

Therefore,

$$t_0 = \frac{x_{\max}}{v} w = \frac{x_{\max}}{v} f(F, y) \qquad (4.15)$$

When R is small (R < 100 MΩ in Figure 4-1), the peak value appears between t=0 and t=x_{max}/v and t_{max} is equal to t_0. When R is large enough (R> 1 GΩ in Figure 4-1), t_0 is larger than x_{max}/v, so the current will increase monotonically between t=0 and t=x_{max}/v. Then, t_{max} is equal to x_{max}/v. Thus, in the entire region of R, t_{max} is the minimum value of t_0 and x_{max}/v, which can be given by:

$$t_{\max} = \min\left(t_0, \frac{x_{\max}}{v}\right) \qquad (4.16)$$

Therefore, we have:

$$t_{\max} = \min\left(t_0, \frac{x_{\max}}{v}\right) = \frac{x_{\max}}{v} \min(f(F, y), 1) = \frac{x_{\max}}{v} M(F, y) \qquad (4.17)$$

where M is an another function. Substituting Equation 4.17 into Equation 4.9, [25]

Note that

$$1 + \frac{1}{d_0} \sum_{n=1}^{\infty} \frac{\alpha_n v^n}{x_{max}^{n-1}} t_{max}^n = 1 + y \sum_{n=1}^{\infty} \alpha_n M^n(F, y) \qquad (4.18a)$$

$$-\frac{1}{RS\varepsilon_0}\left(d_0 t_{max} + \sum_{n=1}^{\infty} \frac{\alpha_n v^n}{(n+1)x_{max}^{n-1}} t_{max}^{n+1}\right)$$

$$= -F^2 y M(F, y)\left(1 + y \sum_{n=1}^{\infty} \frac{\alpha_n M^n(F, y)}{n+1}\right) \qquad (4.18b)$$

$$\int_0^{t_{max}} \exp\left[\frac{1}{RS\varepsilon_0}\left(d_0 z + \sum_{n=1}^{\infty} \frac{\alpha_n v^n}{(n+1)x_{max}^{n-1}} z^{n+1}\right)\right] dz$$

$$= \frac{x_{max}}{v} \int_0^{\mathrm{M(F,y)}} \exp\left[F^2 y\left(z + y \sum_{n=1}^{\infty} \frac{\alpha_n z^{n+1}}{n+1}\right)\right] dz \qquad (4.18c)$$

Therefore,

$$I_{\max} = \frac{\sigma d_0}{R\varepsilon_0}\Bigg\{-1 + \left(1 + y\sum_{n=1}^{\infty}\alpha_n M^n(F,y)\right) \times \exp\left[-F^2 y M(F,y)\left(1 + y\sum_{n=1}^{\infty}\frac{\alpha_n M^n(F,y)}{n+1}\right)\right] + F^2 y\left(1 + y\sum_{n=1}^{\infty}\alpha_n M^n(F,y)\right) \times \exp\left[-F^2 y M(F,y)\left(1 + y\sum_{n=1}^{\infty}\frac{\alpha_n M^n(F,y)}{n+1}\right)\right] \times \int_0^{\mathrm{M(F,y)}} \exp\left[F^2 y\left(z + y\sum_{n=1}^{\infty}\frac{\alpha_n z^{n+1}}{n+1}\right)\right]\mathrm{d}z\Bigg\} \quad (4.19)$$

Therefore, the peak value of current $I_{\max}$ can be written as

$$I_{\max} = \frac{\sigma d_0}{R\varepsilon_0} G(F,y) \quad (4.20)$$

The function $G(F,y)$ is given by:

$$G(F,y) = -1 + \left(1 + y\sum_{n=1}^{\infty}\alpha_n M^n(F,y)\right) \times \exp\left[-F^2 y M(F,y)\left(1 + y\sum_{n=1}^{\infty}\frac{\alpha_n M^n(F,y)}{n+1}\right)\right] + F^2 y\left(1 + y\sum_{n=1}^{\infty}\alpha_n M^n(F,y)\right) \times \exp\left[-F^2 y M(F,y)\left(1 + y\sum_{n=1}^{\infty}\frac{\alpha_n M^n(F,y)}{n+1}\right)\right] \times \int_0^{\mathrm{M(F,y)}} \exp\left[F^2 y\left(z + y\sum_{n=1}^{\infty}\frac{\alpha_n z^{n+1}}{n+1}\right)\right]\mathrm{d}z \quad (4.21)$$

Then, the peak instantaneous power is:

$$P_{\max} = I_{\max}^2 R = \frac{(\sigma d_0)^2}{\varepsilon_0^2} \times \frac{1}{R} G^2(F, y) = \frac{\sigma^2 S v}{\varepsilon_0} F^2 G^2(F, y) \quad (4.22)$$

The optimum load resistance R_{opt} satisfies the following equation:

$$\frac{\partial P_{\max}}{\partial \mathrm{R}} = 0 \quad (4.23)$$

Therefore, combining Equation 4.22 and Equation 4.23, the optimum resistance satisfies the following equation:

$$\mathrm{G}\left(F_{\text{opt}}, y\right) + F_{\text{opt}} \left(\frac{\partial \mathrm{G}}{\partial \mathrm{F}}\right)_{F=F_{\text{opt}}} = 0 \quad (4.24)$$

Equation 4.24 shows that the optimum value of F is only a function of y. Therefore,

$$F_{\text{opt}} = H(y) = \frac{d_0}{\sqrt{R_{\text{opt}} S \varepsilon_0 v}} \quad (4.25)$$

where the function H only relies on the moving mode.

Thus, the expression of R_{opt} can be given by:

$$R_{\text{opt}} = \frac{{d_0}^2}{F_{\text{opt}}^2 S v \varepsilon_0} = \frac{{d_0}^2}{[H(y)]^2 S v \varepsilon_0} = \frac{{d_0}^2}{[H\left(\frac{x_{\max}}{d_0}\right)]^2 S v \varepsilon_0} \quad (4.26)$$

This equation can be easily understood from the fundamental impedance match process. An increase in the area size of the TENG will increase the TENG capacitance than will lower its impedance. The optimum resistance reduces as a response. Similarly, increasing average velocity is equivalent to increase the high frequency component of V_{OC}, which will reduce the TENG impedance as well. As a result, the optimum resistance will decrease. If the effective dielectric thickness increases, the inherent TENG capacitance will reduce and its impedance will increase, so the optimum resistance increases. In addition, increasing the gap will reduce the average capacitance and increase the average impedance, so the optimum resistance also increases. From the similar

analysis, since the TENG impedance is independent of the tribo-charge density, the optimum resistance will not be affected if the tribo-charge density changes.

These conclusions of optimum resistance can also be validated through numerical calculation and experimental studies.[25] As shown in Figure 4-2a, R_{opt} is inversely proportional to either the area size (S) or the average velocity (v). On the other hand, the influences of effective dielectric thickness and air gap distance on R_{opt} are displayed in Figure 4-2b. If we keep the ratio (y) of the above two thicknesses (d_0 and x_{max}) as constant of 27.2, R_{opt} is proportional to d_0^2. Two set of experiments were also performed to validate the theoretical results. In the first set of experiments, the same device was measured under different average velocities, as shown in Figure 4-2c. When the average velocities are 0.02 m/s, 0.04 m/s, and 0.08 m/s, the derived optimum load resistance (through interpolation of the experiment data) is 14.2 MΩ, 6.66 MΩ, and 4.08 MΩ, respectively, which shows the same trend with the theoretical estimation. In the other set of measurements, the influence of the gap and the dielectric thickness is experimentally studied, as shown in Figure 4-2d. The thickness of the Kapton film (d_k) in device 1 is 25 μm while that of device 2 is 125 μm, and the corresponding gaps (x_{max}) are 2 mm and 10 mm, respectively, which maintains the same y. Through the measurement on a series of resistors with all the other parameters kept the same, the obtained optimum resistance for device 1 is 7.69 MΩ while that of device 2 is 162.3 MΩ. The experimental optimum resistance ratio is 21.1, which is quite close to 25, as the theoretical estimation value.

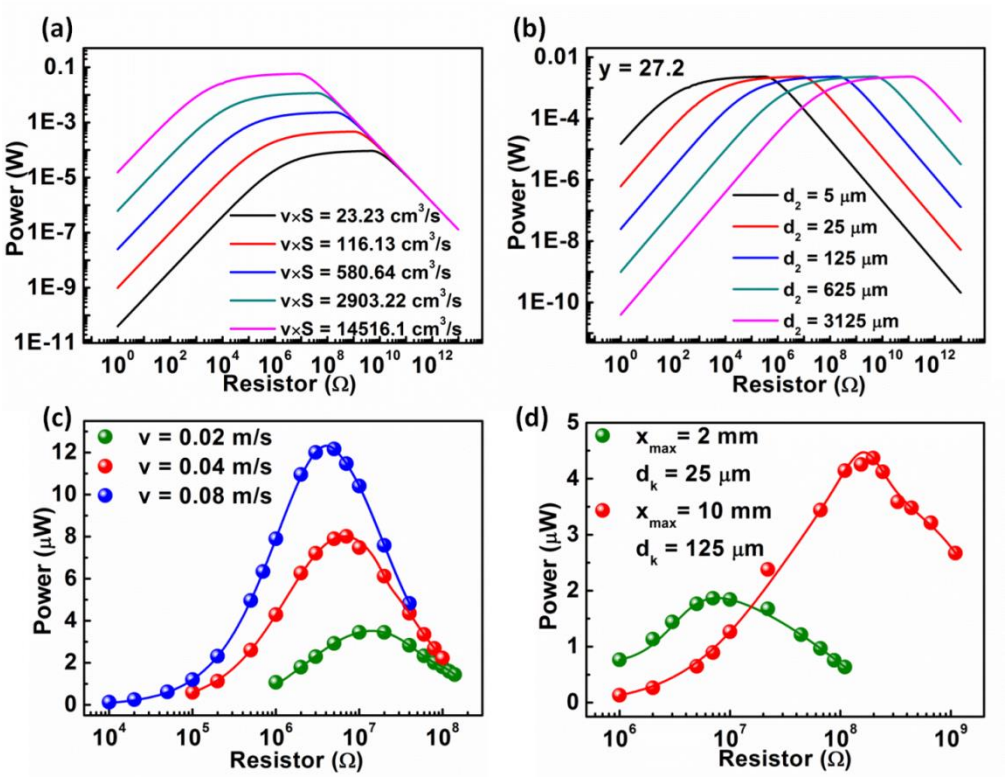

Figure 4-2. Numerical and experimental verification of optimum resistance. (a-b) The relationship of optimum resistance with different TENG parameters under uniform velocity motion. (a) Maximum output power profile with load resistance and at different velocities or area sizes. (b) Maximum output power profile with load resistance under different effective dielectric thickness and gap distances with maintaining their ratio as a constant of 27.2. (c-d) Experimental comparison of the optimum resistances from TENG devices with different parameters. The dots are measured values and the lines are obtained through interpolation of the experimental data. (c) Maximum output power profile with load resistance at different average velocities. (d) Maximum output power profile with load resistance at different Kapton film thickness and gap distances with their ratio (y) remaining as constant. Reproduced from reference [25]. Copyright 2013 Royal Society of Chemistry.

CHAPTER 5

TRIBOELECTRIC NANOGENERATOR CAPACITIVE LOAD CHARACTERISTICS AND CHARGING BEHAVIORS

In the above chapter the resistive load characteristics of TENG are discussed. In this chapter, we will discuss another important load condition: capacitive load. [34]We will start from the simplest unidirectional motion charging characteristics. Then a much more complicated multiple-cycle charging process was analyzed to show the unique TENG charging characteristics and an optimum load capacitance was observed for maximized energy storage. To obtain the optimized design strategy for such system, the analytical solution of the optimum load capacitance was deducted and its dependence on the charging cycle numbers and TENG structural parameters was shown.

5.1 Triboelectric nanogenerator charging characteristics under unidirectional mechanical motion

We start our discussion with the simplest case, which is utilizing a single-electrode contact-mode TENG to charge a load capacitor (C_L) under a unidirectional mechanical motion. In this process, no external rectifier is needed because the charging current of the TENG is also unidirectional. Besides, the inherent capacitance (C_T) of a single-electrode TENG is nearly constant, which will also simplify our discussion. The model of the single-electrode contact-mode TENG is the same as we described above in Chapter 2. Utilizing the above equivalent circuit model of TENG, the equivalent circuit

model of this whole system is shown as Figure 5-1a. In the discussion, Q was defined as the transferred charges from the primary electrode to the reference electrode and Q^C was defined as the charges on the top plate of the load capacitor.

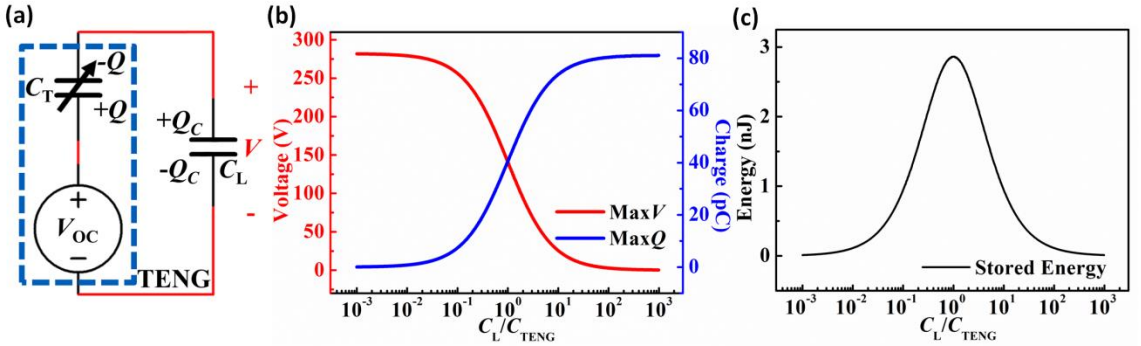

Figure 5-1. (a) Equivalent circuit model of TENG-capacitor system of the unidirectional charging calculation. (b) The influence of the load capacitance on the final voltage and charge stored in the load capacitor. (c) Final stored energy profile with load capacitance. Reproduced from Reference [34]. Copyright 2015 IEEE.

To solve the above equivalent circuit, the initial condition must be specified. As a typical example, we consider the case that at $t = 0$, the top dielectric has stopped at $x = 0$ position for a long time and just starts moving. Besides, no initial charges are stored on the load capacitor, so initial charges on both C_T and C_L are 0 ($Q(t = 0) = Q^C(t = 0) = 0$). Thus, the following equations can be obtained from Kirchhoff's Law and node charge conservation, where V stands for the voltage across C_L and V_{OC} stands for the open circuit voltage of the TENG.

$$V = -\frac{1}{C_T}Q + V_{OC} = \frac{1}{C_L}Q^C \quad (5.1)$$

$$Q^C - Q = Q^C(t = 0) - Q(t = 0) = 0 \quad (5.2)$$

In practical application, the motion of the dielectric always has a maximum separation distance, which is defined as x_{max}. Thus, the final voltage and charge on the

capacitor when a full separation is reached (x reaches x_{max}) can be obtained by solving the above two equations. ($V_{OC,max}$ and $Q_{SC,max}$ stands for the open circuit (OC) voltage and short circuit (SC) transferred charge of the TENG when $x = x_{max}$)

$$V(x = x_{\max}) = \frac{C_T V_{\mathrm{OC,max}}}{C_L + C_T} = \frac{Q_{\mathrm{SC,max}}}{C_L + C_T} \qquad (5.3)$$

$$Q_{\mathrm{C}}(x = x_{\max}) = \frac{C_L Q_{\mathrm{SC,max}}}{C_L + C_T} \qquad (5.4)$$

Thus, the total energy stored in the capacitor (E^{C}) can be given by:

$$E_{\mathrm{C}} = \frac{1}{2} C_L [V(x = x_{max})]^2 = \frac{C_L [Q_{\mathrm{SC}}(x = x_{max})]^2}{2(C_L + C_T)^2} \qquad (5.5)$$

To obtain an intuitive sense of such equations, numerical calculation for the single-electrode TENG under constant velocity motion condition is performed and output profiles as a function of time with different load capacitances are shown in Figure 5-1. (The detailed calculation parameters are listed in Table 5.1). When C_{L} is small, its impedance is much larger than the impedance of C_{T}. Thus, almost all of the V_{OC} is applied on C_{L} and the TENG is working under a quasi-OC condition. Therefore, the voltage charging curves for small C_{L} are all close to the V_{OC} curve. However, the stored charge is still close to 0 because of the small C_{L}, leading to a limited final stored energy. On the opposite, when C_{L} is very large, its impedance is much smaller than the impedance of C_{T}, so the voltage applied on C_{L} is approximately 0. At this moment, the TENG is working under a quasi-SC condition and the stored-charge curves for large C_{L} are all close to the Q_{SC} curve. However, the total stored energy is still limited because of the low voltage across C_{L}. From the above analysis, only at the transition region the stored energy can reach its maximum. Mathematically, it can be easily derived from 6.39 that the optimum load capacitance ($C_{\mathrm{L,opt}}$) at which the maximum stored energy is

reached is equal to C_T, as shown in Figure 5-1c. Physically, this means the impedance match between the TENG and the load is reached.

Table 5.1. Parameters utilized in the calculation of the unidirectional charging behaviors for a single-electrode TENG

Structure Component	Parameters utilized
Relative dielectric constant ε_r	2
Thickness of the dielectric d_r	100 μm
Width of the structure w	5 mm
Length of dielectrics l	5 mm
Gap distance between the electrodes g	1 mm
Tribo-charge surface density σ	8 μCm^{-2}
Maximum separation distance x_{max}	0.02 m
Average velocity v	1 ms^{-1}

5.2 Triboelectric nanogenerator charging performance under periodic mechanical motion

Above we analyzed the charging behavior of a single-electrode TENG to charge a load capacitor under a unidirectional motion. However, in practical applications, the mechanical motion is almost never unidirectional, resulting in an AC charging current. Therefore, a full-bridge diode rectifier is necessary to prevent the charge leaking back from C_L to the TENG. Besides, the inherent capacitance of most TENGs is time-variant.[35] Therefore, the real case is much more complicated than the above discussion. As a typical example, the case we analyzed in the following section is a contact-mode attached-electrode TENG under a periodic harmonic motion process (shown in 5.6). [25]

$$x = x_{max}\left[\frac{1}{2} - \frac{1}{2}\cos\left(\frac{\pi v}{x_{max}}t\right)\right] \qquad (5.6)$$

The structure of this TENG is shown in Figure 5-2a and the working principle has been discussed in detail in Chapter 3.1. Utilizing the parameters listed in Table 5.2, we can obtain the numerical results of this non-linear time-variant system shown in Figure 5-2b from the TENG-simulator. [27] The simulation results are plotted in Figure 5-3. As shown in Figure 5-3a, a saturation charging curve is observed for all the load capacitors, which is very similar to a typical RC charging curve in shape. At $t = 0$, the load capacitor is charging at a maximum speed. Then the charging speed gradually slows down and finally the same saturation voltage about 104.8 V is reached for all the different load capacitors. It takes less time to charge a smaller C_L to reach its saturation voltage. However, a different trend is observed for the stored charges. At beginning, the curves for all load capacitors converge to one linear curve, with the charging rate of $2Q_{SC,max}$ per cycle. However, when time increases, the curves from small C_L shift downwards first and finally get saturated. At this moment, very few charges can be pumped into the capacitor. The voltage and the stored charge of the load capacitor after 1000 charging cycles are shown in Figure 5-3c, which have the similar trend as the previous shown unidirectional charging case. When C_L is small enough, the voltage on the load capacitor is approximately its saturation voltage while the stored charges are close to 0 and proportional to C_L. When C_L is large enough, the stored charges are approximately $2kQ_{SC,max}$ while the voltage is close to 0 and inversely proportional to C_L. Similar to the previous unidirectional charging, an optimum capacitance for maximum stored energy is also observed in the transition region of C_L.

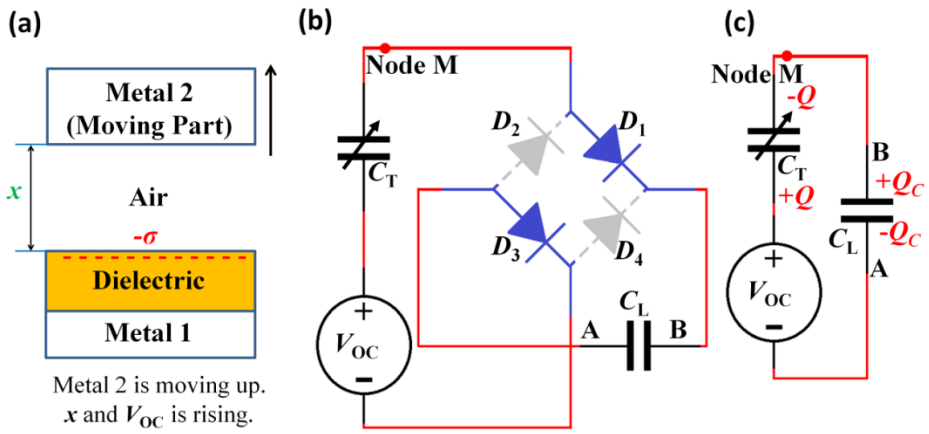

Figure 5-2. Equivalent circuit diagram for TENG charging performance calculation under periodic mechanical motion. (a) Structure of the contact-mode attached-electrode TENG used in the calculation. (b) Circuit diagram showing the conduction condition of full-bridge rectifier in the first half cycle. (c) Simplified circuit diagram under ideal diode approximation in the first half cycle. Reproduced from Reference [34]. Copyright 2015 IEEE.

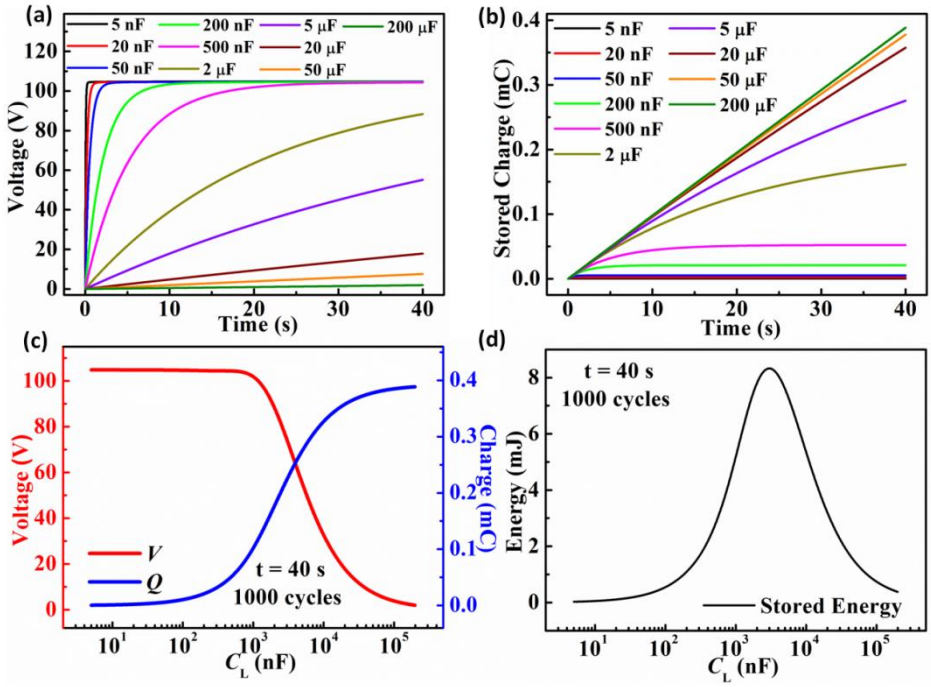

Figure 5-3. TENG charging characteristics under periodic mechanical motion. (a) Voltage-time relationship at different load capacitances. (b) Stored charge-time relationship at different load capacitances. (c) The influence of the load capacitance on the final voltage and charge stored in the load capacitor. (d) Final stored energy profile with load capacitance. Reproduced from Reference [34]. Copyright 2015 IEEE.

Table 5.2. Parameters utilized in the calculation of the multiple-cycle charging behaviors for a contact-mode attached-electrode TENG.

Structure Component	Parameters utilized
Relative dielectric constant ε_r	2.1
Thickness of the dielectric d_r	50 μm
Area of the dielectric S	0.005 m^2
Tribo-charge surface density σ	40 μCm^{-2}
Maximum separation distance x_{max}	0.002 m
Average Velocity v	0.1 ms^{-1}

In addition to the demonstrated numerical calculation, an analytical solution is preferred to better understand the underline physics despite the fact that only approximate solution can be derived. To address this non-linear time-variant system, linearizing the diodes of the bridge rectifier is a critical step. As shown in Figure 5-2a-b, in the first half of each cycle, the top plate is moving upward and V_{oc} is increasing. Neglecting the reverse leakage current of the diode, we can assume only diode 1 and 3 are conducting in this step and diode 2 and 4 are fully open-circuit. Besides, the conducting voltage of these two diodes can be neglected, for it is much smaller than the open-circuit voltage of the TENG. With the above assumptions, the complex circuit shown in Figure 5-2b can be simplified to the linear circuit shown in Figure 5-2c, which is similar to the unidirectional circuit shown in Figure 5-1a. Similarly, in the second half of each cycle when V_{oc} is decreasing, the circuit can also be simplified, but the direction of C_L is reversed because of the function of the full-bridge rectifier.

The initial condition we utilized is still the same with the analysis of unidirectional charging, that is the initial charges on both C_T and C_L are 0. So at the beginning of the first cycle, the total charges stored on Node M (shown in Figure 5-2b

and c) are 0, which is shown in mathematics as $Q^{M}_{1}= 0$. (Q^{M}_{k} stands for the total charges on the Node M at the beginning of the *k*th cycle).

Now we consider the *k*th charging cycle. During its first half, it is a unidirectional charging step. Similar to the previous derivation, at the end of this half cycle ($x = x_{max}$), the charges stored on C_T (Q) and C_L (Q^C) can be given by:

$$Q_{k,1\text{end}} = \frac{C_L Q_{\text{SC,max}} - C_{\min} Q^{M}_{k}}{C_L + C_{\min}} \quad (5.7)$$

$$Q^{C}_{\text{k,1end}} = C_L \frac{Q_{\text{SC,max}} + Q^{M}_{k}}{C_L + C_{\min}} \quad (5.8)$$

where the subscript in $Q_{\text{k,1end}}$ stands for its value at the end of the 1st half in the *k*th charging cycle and C_{min} stands for the value of $C_T(x = x_{max})$.

From the end of the first half cycle to the beginning of the second half cycle, the direction of C_L is reversed due to the function of the full bridge rectifier. Thus, the charges stored on Node M at the beginning of the second half of the *k*th cycle ($Q^{M}_{k,\text{mid}}$) can be given by:

$$Q^{M}_{k,\text{mid}} = -Q_{k,2\text{begin}} + Q^{C}_{k,2\text{begin}} = -Q_{k,1\text{end}} - Q^{C}_{k,1\text{end}} \quad (5.9)$$

The second half cycle is also a unidirectional charging step (x is from x_{max} back to 0). Similar to the previous derivation, at the end of this half cycle ($x = 0$), the charges stored on C_T (Q) and C_L (Q^C) can be obtained as (C_{max} stands for the value of $C_T(x = 0)$)

$$Q_{k,2\text{end}} = -\frac{C_{\max} Q^{M}_{k,\text{mid}}}{C_L + C_{\max}} \quad (5.10) \qquad Q^{C}_{k,2\text{end}} = \frac{C_L Q^{M}_{k,\text{mid}}}{C_L + C_{\max}} \quad (5.11)$$

At the end of this second half-cycle, the direction of C_L is reversed again. Thus, the charges stored on Node M at the beginning of the (k+1)th cycle (Q^{M}_{k+1}) can be given by:

$$Q^{M}{}_{k+1} = -Q_{k+1,1\text{begin}} + Q^{C}{}_{k+1,1\text{begin}} = -Q_{k,2\text{end}} - Q^{C}{}_{k,2\text{end}} \qquad (5.12)$$

Through the above equations, a recursion relationship for $Q^{M}{}_{k}$ can be derived below.

$$Q^{M}{}_{k+1} = \frac{C_L - C_{\max}}{C_L + C_{\max}} \frac{C_L - C_{\min}}{C_L + C_{\min}} Q^{M}{}_{k} + 2\frac{C_L - C_{\max}}{C_L + C_{\max}} \frac{C_L}{C_L + C_{\min}} Q_{SC,max} \quad (5.13)$$

With the boundary condition of $Q^{M}{}_{1} = 0$, the above recursion relationship can be easily solved as:

$$Q^{M}{}_{k} = \frac{C_L - C_{\max}}{C_{\min} + C_{\max}} Q_{SC,max} - \frac{C_L - C_{\max}}{C_{\min} + C_{\max}} Q_{SC,max} \left[\frac{(C_L - C_{\max})(C_L - C_{\min})}{(C_L + C_{\max})(C_L + C_{\min})}\right]^{k-1} \quad (5.14)$$

Therefore, the voltage on C_L at the end of kth charging cycle ($|V^{C}{}_{k,2\text{end}}|$) can be easily derived as:

$$\left|V^{C}{}_{k,2\text{end}}\right| = \frac{Q_{SC,max}}{C_{\min} + C_{\max}} \left\{1 - \left[1 - \frac{2(C_{\min} + C_{\max})C_L}{(C_L + C_{\max})(C_L + C_{\min})}\right]^{k}\right\} \quad (5.15)$$

It is useful to note that the above derivation is also applicable to other categories of TENGs because we didn't utilize any TENG category information in our derivation. In practical applications, C_L is usually much larger than both C_{max} and C_{min}. Under this condition, equation 5.15 can be further simplified to (where f stands for the frequency of the periodic motion):

$$\left|V^{C}{}_{k,2\text{end}}\right| = \frac{Q_{\text{SC,max}}}{C_{\min} + C_{\max}} \left\{1 - \exp\left[-\frac{2(C_{\min} + C_{\max})k}{C_L}\right]\right\}$$

$$= \frac{Q_{\text{SC,max}}}{C_{\min} + C_{\max}} \left\{1 - \exp\left[-\frac{2(C_{\min} + C_{\max})ft}{C_L}\right]\right\} \qquad (5.16)$$

Equation 5.16 clearly shows that a TENG together with a bridge rectifier under periodic external motion is completely comparable to a DC voltage source in series with a resistor regarding the capacitor charging characteristics. They all follow the same exponential saturation trend. The value of the DC source is the saturation voltage (V_{sat}) shown in Figure 5-3a and its value can be easily calculated as:

$$V_{\mathrm{sat}} = \lim_{k\to\infty} \left| V^{C}{}_{k,2\mathrm{end}} \right| = \frac{Q_{\mathrm{SC,max}}}{C_{\mathrm{min}} + C_{\mathrm{max}}} \qquad (5.17)$$

Same as a first order RC charging circuit, V_{sat} is only a function of TENG parameters but is independent of C_L, which is consistent with the above numerical results shown in Figure 5-3a. Utilizing the parameters shown in Table 5.2, we can calculate that the saturation voltage for the previous TENG system is 105.06V, which is very close to the simulation results (104.8V).

Besides the saturation voltage, the charging speed is another important charging parameter. Analogous to a first-order RC charging circuit, time constant (τ) is utilized to characterize the charging speed, which can be easily given by:

$$\tau = \frac{C_L}{2(C_{\mathrm{min}} + C_{\mathrm{max}})f} \qquad (5.18)$$

The time constant is directly proportional to C_L. Therefore, the value of the effective resistor in the first-order RC charging circuit can be easily extracted as $1/[2f(C_{max}+C_{min})]$, which shows that the TENG with a larger inherent capacitance can charge C_L with a higher speed.

Moreover, when C_L is large enough, linear charging behavior is observed and the TENG is working on quasi-SC condition. When C_L is close to infinity, the final stored charges at the end of the *k*th charging cycle can be given by:

$$\lim_{C_{\mathrm{L}}\to\infty}\left|{V^{C}}_{k,2\mathrm{end}}\right| = \lim_{C_{\mathrm{L}}\to\infty}\frac{2kQ_{\mathrm{SC,max}}}{C_L} = 0 \qquad (5.19)$$

$$\lim_{C_{\mathrm{L}}\to\infty}\left|{Q^{C}}_{k,2\mathrm{end}}\right| = C_L\lim_{C_{\mathrm{L}}\to\infty}\left|{V^{C}}_{k,2\mathrm{end}}\right| = 2kQ_{\mathrm{SC,max}} \qquad (5.20)$$

Since the maximum charge generated from the TENG is $Q_{\mathrm{SC,max}}$ for each half cycle, the above results show that all the charges generated from the TENG are stored in C_{L}. At the same time, the voltage difference across the TENG is 0, which is completely consistent with the numerical results shown in Figure 5-3b.

Finally and most importantly, there also exists an optimum load capacitance ($C_{\mathrm{L,opt}}$) at which the stored energy reaches its maximum value. This optimum load capacitance is critically important for optimized design for such energy harvesting system and needs to be analytically derived to show its dependence on the TENG structural parameters and cycle numbers.

From equation 5.16, the energy stored in the load capacitor at the end of the *k*th charging cycle (${E^{\mathrm{C}}}_{k,\mathrm{end}}$) is given by:

$${E^{C}}_{k,\mathrm{end}} = \frac{C_L{V^{C}}_{k,2\mathrm{end}}^{\,2}}{2} = \frac{C_L{Q_{\mathrm{SC,max}}}^{2}}{2(C_{\mathrm{min}}+C_{\mathrm{max}})^2}\left\{1-\exp\left[-\frac{2(C_{\mathrm{min}}+C_{\mathrm{max}})k}{C_L}\right]\right\}^2 \qquad (5.21)$$

At the optimum capacitance, ${E^{\mathrm{C}}}_{k,\mathrm{end}}$ reaches its maximum value. Therefore,

$$\left(\frac{\mathrm{d}{E^{C}}_{k,\mathrm{end}}}{\mathrm{d}C_L}\right)_{C_L=C_{\mathrm{L,opt}}} = 0 \qquad (5.22)$$

Thus, an analytical solution for $C_{\mathrm{L,opt}}$ can be obtained as:

$$C_{\mathrm{L,opt}} = 1.592k(C_{\mathrm{min}}+C_{\mathrm{max}}) \qquad (5.23)$$

Equation 5.23 is an excellent approximation of $C_{\mathrm{L,opt}}$ only when *k* is larger than 10 because the approximation that C_{L} is much larger than both C_{max} and C_{min} is utilized

during the derivation of 5.16. However, the charging cycle number in almost all cases is more than 10, so Equation 5.23 is always a good estimation in practical applications.

The derived $C_{L,opt}$ is linearly proportional to the charging cycle numbers, which is undesirable for practical applications. However, if we put the optimum load capacitance value back to equation 5.16. We found that, at this optimum load capacitance, their charging voltage is always the same value show below.

$$V_{opt} = V_{sat}[1 - \exp(-2/1.592)] = 0.7153V_{sat} \quad (5.24)$$

This optimum charging voltage only depends on TENG properties, but is independent of the time and the load capacitance, which is very important theoretical basis to utilize in the design of the optimum TENG charging cycles.

To verify the above theoretical anticipations, numerical calculations are carried out with contact-mode attached-electrode TENGs with different parameters and cycle numbers, as shown in Figure 5-4. Without special notation in the figure, the values utilized for the parameters are exactly the same as those in Table 5.2. First, the influence of the charging cycle number on $C_{L,opt}$ is investigated. As shown in Figure 5-4a and 5-4b, when the number of charging cycles increases, $C_{L,opt}$ and the maximum energy stored both increases and an accurately linear trend between $C_{L,opt}$ and the charging cycle numbers is observed. In addition, the influence of several structural parameters on $C_{L,opt}$ is investigated as well. For practical contact-mode TENGs with acceptable charge generation efficiency (x_{max} should be much larger than d_0) shown in Figure 5-2a [25], Equation 5.23 can be further simplified utilizing the parallel plate capacitance model.

$$C_{L,opt} = 1.592k\left(\frac{\varepsilon_0 S}{d_0 + x_{max}} + \frac{\varepsilon_0 S}{d_0}\right) \approx \frac{1.592k\varepsilon_0 S}{d_0} \quad (5.25)$$

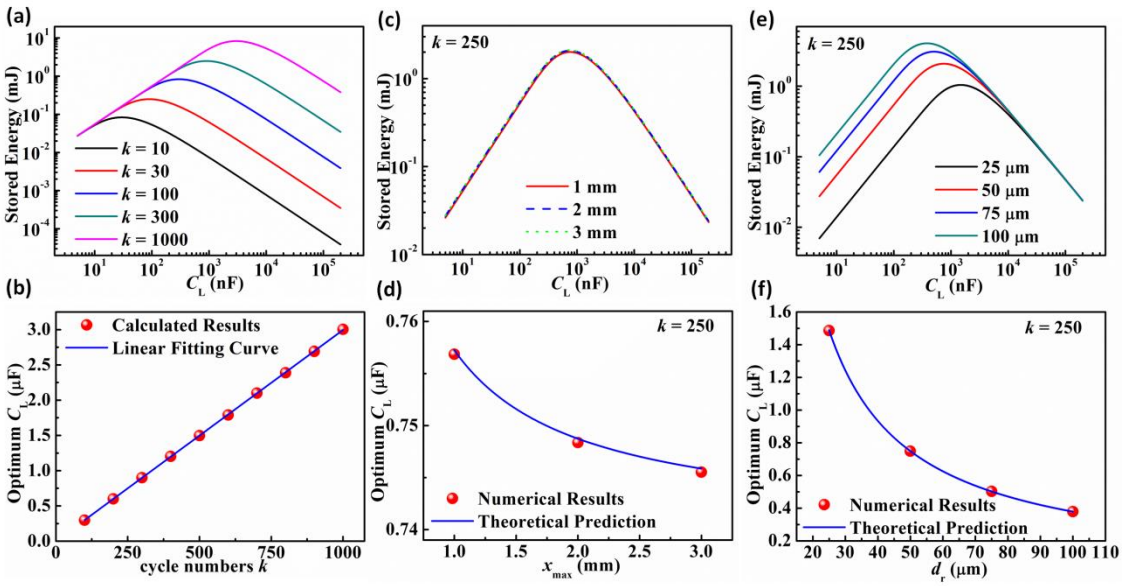

Figure 5-4. Optimum load capacitance characteristics. (a) The relationship between stored energy and load capacitance at different cycle numbers. (b) Extracted optimum capacitance with cycle numbers. (c) The relationship between stored energy and load capacitance at different x_{max}. (d) Extracted optimum capacitance with x_{max}. (e) The relationship between stored energy and load capacitance at different d_r. (f) Extracted optimum capacitance with d_r. Reproduced from Reference [34]. Copyright 2015 IEEE.

First, we investigate the influence of x_{max}. Intuitively, increasing this maximum moving distance will increase the open-circuit voltage of the TENG [25] and may have an obvious influence on V_{sat} and $C_{L,opt}$. However, from Equation 5.16, V_{sat} and $C_{L,opt}$ are mainly affected by the sum of C_{min} and C_{max}, in which C_{min} is negligible compared to C_{max} for a contact-mode attached-electrode TENG. [25] Thus, since x_{max} can only affect C_{min}, the whole charging behavior and $C_{L,opt}$ is almost independent of x_{max}. As shown in Figure 5-4c, the total stored energy as a function of C_L for different x_{max} almost coincide with each other. When x_{max} increases from 1 mm to 3 mm, $C_{L,opt}$ only decreases from 756.9 nF to 745.5 nF, which is completely consistent with the theoretical estimation from 5.25. In contrast with x_{max}, since the dielectric thickness (d_r) will have significant impact on C_{max}, the total charging behavior and $C_{L,opt}$ is obviously dependent on d_r. As shown in

Figure 5-4e and f, when d_r increases from 25 μm to 100 μm, the maximum stored energy increases from 1.04 mJ to 4.05 mJ and $C_{L,opt}$ decreases from 1486 nF to 379 nF, which is completely consistent with the theoretical inverse ratio relationship.

To further validate the theoretical equation presented above, experiments were carried out to compare with the theoretical expectations. A contact-mode attached-electrode TENG with the structure shown in Figure 5-2a was utilized in this experiment. The triboelectric pair material in the TENG was Al and FEP. Al was utilized as one electrode and at the backside of the FEP, copper was deposited as another electrode. The whole structure was supported by two Acrylic sheets. The bottom plate was bonded onto the measurement desk and the top plate was driven by a motor with a 2 Hz harmonic motion. Through bridge rectifier made from four low-leakage and high-breakdown diodes, different low-leakage capacitors were charged by this TENG and a voltage-meter (Keithley Model 6514) was utilized to measure the real-time voltage across the load capacitor. The measured charging curves for different capacitors are shown in Figure 5-5a and b, which have the same shape and trend as the theoretical prediction shown in Figure 5-3. The relationship between the stored energy and the load capacitance is also plotted and an optimum capacitance for the maximized stored energy is also observed as the theoretical prediction. If the interpolated optimum capacitance was extracted and plotted with the cycle number, a very good linear relationship is observed, which is consistent with our theoretical prediction. All of the above experimental results further validate the conclusions from our theoretical derivation, clearly showing its potential to guide future experimental designs.

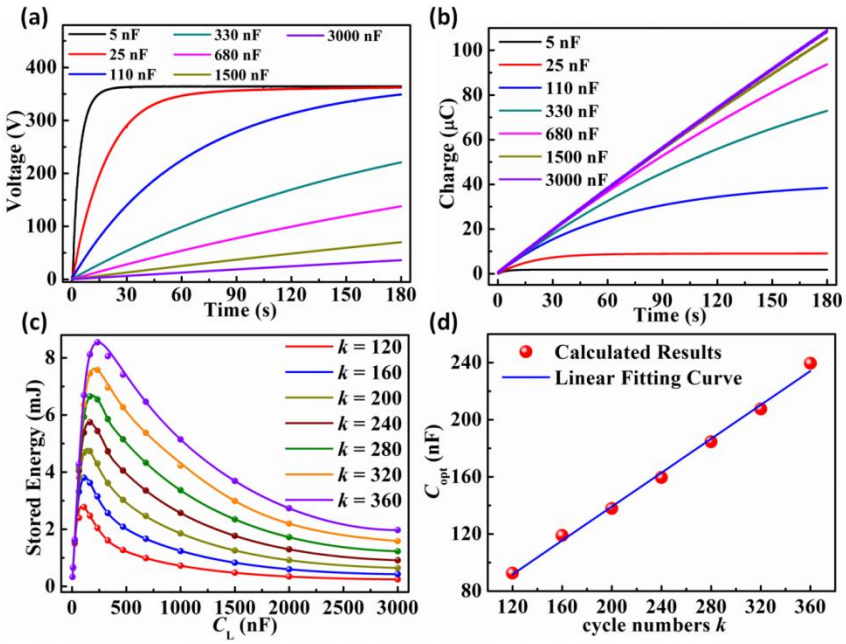

Figure 5-5. Experimental measured multi-step charging profiles. (a) Measured Voltage-time relationship at different load capacitances. (b) Measured stored charge-time relationship at different load capacitances. (c) Measured stored energy-load capacitance relationship at different time. (d) Extracted optimum capacitance with time. Reproduced from Reference [34]. Copyright 2015 IEEE.

CHAPTER 6

STRUCTURE INFLUENCE AND OPTIMIZATION FOR IMPROVED TRIBOELECTRIC NANOGENERATOR OUTPUT PERFORMANCE

In the above chapters, the intrinsic output characteristics and basic load effects of triboelectric generators have been shown. In this chapter, we will discuss some in-depth output characteristics for different modes of triboelectric generators and the influence of several important structural parameters on the output performance. Based on this discussion, some optimization strategies are proposed to obtain an improved TENG output performance.

6.1 Attached-electrode grating-structured TENGs and influence of edge effect

Grating structure is an advanced structural design based on the above discussed sliding-mode TENGs.[15,32,33] Utilizing grating structure, the in-plane charge separation cycles can by multiplied. However, the output characteristics of grating structure are very complicated mainly because the edge effect can no longer be neglected. The length of one grating unit is usually comparable to the dielectric thickness when the grating is fine. In this section, in-depth theoretical models of two types of grating TENGs, one with equal length plates and the other with unequal length plates, are discussed in detail. [36] Through theoretical and computational methods, their output characteristics are obtained and analyzed. With this basic understanding of the output performance, the effect of finer

pitches is outlined for both grating structures. In addition, structural optimization strategies are provided to maximize the power output.

6.1.1 Grating structure with equal-length plates

6.1.1.1 Influence of electrode structure

The grating structure with two equal-length plates is first considered. In a grating TENG, the patterning of the triboelectric layer is essential in order to enable multiple charge separation cycles. On the other hand, patterning is not necessary for the attached electrodes. As shown in Figure 6-1a, there are two choices available: a continuous plate electrode and a grating electrode, in which the electrodes are fabricated with the same grating as the dielectric layer. In this case, the electrical connection is realized through external circuits or electrode bars. These two electrode configurations will lead to different output performance.

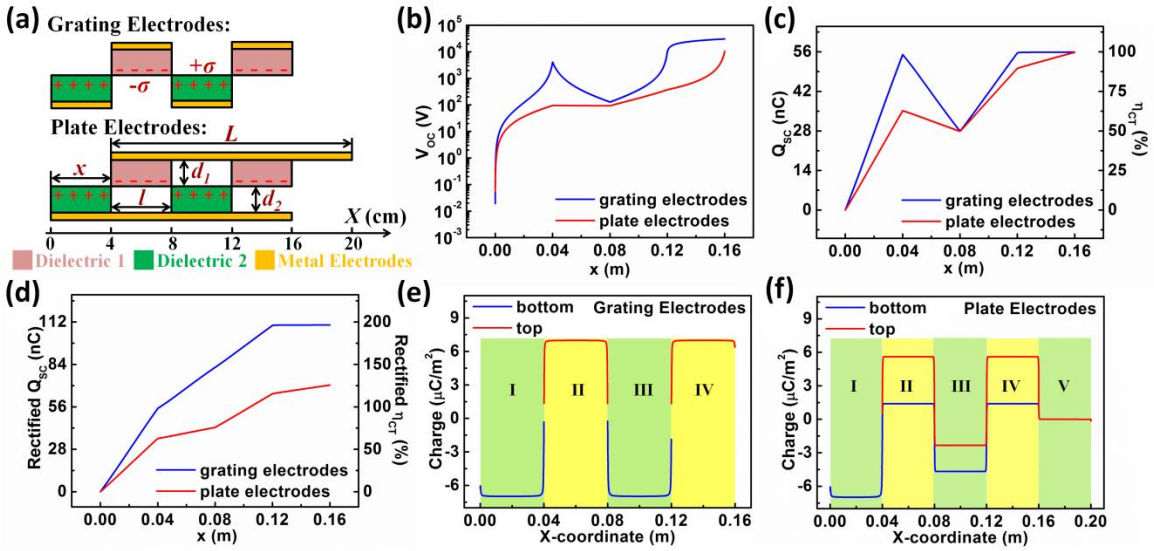

Figure 6-1. Electrode structure optimization of equal-length grating TENGs. (a) Structure of the FEM model for grating TENGs with grating electrodes and plate electrodes. (b-d) Calculated (b) open circuit voltage, (c) transferred charges at short circuit condition, and (d) rectified transferred charges at short circuit condition for grating TENGs with both grating electrodes and plate electrodes. (e-f) charge distribution at the metal electrodes for (e) grating electrodes and (f) plate electrodes at the case $x = l$. Reproduced from reference [36]. Copyright 2014 Royal Society of Chemistry.

To compare the output characteristics of the two grating structures with different electrode configurations, their finite element method (FEM) models were built and calculated using COMSOL. Since the width of grating TENGs is usually much larger than their thickness, 2D models were utilized to simplify the calculation. Two grating dielectrics with 50% duty cycle are placed as tribo-pairs (a pair of materials which will undergo contact electrification). Their half pitch is defined as l and the number of grating units in the top plate is defined as n. The total length of the top plate is L, such that $L = 2nl$. As an example, the case with two grating units ($n = 2$) was studied to illustrate the difference. (Detailed calculation parameters are listed in Table 6.1.) Due to contact electrification, different signs of static charges (called tribo-charges) are distributed at the lower surface of Dielectric 1 and the upper surface of Dielectric 2. We assume that the tribo-charges are uniformly distributed on these surfaces with a density of σ. In order to simulate the relative-sliding motion in operation, the bottom dielectric is fixed and the top dielectric slides in the lateral direction, with the lateral displacement defined as x.

Table 6.1. Parameters utilized in FEM calculations for comparing grating and plate electrodes

Structure Component	Parameter Utilized
Dielectric 1	$\varepsilon_{r1} = 4$, $d_1 = 220$ μm
Dielectric 2	$\varepsilon_{r2} = 2$, $d_2 = 220$ μm
Width of Dielectrics, w	0.1 m
Total Length of the top plate, L	0.16 m
Tribo-charge surface density, σ	7 μCm^{-2}
Velocity, v	1 ms^{-1}

The profiles of V_{OC} and Q_{SC} generated by these two TENGs (Under MACRS) with different electrode structures are completely different, as shown in Figure 6-1b-d.

V_{OC}, Q_{SC}, and the charge transfer efficiency η_{CT} of both structures show an oscillating trend, but those of the plate electrodes are always smaller than those of the grating electrodes. If the AC output is rectified to DC signal for storage, the TENG with grating electrodes would contribute a higher amount of accumulated charge. $\eta_{CT\text{-rectified}}$ after a full displacement cycle from the grating electrode structure can reach 200% while that from the plate electrode only reaches 126%. It should be noted that the reason that $\eta_{CT\text{-rectified}}$ is larger than 100% for both structures comes from the multiple cycles of charge separation, which is the key advantage of the grating structure. As for the open circuit voltage, V_{OC} after a full displacement cycle from the grating electrode can reach around 31 kV while that from the plate electrode only reaches around 10 kV. This set of comparisons clearly shows that the grating electrode is more effective in electricity generation than the plate electrode.

This difference in output characteristics results from the difference in charge distribution at the metal electrodes in these two electrode structures, as shown in Figure 6-1e and f for the example case of $x = l$ under SC conditions. Q_{sc} equals half of the difference between the total amount of charge on top electrodes and on the bottom electrodes, which can be regarded as the sum of the contributions in all sub-regions (as marked in Figure 6-1e and f). As an example, we can analyse the charge distribution in Region II and its contribution to Q_{sc} to elucidate the difference between these two electrode structures.

For the grating electrode, only the top electrode exists in this region. Therefore, the induced charge density on the top electrode is σ and its contribution to Q_{sc} is $\sigma wl/2$. For the plate electrode, both the top and bottom electrode exist in this region. A charge

density of σ_T will be induced on the top electrode, and σ_B on the bottom. Thus its contribution to Q_{sc} is $(\sigma_T-\sigma_B)wl/2$. Since the electric field inside the metal electrodes is 0, the following relationship exists:

$$\sigma_T + \sigma_B = \sigma \quad (6.1)$$

In addition, because the voltage between the top and bottom electrodes is 0 under SC conditions, we will have:

$$\frac{\sigma_T}{\varepsilon_0}\frac{d_1}{\varepsilon_{r1}} = \frac{\sigma_B}{\varepsilon_0}d_2 \quad (6.2)$$

This equation indicates that σ_T and σ_B will have the same sign. From Equation 6.1, $(\sigma_T-\sigma_B)$ will be obviously smaller than σ. Thus, the contribution of the plate electrode in region II to Q_{SC} is smaller than that of the grating electrode structure. Likewise, in regions III and IV, their contribution to Q_{SC} of the plate electrode is also smaller than that of the grating electrode. As a result, the total Q_{SC} generated by the plate electrode will be smaller. Therefore, through comparison of plate and grating electrode structures, it can be concluded that grating electrode structure is favourable for high output power. Thus, in the following discussion, we will mainly focus on TENGs with grating electrodes.

6.1.1.2 Influence of number of grating units (*n*)

The number of grating units (*n*) has a direct impact on the total output characteristics. When *n* starts to increase from 1, the approximate ideal charge distribution is still satisfied because *l* is still much larger than the thickness of dielectrics. However, when *n* is increased to fairly large values and *l* is comparable with d_1 or d_2, the non-ideal edge effect is significant and cannot be neglected any longer.

The influence of n in relatively small regions which satisfies the ideal conditions is first discussed. In this case, the instantaneous Q_{SC} and the short circuit current (I_{SC}) have the following relationships with n:

$$Q_{\mathrm{SC}} = \frac{\sigma w L}{2}\left[\frac{k}{n} + \frac{2(n-k)}{L}(x-2kl)\right], 2kl \le x \le (2k+1)l \quad (k \in N) \quad (6.3a)$$

$$Q_{\mathrm{SC}} = \frac{\sigma w L}{2}\left[1 - \frac{2(n-k-1)(x-2kl-l)}{L}\right], (2k+1)l \le x \le (2k+2)l \ \ (k \in N) \ \ (6.3b)$$

$$I_{SC} = \frac{\mathrm{d}Q_{\mathrm{SC}}}{\mathrm{d}x}\frac{\mathrm{d}x}{\mathrm{d}t} = \sigma w(n-k)\frac{\mathrm{d}x}{\mathrm{d}t}, 2kl \le x \le (2k+1)l \quad (k \in N) \quad (6.4a)$$

$$I_{SC} = \frac{\mathrm{d}Q_{\mathrm{SC}}}{\mathrm{d}x}\frac{\mathrm{d}x}{\mathrm{d}t} = -\sigma w(n-k-1)\frac{\mathrm{d}x}{\mathrm{d}t}, (2k+1)l \le x \le (2k+2)l \quad (k \in N) \quad (6.4b)$$

Therefore, the following equations give the accumulated charges ($Q_{\text{SC-rectified}}$) and charge transfer efficiency ($\eta_{\text{CT-rectified}}$) after rectification under SC conditions when a full displacement is finished:

$$Q_{\mathrm{SC,rectified}}(x = L) = \frac{\sigma w L}{2} n \qquad (6.5)$$

$$\eta_{\mathrm{CT,rectified}} = \frac{Q_{\mathrm{SC,rectified}}(x = L)}{Q_{\mathrm{tribo-total}}} = n \qquad (6.6)$$

From the above derivation, the peak value of I_{SC} and $Q_{\text{SC-rectified}}$ in the grating structure can be enhanced by n times through the subdivision process under ideal conditions, which is the most significant advantage of fabricating finer pitch structures.

To verify these results, a numerical calculation for a grating TENG under ideal conditions (L/d = 727.3, detailed calculation parameters are the same as shown in Table 6.1) is performed and the results are shown in Figure 6-2a-d. The numerically calculated results are consistent with the theoretical analysis above. When n increases, the number

of charge transfers increases as a response, which significantly elevates the amount of accumulated charges after rectification. In addition, the slope of $Q_{SC} - t$ curve also increases with n, leading to an enhancement of I_{SC}, as shown in Figure 6-2b. But as for voltage, since finer pitch results in a significant increase in capacitance when the top dielectrics and bottom dielectrics are fully separated, the peak value of V_{OC} at larger n significantly drops while the peak value of Q_{SC} remains almost the same, which is determined by the general V_{OC}, Q_{SC} and C equation (equation 2.3).

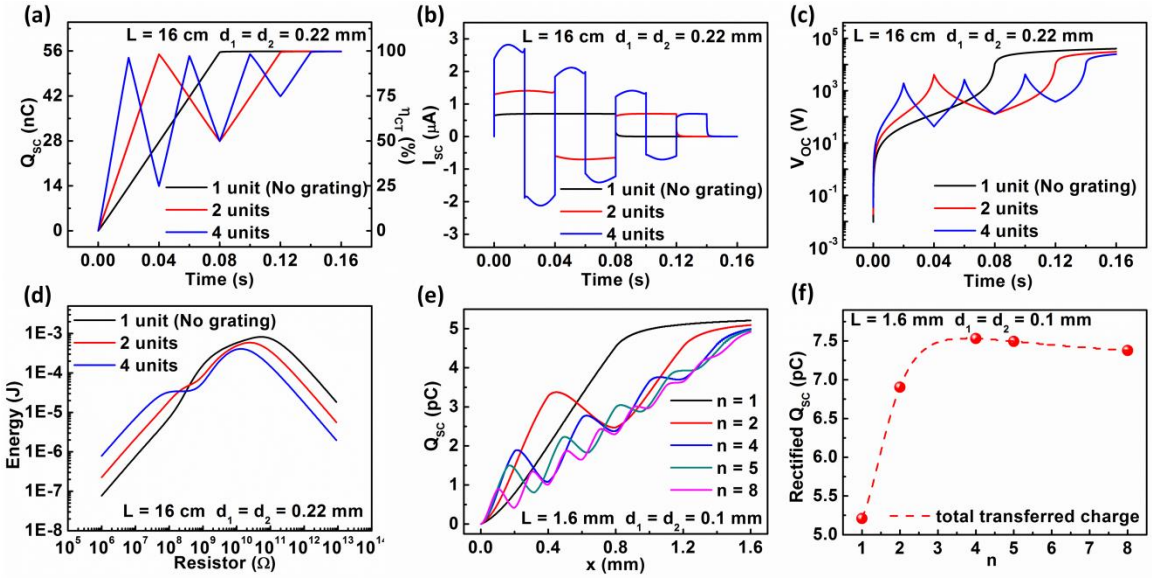

Figure 6-2. Influence of number of grating on the output performance of equal-length grating TENGs. (a-d) Influence of n in the ideal condition. (a) The relationship between transferred charges at short circuit and time at different n. (b) The relationship between current at short circuit and time at different n. (c) The relationship between open circuit voltage and time at different n. (d) The relationship between generated energy and load resistance at different n. (e-f) Influence of n in the non-ideal condition. (e) transferred charges at short circuit profile with moving distance at different n. (f) Total transferred charges relationship with n. Reproduced from reference [36]. Copyright 2014 Royal Society of Chemistry.

Such a change in V_{OC} is shown in Figure 6-2c. However, the total energy generated is more complicated, as it is determined by both the current and the voltage.

Figure 6-2d shows the energy generated by 3 TENG structures with different *n* in one full back-and-forth cycle under different load resistances. The following conclusions can be reached by comparing the curves shown in Figure 6-2d. First, a finer pitch can generate more energy in the low resistance range, where the energy is mainly dominated by I_{SC}. However, a wider pitch can generate more energy in the high resistance range, where the generated energy is mainly determined by V_{OC}. The optimum resistance (the resistance at which the total energy is maximized) decreases with *n*, due to the increase of the inherent TENG capacitance. Considering the peak value of the harvested energy (in Figure 6-2d), a finer pitch doesn't significantly improve the output, as V_{OC} decreases more significantly than I_{SC} increases for the equal-length grating TENGs.

When *n* continues to increase to very large values, the aspect ratio of each unit will be further lowered and the non-ideal edge effect cannot be neglected. To study the influence of this non-ideal effect, a numerical calculation for grating TENGs with a small *L*/*d* ratio of 16 was conducted, as shown in Figure 6-2e and f. (Detailed calculation parameters are shown in Table 6.2.) At this aspect ratio, although the times of charge transfer increases with increasing values of *n*, the peak value of Q_{SC} in each period is far smaller than that of Q_{tribo}. Especially when *n* is larger than 5, the transfer of charges is unidirectional after the first few cycles, so $Q_{SC\text{-}rectified}$ doesn't have a multiplication effect in these cycles. As a result, $Q_{SC\text{-}rectified}$ starts to drop with an increasing value of *n*. Because of the reverse influence of *n* in the two different regions, there is an optimum value of *n* that yields the maximum $Q_{SC\text{-}rectified}$. As shown in Figure 6-2f, for a total geometric aspect ratio, the optimum value of *n* is about 4, in which the geometric aspect ratio of each unit is 2. This calculation shows that it is critically important to have this

optimum value of n to generate the optimum charge when this kind of TENG is being used to charge a battery or capacitor.

Table 6.2. Parameters utilized in the FEM calculation for illustrating non-ideal effect for the equal-length grating TENGs.

Structure Component	Parameter Utilized
Dielectric 1	$\varepsilon_{r1} = 4$, $d_1 = 100$ μm
Dielectric 2	$\varepsilon_{r2} = 2$, $d_2 = 100$ μm
Width of Dielectrics w	1 mm
Total Length of the top plate L	1.6 mm
Tribo-charge surface density σ	7 μCm^{-2}
Velocity v	1 ms^{-1}

6.1.2 Grating structure with unequal-length plates

In the above section, we mainly discussed the design of grating TENGs with two plates of equal length. In such a structure, the top units will gradually slide out from the bottom grating due to lateral displacement. This feature is favourable for a high open-circuit voltage (because of the small side capacitance), but results in non-periodic signals. To avoid this situation, the length of the bottom plate that is stationary during operation can be increased to fully cover the sliding region of the top plate, which forms another structure of grating TENGs with plates of unequal length. As a typical example, the length of the bottom part is set to $2L$, which is twice the length of top part. Thus, the sliding displacement is maintained as L. In this structure, because of the charge conservation in contact electrification, the tribo-charge density of Dielectric 1 (-2σ) is twice as high as that of Dielectric 2 (σ). Because Dielectric 1 is always sliding within the range of Dielectric 2, Q_{SC}, V_{OC} and C will be periodic. In addition, the Q_{SC}, V_{OC} and C

curves all have mirror symmetry in each single period, which can be mathematically shown by the following set of equations.

$$V_{OC}(x + 2kl) = V_{OC}(x) \qquad (6.7a)$$

$$V_{OC}(2kl - x) = V_{OC}(x) \qquad (6.7b)$$

$$C(x + 2kl) = C(x) \qquad (6.7c)$$

$$C(2kl - x) = C(x) \qquad (6.7d)$$

$$Q_{SC}(x + 2kl) = Q_{SC}(x) \qquad (6.7e)$$

$$Q_{SC}(2kl - x) = Q_{SC}(x) \qquad (6.7f)$$

Because of the periodicity and mirror symmetry, we only need to simulate the TENG for its first half period. As for the electrode structure, the grating electrode still provides a better performance than the plate electrode in this case, which can be obtained from a similar discussion and derivation as above. Therefore, in the following discussion, we mainly focus on the unequal-length grating TENGs with the grating electrode.

6.1.2.1 Influence of dielectric thickness

Unlike equal-length grating TENGs, the choice of dielectric thickness can significantly influence Q_{SC}. Under ideal conditions (l/d is sufficiently large), Q_{SC} and η_{CT} of this grating TENG can be given by:

$$Q_{SC} = \left(2 - \frac{1}{1 + \frac{d_1\varepsilon_{r2}}{d_2\varepsilon_{r1}}}\right) n\sigma w(x - 2kl),$$

$$2kl \le x \le (2k + 1)l \quad (k \in N) \qquad (6.8a)$$

$$Q_{SC} = \left(2 - \frac{1}{1 + \frac{d_1 \varepsilon_{r2}}{d_2 \varepsilon_{r1}}}\right) n\sigma w(2kl + 2l - x),$$

$$(2k+1)l \le x \le (2k+2)l \ \ (k \in N) \quad (6.8b)$$

$$\eta_{CT} = \left(1 - \frac{1}{2}\frac{1}{1 + \frac{d_1 \varepsilon_{r2}}{d_2 \varepsilon_{r1}}}\right)\frac{x - 2kl}{l},$$

$$2kl \le x \le (2k+1)l \quad (k \in N) \quad (6.9a)$$

$$\eta_{CT} = \left(1 - \frac{1}{2}\frac{1}{1 + \frac{d_1 \varepsilon_{r2}}{d_2 \varepsilon_{r1}}}\right)\frac{2kl + 2l - x}{l},$$

$$(2k+1)l \le x \le (2k+2)l \ \ (k \in N) \quad (6.9b)$$

where n is defined as the number of units in top dielectrics. From the above equations, it is observed that Q_{SC} and η_{CT} decrease dramatically if the ratio of d_2/d_1 increases, which is because of the non-zero value of Q_0 from the not totally overlapped surface when $x = 0$. To minimize this effect, as shown in Equation 6.8, the ratio d_2/d_1 needs to be reduced. An effective design is to eliminate the dielectric layer on the bottom plate and use a conductive material as both electrode and tribo-layer, in which d_2 can be regarded as 0. In order to validate this, the performance of this conductor-to-dielectric structure ($d_2 = 0$) where $n = 4$ is compared with the dielectric-to-dielectric TENG structure ($d_2 = d_1$) as shown in Figure 6-3b-c. The detailed parameters for this calculation are listed in Table 6.3. The peak values of Q_{SC}, η_{CT} and V_{OC} from the conductor-to-dielectric TENG are all higher than the dielectric-to-dielectric TENG. Thus, the conductor-to-dielectric design is favourable for efficient charge transfer, from the point of

view of device structure. Therefore, we will mainly focus on this design in the following discussion.

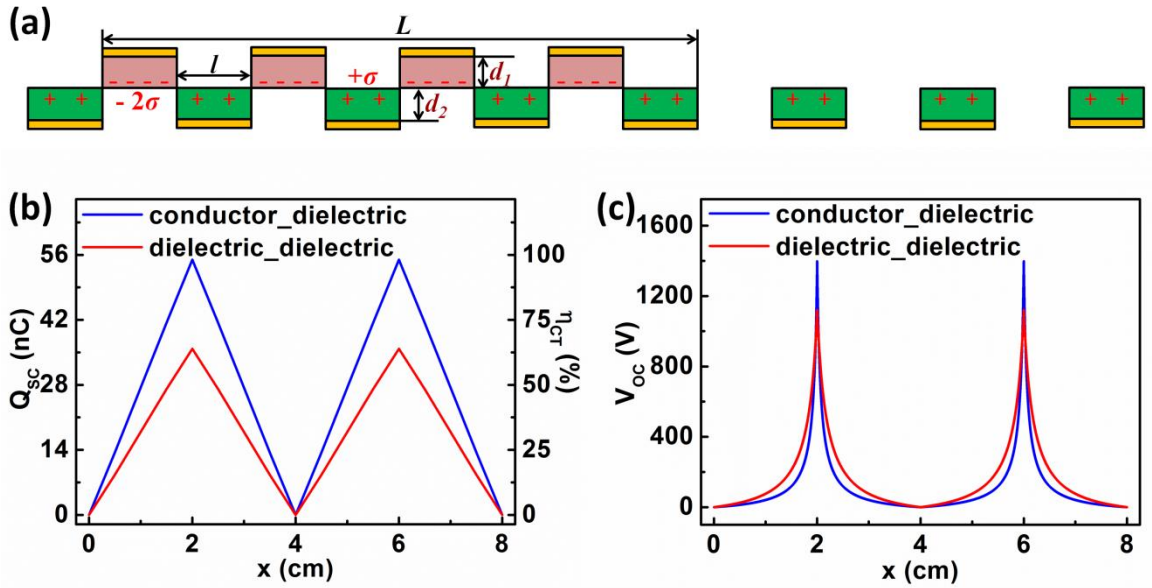

Figure 6-3. Influence of dielectric thickness on the performance of the unequal-length grating TENGs. (a) FEM model for the unequal-length grating TENGs. (b-c) Comparison of conductor-to-dielectric and dielectric-to-dielectric unequal-length grating TENGs on (b) short circuit transferred charges and (c) open circuit voltage. Reproduced from reference [36]. Copyright 2014 Royal Society of Chemistry.

Table 6.3 Parameters for FEM calculation for unequal-length grating TENGs

Structure Component	Dielectric-to-dielectric unequal-length grating TENGs	Conductor-to-dielectric unequal-length grating TENGs
Dielectric 1	$\varepsilon_{r1} = 4$, $d_1 = 220$ μm	$\varepsilon_{r1} = 4$, $d_1 = 220$ μm
Dielectric 2	$\varepsilon_{r2} = 2$, $d_2 = 220$ μm	Metal, $d_2 = 0$
Width of Dielectrics w	0.1 m	0.1 m
Total Length of the top plate L	0.16 m	0.16 m
Tribo-charge surface density at the bottom dielectric surface σ	3.5 μCm^{-2}	3.5 μCm^{-2}
Velocity v	1 ms^{-1}	1 ms^{-1}

6.1.2.2 Influence of number of grating units (n)

With the above basic understanding of the output characteristics of the unequal-length grating TENG, we can discuss the influence of the most important design parameter: the number of grating units. The output performance of a TENG with different n is calculated and plotted in Figure 6-4. When n increases in the small region, since the aspect ratio of each grating unit (l/d_1) is still large enough, the transferred charge amount in one half-cycle stays almost the same as Q_{tribo}. Therefore, since the total accumulated charges ($Q_{\text{SC,rectified}}(x = L)$) equals to $2n$ times the amount of transferred charge in one half-cycle, the total accumulated charges and average current magnitude increase quasi-linearly with n in its small value region, as shown in Figure 6-4b. However, when n continues to increase, the non-ideal edge effect becomes much more significant due to the decrease in the aspect ratio in each unit, resulting in a decreased number of transferred charges in each half-cycle. Although the number of charge transfer cycles still increases, the elevation slope of the total accumulated charges decreases dramatically. When n is sufficiently large, the slope of the total accumulated charges is close to 0 and the average current no longer increases. Additionally, finer pitches also contribute to a significant increase in the side capacitance between the top and bottom electrodes. Therefore, in Equation 2.3, V_{OC} will significantly drop with increased n, as shown in Figure 6-4d. Unlike the case in equal-length grating TENG, the V_{OC} and Q_{SC} curves in each half-cycle are always monotonic, even when n is sufficiently large. The peak value of the V_{OC} and Q_{SC} curves are always in the middle position of each period. With these characteristics, the unequal-length grating TENGs can have applications as a self-powered sensor for actively measuring the displacement and velocity with high accuracy and resolution.

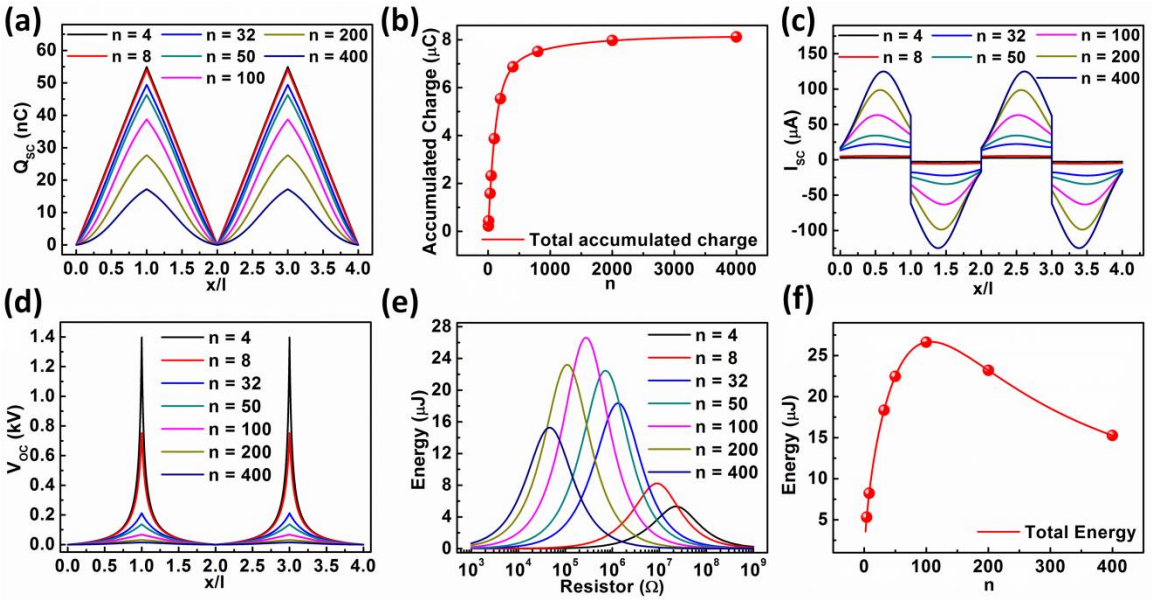

Figure 6-4. Influence of number of grating for unequal-length grating TENGs. (a) The relationship between transferred charges at short circuit in one period at different *n*. (b) Extracted total transferred charges when $x = L$. (c) The current profile at short circuit in one period at different *n*. (d) The voltage profile at open circuit in one period at different *n*. (e) The relationship between total generated energy and load resistance at different *n*. (f) Influence of *n* on the total generated energy. Reproduced from reference [36]. Copyright 2014 Royal Society of Chemistry.

With the above basic output characteristics, the load performance of these TENGs was numerically calculated, from which the total harvested energy was plotted corresponding to different load resistances, as shown in Figure 6-4e and f. Since finer pitches yield a larger inherent TENG capacitance, the optimum resistance shifts significantly to lower values. In addition, unlike the equal-length grating TENGs, an optimum value of *n* exists (about 108 through interpolation) for the unequal-length grating TENGs, which yields the maximum total harvested energy. With this optimum *n*, the aspect ratio is 3.37 for each grating unit. This optimum *n* originates from the complicated behavior of V_{OC} and I_{SC}. When *n* first increases, the average value of I_{SC} increases more significantly than V_{OC} decreases, so the harvested energy will increase.

However, when n continues increasing, the growth rate of I_{SC} decreases dramatically due to the non-ideal edge effect. Therefore, the total harvested energy starts to decrease when the decreasing V_{OC} becomes the dominant factor. This critical aspect ratio for the individual dielectric unit that yields the largest total energy mainly depends on the motion process and the relative dielectric constant of Dielectric 1. We can take the unequal-length grating TENG at constant velocity as an example. Under this condition, it can be mathematically proved that this critical aspect ratio is only dependent on the relative dielectric constant of Dielectric 1 (independent on d_1, L, and v).

6.2 Electrostatic shield effect in single-electrode triboelectric nanogenerators

In previous chapter, we have shown that the electrostatic shield effect is the main reason for the degraded performance of SETENGs.[26] Therefore, effective designs will try to minimize the influence of this electrostatic shield effect. In the following section, we will study the influences of the electrode gap distance and their area size on the output performance and elucidate the optimization strategy for SETENGs. [26]

6.2.1 Effect of electrode gap distance

Unlike attached-electrode TENGs, SETENGs have a fixed gap between their two electrodes, which are independent of the motion of Dielectric 1. This leads to an approximately fixed inherent capacitance C_0, which is critical to the performance of the whole device. To understand the influence of the gap (g), the intrinsic properties of the SETENG, i.e. V_{OC} and Q_{SC}, are calculated for SETENGs with different gap distances (g), as shown in Figure 6-5a and b. In this calculation, all of the other parameters used are the

same as shown in Table 3.1 except the gap distance, which is specified in each figure. At the same moving distance (x), V_{OC} rises up monotonically with the increase of g while Q_{SC} decreases. When g is large enough, the raise speed V_{OC} is quite slow and V_{OC} approaches to its saturation value. Similarly, when g approaches to 0, Q_{SC} also approaches to its saturation value.

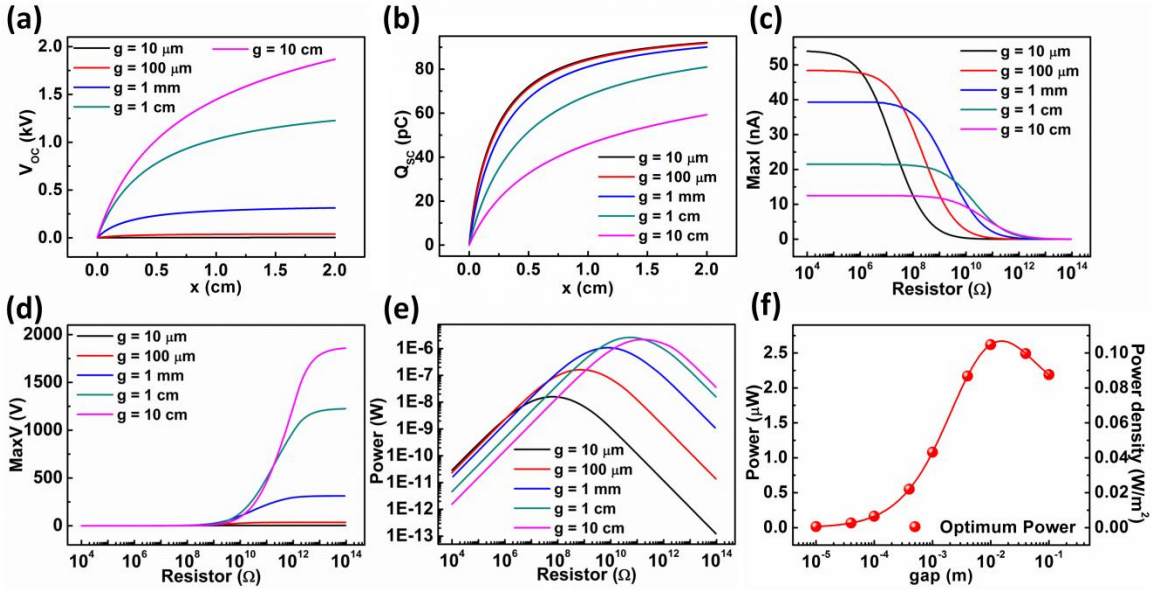

Figure 6-5. Influence of gap distance (g) on the output performance of the single-electrode TENG. (a) The relationship between open circuit voltage and separation distance at different gap distances. (b) The relationship between transferred charges at short circuit and separation distance at different gap distance. (c-e) Maximum output (c) current profile, (d) voltage profile, and (e) power profile with load resistance at different gap distances. (f) Extracted optimum power profile with gap distance. Reproduced from reference [26]. Copyright from 2014 Wiley.

This influence of g can be interpreted utilizing the equivalent circuit built above. When g increases, C_b and C_0 decreases significantly while C_a is barely affected. Therefore, C_2 and C_3 decrease significantly while C_1 maintains almost the same value. In addition, the decrease of C_3 is in a higher rate than that of C_2. Therefore, from Equation

3.19-3.21, V_{OC} monotonically increases with the increase of g while Q_{SC} monotonically decreases to 0.

Besides the basic trend of V_{OC} and Q_{SC}, their saturation behavior can be theoretically understood as well. First, the saturation behavior of V_{OC} when g is sufficiently large is discussed. When g is sufficiently large, C_b and C_0 approach to 0 at the same rate while C_a is almost unaffected. Therefore, C_2 and C_3 approach to 0 with its ratio approaching to 1 while C_1 approaches to C_a. Thus, V_{OC} saturates to the value of $\sigma wl/(2C_a)$ when g is large enough.

The saturation behavior of Q_{SC} can also be interpreted. When g decreases to 0, C_o is getting close to infinity and C_a equals to C_b. Thus, both C_1 and C_2 are approaching to $C_a/2$. As a result, Q_{SC} approaches to its saturation value $\sigma wl/2$.

Besides the fundamental property, the influence of the gap on the load characteristics is investigated as well. The output current, voltage, and transit power peak were calculated under different load resistances for SETENGs with different g, as shown in Figure 6-5c-e. A smaller gap provides a larger inherent capacitance, leading to the decrease of the optimum resistance. The relationship between the maximum transit power and the gap distance is plotted in Figure 6-5f. An optimum gap about 1.54 cm is observed to generate the maximized transit power.

6.2.2. Effect of area size (length)

Besides the gap between the electrodes, another important design parameter is the area size (represented by the length l in this 2D model) of the SETENG. To systematically study its influence, V_{OC}, Q_{SC}, and η_{CT} of the SETENG with different

length l is calculated through the COMSOL software, as shown in Figure 6-6a-c. All of the parameters utilized in this calculation are the same as listed in Table 3.1**,** except that the value of x_{max} utilized in the calculation is 2 cm. From the calculation results, for any given x, there exists a specific l to generate the largest V_{OC}. In addition, when x increases, this l for the largest V_{OC} also increases. Q_{SC} should have been proportional to the length l, but this is true only when l is sufficiently small. When l is large enough, the Q_{SC}-l curve shifts downwards dramatically, which shows that η_{CT} decreases significantly when l is large.

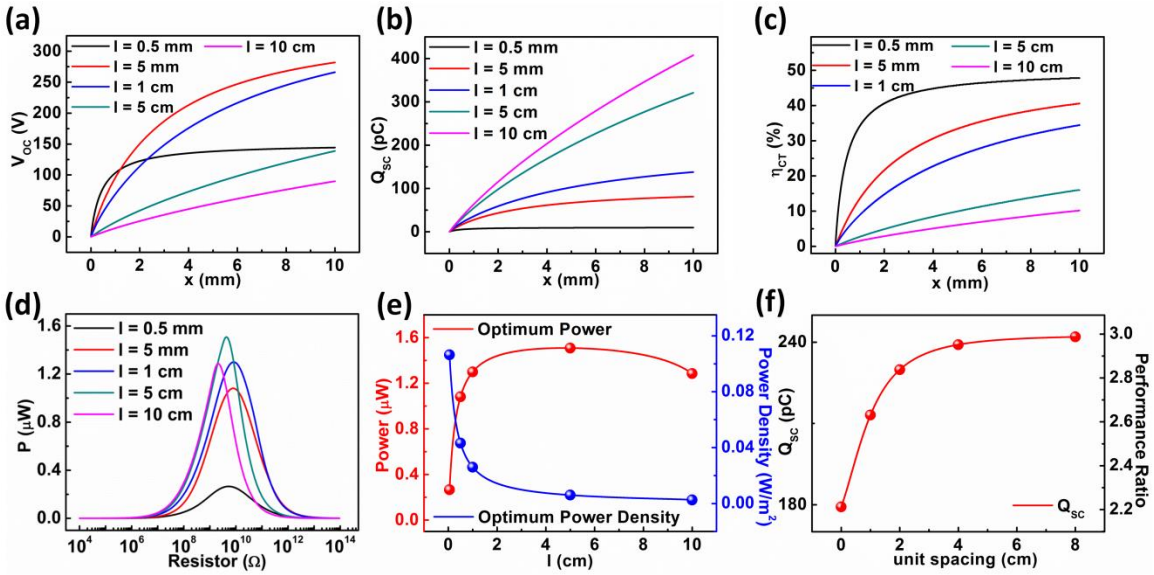

Figure 6-6. The influence of area size/length on the output characteristics of the single-electrode TENG. (a) open circuit voltage profiles with separation distances for SETENGs with different lengths. (b) short circuit transferred charges profile with separation distances for SETENGs with different lengths. (c) short circuit charge transfer efficiency profile with separation distances for SETENGs with different lengths. (d) Maximum output power profile with load resistance for SETENGs with different lengths. (e) Extracted optimum power and power density profile with length of SETENG. (f) The influence of unit spacing on the short circuit transferred charges in a three-SETENG system. Reproduced from reference [26]. Copyright from 2014 Wiley.

The complicate behavior of the influence of l to outputs of SETENGs can be understood from the equivalent circuit built above. The capacitances C_a, C_b, and C_0 are first calculated, which are all 2D parallel electrode capacitances. For an non-ideal 2D parallel electrode capacitance considering the edge effect, its capacitance value can be shown as the following equation,[37]

$$C = \frac{\varepsilon_0 wl}{d}\left\{1 + \frac{d}{\pi l}\left\{1 + \ln\left[1 + \frac{2\pi l}{d} + \ln(1 + \frac{2\pi l}{d})\right]\right\}\right\} = \frac{\varepsilon_0 wl}{d}[1 + \alpha\left(\frac{d}{l}\right)] \qquad (6.10)$$

where l is its length, w is its width and d is the separation distance between the two parallel electrodes. Inside Equation 6.10, the edge effect is reflected by the function $\alpha(y)$:

$$\alpha(y) = \frac{y}{\pi}\left\{1 + \ln\left[1 + \frac{2\pi}{y} + \ln(1 + \frac{2\pi}{y})\right]\right\} \qquad (6.11)$$

With C_a, C_b, and C_0 calculated through the above equation, C_1, C_2, and C_3 can be analytically calculated utilizing Equation 3.16-3.18. Thus, from the calculated C_1, C_2, and C_3, V_{OC}, Q_{SC}, and η_{CT} can be analytically calculated through Equation 3.19-3.21. Their behaviors at the two l limits are shown below.

When l approaches to 0 (x/l and g/l is very large):

$$V_{OC} = \frac{\sigma}{2\varepsilon_0}\pi l \quad (6.12a) \qquad Q_{SC} = \frac{\sigma wl}{2} \quad (6.12b) \qquad \eta_{CT} = \frac{1}{2} \qquad (6.12c)$$

When l approaches to infinity (x/l and g/l is close to 0):

$$V_{OC} = \frac{\sigma g x \ln(l)}{\pi \varepsilon_0 l} \quad (6.13a) \qquad Q_{SC} = \frac{\sigma w x}{\pi}\ln(l) \quad (6.13b) \qquad \eta_{CT} = \frac{x}{\pi l}\ln(l) \quad (6.13c)$$

From Equation 6.12a and 6.13a, the behavior of V_{OC} can be quite easily understood. When l is small, V_{OC} is proportional to l and increases with the increase of l. But when l is large enough, V_{OC} satisfies Equation 6.13a and starts to drop. Therefore, there is an optimum l at which V_{OC} reaches its maximum. When x or g increases, a larger

range of l can satisfy the condition for Equation 6.12, so that the l providing the maximum V_{OC} rises. For Q_{SC}, when l is small (condition of Equation 6.12), Q_{SC} is proportional to l and increases dramatically with the increase of l. When l is sufficiently large (condition of Equation 6.13), Q_{SC} is proportional to ln(l), resulting in a much lower slope of Q_{SC} - l curve. From the Q_{SC} behavior, η_{CT} is close to 50% when l is small and decays to 0 when l is sufficiently large. This analysis clearly explains the FEM calculation results shown in Figure 6-6.

Besides these intrinsic characteristics, the resitive load characteristics of the contact-mode SETENG are studied as well. Because V_{OC} and η_{CT} of SETENGs with infinite l are 0, an optimum l of 4.7 cm is observed to generate the maximum total transit power, as shown in Figure 6-6d and 6-6e. In addition, the optimum resistance increases first then starts to decrease when l increases. This is because when l first increases, V_{OC} increases at a faster speed than I_{SC}, Region II of the single electrode shifts to a higher resistance range and the optimum resistance increases.[26] When l further increases, V_{OC} starts to decrease and I_{SC} continues increasing. Thus, the optimum resistance starts to decrease.[26] Moreover, the peak power density is monotonically lowered when l increases, which is because larger area l lowers η_{CT}. Thus, unlike the attached-electrode TENGs, SETENGs are not optimized for direct scaled-up processing.

6.2.3 Effect of unit spacing for scale up

Finally, the effect of connecting several SETENGs in parallel is discussed, which is another way to scale-up the output from SETENGs besides increasing the area size. For a three-SETENG system, a simulation was performed at OC condition through FEM

calculation, in order to study the influence of the spacing between each SETENG. The total Q_{SC} generated by the three SETENGs with different spacing is shown in Figure 6-6f. When the unit spacing is small, electric field from each SETENG will interfere, resulting in a decrease of η_{CT} for each SETENG, which is similar to the effect of increasing l on one SETENG. Only when their spacing is large enough, the mutual influence will be minimized, so that there will be little decrease on η_{CT}. From Figure 6-6f, to reach the total charge transfer amount more than 270% of that for each SETENG, a minimum unit spacing of 1.24 cm is observed, about 2.5 times the length of an individual SETENG. Therefore, a large enough spacing is critical for the scale-up of the output through parallel connection.

6.3 Superior linear characteristics of contact-mode freestanding triboelectric nanogenerators and their application in harvesting vibration energy

As discussed above, the most advantage of this CFTENG structure is its superior linearity. [29] The linear dependence of both V_{OC} and Q_{SC} on x makes it an ideal medium to transform mechanical vibration signal to electrical signal. Besides, the constant inherent capacitance makes it a linear and time-invariant device. Thus, the electrical signal output of this device is compatible with all the currently available signal processing techniques, making it easy to accomplish post-processing of the obtained electrical signal. Therefore, this structure could have wide applications in self-powered vibration detection.

Besides the self-powered sensor application, this superior linearity is also beneficial in vibration energy harvesting applications as well. To fully uncover its advantages, we design a device structure that can harvest vibration energy under both

freestanding-mode and traditional attached-electrode mode, as shown in Figure 6-7a. When metal 1 and metal 2 are directly utilized as two electrodes and metal 3 and 4 are suspended with no output terminal, this device is working in the freestanding-mode (shown in the right solid line). If metal 1 and metal 4 are connected to form Node A, metal 2 and metal 3 are connected to form Node B and then Node A and Node B are utilized as the output terminals to connect with external load circuits, the device is working in traditional attached-electrode mode, which is equivalent to two parallel-connected attached-electrode TENGs. The reason to connect metal 1 and 4 rather than metal 1 and 2 to form the output node is to ensure the polarity of these two TENGs is consistent.

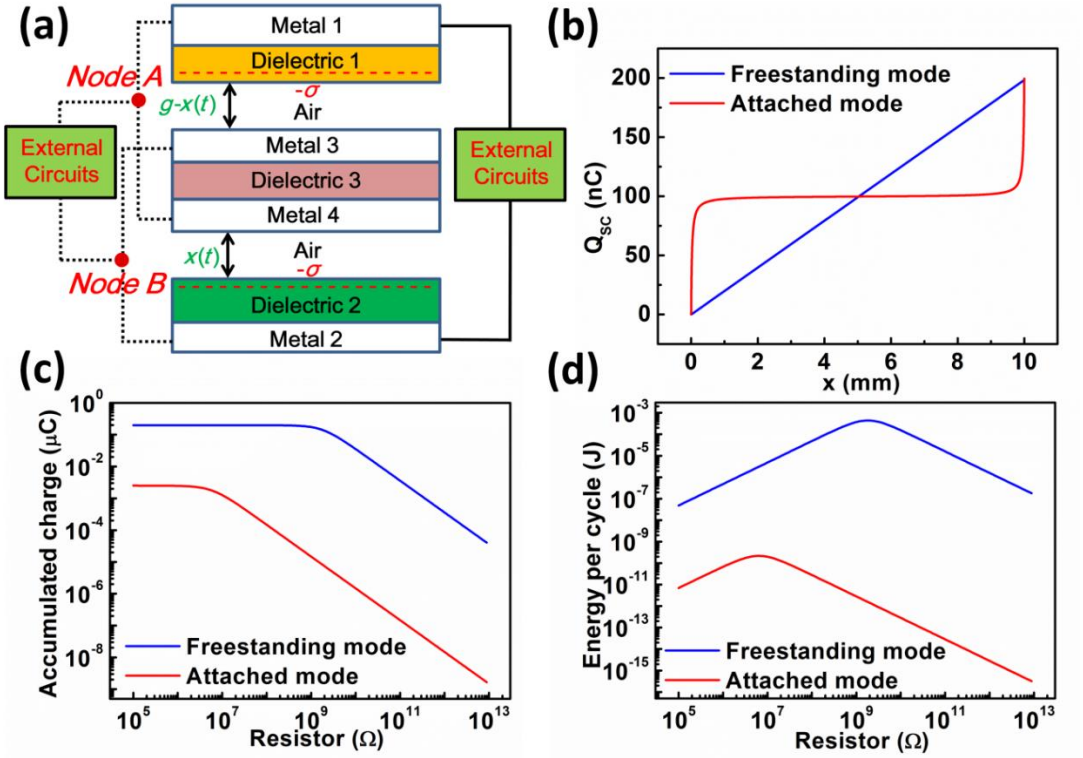

Figure 6-7. The advantages of contact-mode freestanding TENGs in harvesting vibration energy compared to traditional contact-mode attached-electrode TENGs. (a) Structure of the carefully designed TENG which can work in both freestanding mode and traditional attached-electrode mode. (b) Compare of short-circuit transferred charges characteristics under these two modes. (c-d) When the vibration amplitude is only a quarter of the air gap, the comparison of these two modes considering (c) the amount of the transferred charges and (d) harvested vibration energy in one cycle under different load resistance. Reproduced from reference [29]. Copyright Elsevier 2015.

As a comparison, Q_{SC} under both two operation-modes are numerically calculated utilizing the same parameters and plotted in Figure 6-7c. Although for both of these two-modes, their $Q_{sc\text{-}final}$ (short-circuit transferred charge amount when a full separation is reached) can reach $2\sigma S$, the shape of Q_{SC} is completely different. For the freestanding mode, Q_{SC} changes linearly with x, ensuring a relative high slope in the whole x range. However, for the traditional attached-electrode mode, Q_{SC} only has a huge slope at the two ends. When x is between $0.05g$ to $0.95g$, Q_{SC} is nearly a constant. Therefore, when the traditional attached-electrode mode is utilized to harvest vibration energy with

vibration amplitude which is not large enough to ensure the freestanding layer to fully contact with the two electrodes (which is always the case in practical application), the total short-circuit transferred charges will be strongly limited. As an example, this device is utilized to harvest a harmonic vibration whose vibration amplitude is $g/4$ and center position is $x = g/2$. The steady state electrical outputs under these two modes are numerically calculated through the TENG simulator utilizing the periodic boundary condition. As shown in Figure 6-7c, the amount of transferred-charges of the freestanding mode is more than 70 times higher than the attached-electrode mode in all the resistance ranges. In addition, the optimum energy harvested from the freestanding-mode is several orders larger than the attached-electrode mode. From the above comparison, we can conclude that the linearity of the freestanding mode is highly beneficial for harvesting the mechanical energy from the vibration that cannot ensure good contact of the moving object and the two electrodes, which will also save energy loss from the inelastic collision and increase the energy conversion efficiency.

6.4 Optimization for sliding-mode freestanding triboelectric nanogenerators

6.4.1 Tolerance to the freestanding height

The most significant advantage of the SFTENG structure is its excellent tolerance to the freestanding height h.[29] This loosens the requirement of the sliding object and reduces the energy loss due to the friction. The influence of the freestanding height on the output performance of dielectric SFTENGs is first investigated. Besides the parameter specified in the figure, the value of all the other parameters are the same as listed in Table 3.2. From Figure 6-8a, $Q_{SC,final}$ decreases when h increases, which is mainly because of

the reduce of the difference between $(C_2(k)/C_1(k))_{x=0}$ and $(C_2(k)/C_1(k))_{x=g+l}$. Specifically, when $h = 0$, $C_2(k)/C_1(k)$ equals to 0 at the position of $x = 0$ and equals to infinity at the position of $x = g + l$, so $Q_{SC,final}$ can reach σwl. When h is large enough, the average distance between the tribo-charge surface and two electrodes will be approximately the same. Thus both $(C_2(k)/C_1(k))_{x=0}$ and $(C_2(k)/C_1(k))_{x=g+l}$ are approximately 1, resulting in a zero $Q_{sc,final}$. But the decreasing slope with height is much flatter than the attached-electrode STENG case. From the numerical calculation results, the half-life height that $Q_{SC,final}$ reduces to its half-value for attached-electrode sliding-mode TENGs is 250 μm, while that for SFTENG structure is about 2 cm. As for the capacitance profile shown in Figure 6-8b, the increase of h only slightly decreases the total capacitance since the capacitance in the dielectric SFTENGs is mainly from the direct capacitance between metal 1 and metal 2. For the V_{OC} profile of the dielectric SFTENG shown in Figure 6-8c, it almost has the same trend with Q_{SC}, for the capacitance almost has no dependence with h. As for the total energy-R curve, this degradation of both Q_{SC} and V_{OC} will lead to the decrease of the maximum harvested energy when h increases. However, the optimum resistance stays almost the same, which is because of the nearly same inherent capacitance for different h.

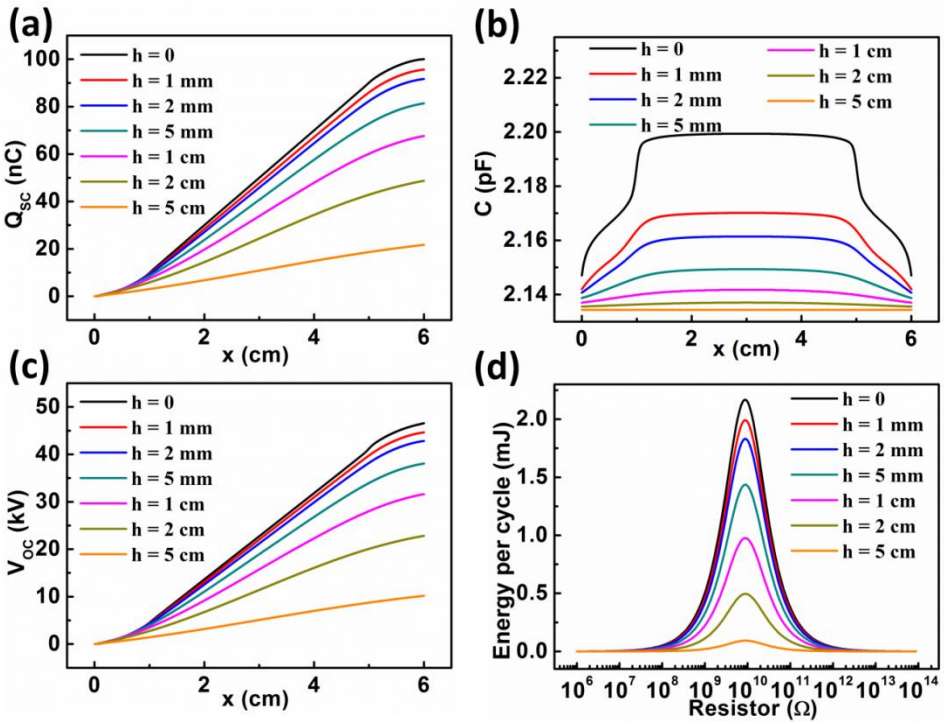

Figure 6-8. Tolerance of height for dielectric sliding-mode freestanding TENGs. (a-c) Influence of the freestanding height h on (a) Q_{SC} curves under MACRS, (b) total capacitance curves, and (c) V_{OC} curves under MACRS of the dielectric SFTENG. (d) The harvested energy by the dielectric SFTENG in one cycle under different load resistance and different h. Reproduced from reference [29]. Copyright Elsevier 2015.

For metal SFTENGs, their height characteristics have some similarity with dielectric SFTENGs, but it will still have several differences. Since the basic electrostatic induction mechanism in the metal SFTENG system is very similar to that of dielectric SFTENG system, the change of Q_{SC} profiles with height is similar to that of dielectric SFTENG system. However, there are still many differences. When h increases, the influence of the metal layer on the electrostatic system reduces and both C_{f1} and C_{f2} significantly decrease. Thus, as shown in Figure 6-9b, the total capacitance at the middle position is largely affected when h first increases from 0. When h is large enough, the total capacitance starts to be dominated by the direct parasitic capacitance between the two electrodes and is nearly independent of x. At this time, the metal SFTENGs are

indistinguishable with the dielectric SFTENGs. As for the open-circuit voltage shown in Figure 6-9c, the metal SFTENGs also show a very complicated profile, which is because both Q_{SC} and C have strong dependence on the freestanding height. $V_{OC\text{-}final}$ will decrease because of a reduced $Q_{SC\text{-}final}$ and an almost non-changed C in that region. However, at the middle region, V_{OC} will increase first when h increases then decreases when h is already large enough. This is because the decreasing speed of the serial connection of C_{f1} and C_{f2} is faster than the decreasing speed of Q_{SC} in this region. When h is small and x is in the middle range, this serial connection dominates the total capacitance and V_{OC} has this unusual increase. As for the total harvested energy, it also has the similar decay trend as the dielectric SFTENGs. However, since the average total capacitance drops with the increase of h, the optimum resistance shifts to the right when h first increases and finally stays on the value which is almost the same as the dielectric SFTENGs.

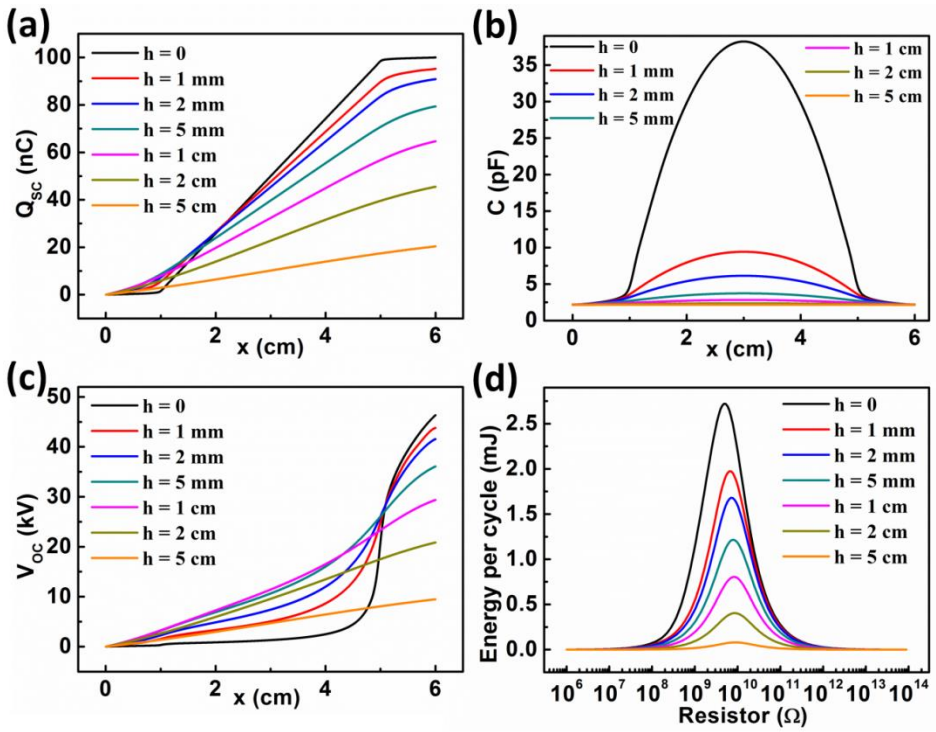

Figure 6-9. Tolerance of height for metal sliding-mode freestanding TENGs. (a-c) Influence of the freestanding height h under g = 1cm condition on (a) Q_{SC} curves under MACRS, (b) total capacitance curves, and (c) V_{OC} curves of the metal SFTENG under MACRS. (d) The harvested energy by the metal SFTENG in one cycle under different load resistance and different h. Reproduced from reference [29]. Copyright 2015 Elsevier.

6.4.2 Influence of the gap between electrodes

Besides the freestanding height h, another important design parameter is the gap distance between the electrodes (g). The capacitance between the electrodes is strongly dependent on the gap distance. Therefore, the gap distance will have strong effect on the total output characteristics.

The effect of g on the total output performance for dielectric SFTENGs under h = 0 conditions is studied first and plotted in Figure 6-10. Besides the parameters specified in the figure, all the other parameters is the same as listed in Table 3.2. Since h equals to 0, the ratio $C_2(k)/C_1(k)$ is still 0 when x = 0 and infinity when $x = g+l$. Therefore, the charge transfer efficiency η_{CT} can still reach 100% for all the g values and $Q_{SC\text{-final}}$ will

not change with g. However, the capacitance between the two electrodes decreases when g increases, as shown in Figure 6-10b. Thus, through equation 2.3, $V_{OC\text{-final}}$ when a full separation is reached will increase with g. Therefore, considering the total energy harvested in one cycle, the dielectric SFTENG with a higher g will generate a larger total energy with a higher optimum resistance. However, for dielectric SFTENGs with a higher g, their cycle (T) is also longer when the average velocity stays the same. Therefore, the average power (defined as equation 6.14a) will have a different trend with the total harvested energy, as shown in Figure 6-10d.

$$P_{avg} = \frac{R\int_0^T I^2 \mathrm{d}t}{T} \quad (6.14a) \qquad T = \frac{2(l+g)}{v} \quad (6.14b)$$

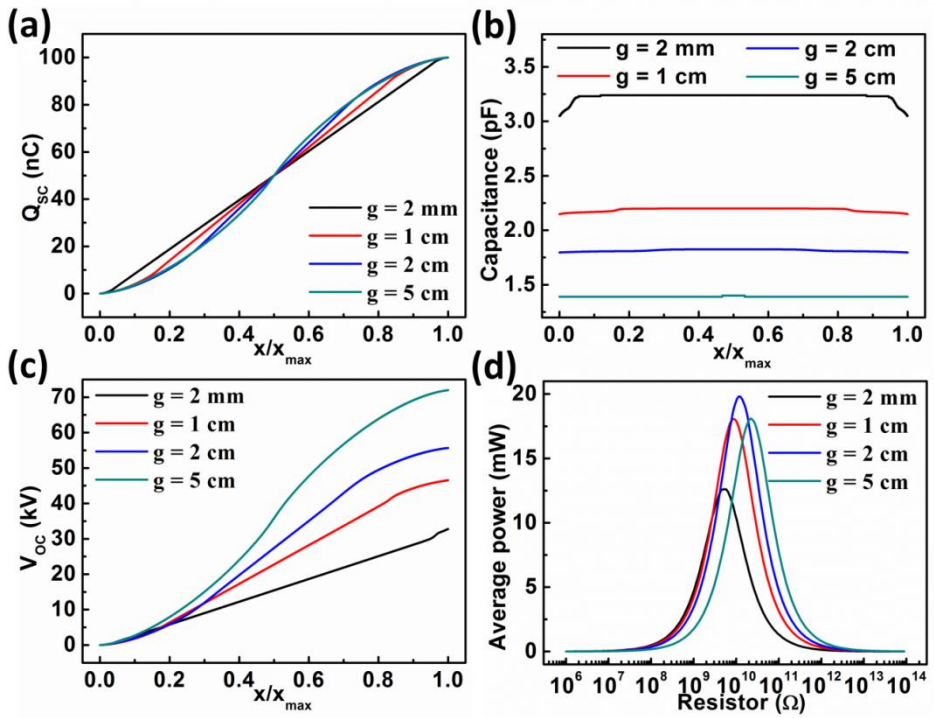

Figure 6-10. Influence of the gap on the output performance of dielectric sliding-mode freestanding TENGs. (a-c) Influence of the electrode gap g under h = 0 condition on (a) Q_{SC} curves under MACRS, (b) total capacitance curves, and (c) V_{OC} curves of the dielectric SFTENG (under MACRS). (d) The average power by the dielectric SFTENG in one cycle under different load resistance and different g. Reproduced from reference [29]. Copyright 2015 Elsevier.

When g first increases from 0, the cycle length increases only a little because l still dominates the total cycle length. Therefore, the increase of $V_{OC\text{-}final}$ dominates the total average power and average power increases with g. However, when g is already very large, the decreasing slope of the total capacitance is flattened. Therefore, the increase of $V_{OC\text{-}final}$ cannot catch up with the increasing speed of T and the average power begins to drop. Thus, an optimum gap is observed to generate the largest average power.

For metal SFTENGs under h = 0 conditions, similar results have also been observed. The charge transfer efficiency η_{CT} can still reach 100% for all the g values and $Q_{SC\text{-}final}$ will not change with g. The total capacitance of metal SFTENGs also decrease with the increase of g, but this decrease contributes from two reasons. The first reason is the same as dielectric SFTENGs, which will lead to the decrease of the direct parasitic capacitance between these two electrodes. Besides, when g increases, the region when the freestanding layer are overlapped with both of the two electrodes decreases, leading a decrease of the serial connection of C_{f1} and C_{f2}. When g is larger than l, the region that the freestanding layer is overlapped with both electrodes no longer exists and the serial connection of C_{f1} and C_{f2} can be neglected. The influence of g on V_{OC} of metal SFTENGs is very similar to the case in dielectric SFTENGs. $V_{OC\text{-}final}$ will increase with the increase of g. Also, similar to the dielectric SFTENGs, the optimum resistance still increases when g increases and there is an optimum gap to reach the highest average power.

Besides the h = 0 case we discussed above, the influence of the gap distance will be much more complicated if there is a non-zero freestanding height. When h is non-zero, the capacitance ratio $C_2(k)/C_1(k)$ is no longer 0 when x = 0 and no longer infinity when x = g+l. And if the gap decreases, the difference of the capacitance ratio $C_2(k)/C_1(k)$

between $x = 0$ position and $x = g+l$ position will reduce as a response, resulting in a decrease of $Q_{SC\text{-}final}$. The 3d plot of $Q_{SC\text{-}final}$ under different h and g for dielectric SFTENG is shown in Figure 6-11a. Consistent with our theoretical analysis, when g increases, the slope of $Q_{SC\text{-}final}$-h curve decreases and the dielectric SFTENG has more tolerance to the height h. In addition, $Q_{SC\text{-}final}$ will increase with the increase of g when h is a non-zero constant and the slope of $Q_{SC\text{-}final}$-g curves increase when h goes up. As for the average power shown in Figure 6-11b, there is still an optimum gap value when h increases. This optimum gap at which the highest average power is reached increases with h, as a result of better tolerance of height for larger gap devices. For metal SFTENGs, similar results have also been observed.

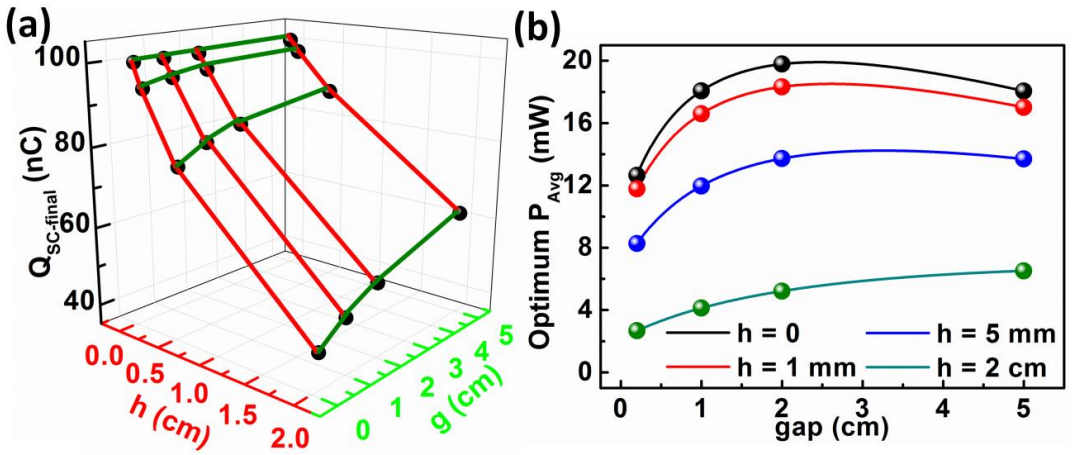

Figure 6-11. Coupling effect of gap and height on the output performance of dielectric sliding-mode freestanding TENGs. (a) Dependence of the short circuit transferred charge when a full separation is reached on the freestanding height and the electrode gap. (b) Influence of the freestanding height on the optimum gap at which the maximum average power is reached. Reproduced from reference [29]. Copyright 2015 Elsevier.

CHAPTER 7

STANDARDS AND FIGURE-OF-MERITS FOR QUANTIFYING THE PERFORMANCE OF TRIBOELECTRIC NANOGENERATORS

To improve the performance and broaden the applications of TENG, numerous efforts have been made with focus on both enhancement of the surface charge density σ [13] and development of new structures/modes.[13,16,18,22,38] However, without a common standard it becomes difficult to evaluate the performance of a TENG. In comparison to its counter parts, standards have been established for alternative power generators, such as Carnot efficiency for heat engines [39,40] and pyroelectric nanogenerators [41,42], ZT factor for thermoelectric materials [43,44], and energy conversion efficiency for solar cells [45,46]. As described in previous chapters, several modes of TENG have been developed, including attached-electrode contact-mode (AEC), attached-electrode sliding-mode (AES), single-electrode (SE) mode, and freestanding-triboelectric-layer (FT) mode. Each mode has its own structure and choice of materials as well as specific mechanical triggering configurations. To evaluate and compare the performance of the TENGs in different structures/modes, a universal standard has to be introduced to quantify the performance of the TENG regardless its operation mode.

We proposed a standard method to quantitatively evaluate TENG's performance from both structure's and the materials' points of view.[47] Starting from the plot of built-up voltage V - total transferred charges Q, the TENG operation cycle with maximized energy output is firstly proposed. Based on this cycle, a performance figure-of-merit

(FOM) is proposed for TENG, which consists of a structural FOM related to the design of the TENG and a material FOM as the square of the surface charge density. To characterize and compare different structures of TENGs, the structural FOM for each configuration of TENG is derived and simulated. A standard method is proposed to quantify the material FOM. The proposed standards will set the foundation for the further applications and industrialization of the TENGs.

7.1 Operation cycles of triboelectric nanogenerators

7.1.1 *V-Q* plot and its characteristics

The fundamental working principle of the TENG is a conjugation of contact electrification and electrostatic induction. For a basic triboelectric nanogenerator, there is at least one pair of triboelectric layers (two pairs for FT mode and one pair for other modes) that are facing each other for creating opposite triboelectric charges via physical contacts. Besides the triboelectric layers, there are two electrodes (for SE mode, the ground can be utilized as the second/reference electrode[26]) that are carefully insulated from each other, which are required for the free electrons to be transferred between them through an external load. Triggered by the external mechanical force, there is a periodical relative motion between the triboelectric layers that breaks the balanced distribution of electrostatic charges; as a result, free electrons are driven to flow between the electrodes in order to build a new equilibrium. Therefore, the governing equations of TENG can be developed based on the relationship among the transferred charges between the electrodes Q, the built-up voltage V, and the relative displacement x between the triboelectric layers. Usually, we define the status while one pair of the triboelectric layers

are fully contacting with each other as $x = 0$, and $x = x_{max}$ is defined at the farthest achievable displacement. (Please be noticed that actually the x_{max} can be picked at any displacement larger than 0. In application, the x_{max} is fixed inside a range which depends on the structural design.) The detailed definitions of x for different structures of TENG are illustrated below (in Figure 7-3). We use the most commonly utilized minimum achievable charge reference state (MACRS),[29] so both the absolute short-circuit transferred charges $Q_{SC}(x)$ and the absolute open-circuit voltage $V_{OC}(x)$ at $x = 0$ position are set to be 0. The definitions of the displacement x and the two electrodes for an attached-electrode sliding-mode TENG are illustrated in Figure 7-1a. The maxima of $Q_{SC,max}$ and $V_{OC,max}$ are expected to be reached at $x = x_{max}$ for these basic modes of TENG.

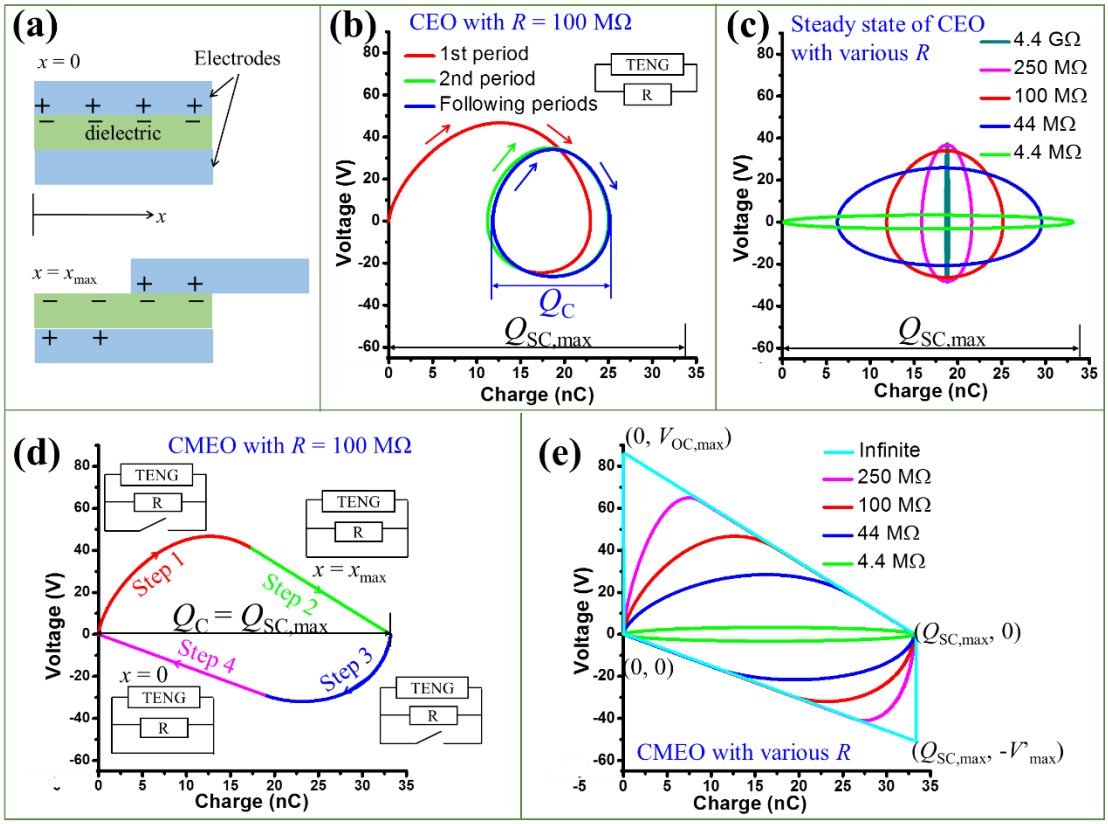

Figure 7-1. Operation cycles of TENG. (a) Schematic diagram of the attached-electrode sliding-mode TENG with displacement $x = 0$ and $x = x_{max}$; (b) The cycle for energy output (CEO) with load resistance $R = 100$ MΩ. The total cycling charge Q_C was marked and the inset shows the operation circuit; (c) The steady-state of CEO with various load resistances; (d) The cycle for maximized energy output (CMEO) with load resistance $R = 100$ MΩ, with the maximum total cycling charge $Q_C = Q_{SC,max}$. The insets show the corresponding status of the switch in circuits during different steps; (e) The CMEO with various load resistances. The vertices of the CMEO with infinite load resistances are marked. Reproduced with permission from Nature Publication Group.[47]

For a continuous periodic mechanical motion, the electrical output signal from the TENG is also periodically time-dependent. In such a case, the average output power $\bar{P}$, which is related to the load resistance, is used to determine the merits of the TENG. Given a certain period of time T, the output energy per cycle E can be derived as:

$$E = \bar{P}T = \int_0^T VI\mathrm{d}t = \int_0^T V\mathrm{d}Q = \oint V\mathrm{d}Q \qquad (7.1)$$

Therefore, the electrostatic states and the energy output of TENG can be represented by the plot of built-up voltage *V* against the transferred charges *Q*.

Based on the *V*-*Q* curves, different operation cycles were developed to quantitatively describe the working status of TENG. Currently reported cycles include that of energy output and maximized energy output for TENG connected with a load resistance, and the direct charging cycle and the designed charging cycle for TENG to charge a battery or capacitor. In following sections, we mainly focused on the former two since they are closely related to the figure-of-merits as proposed.

7.1.2 Cycle of energy output

The *V*-*Q* plot for an attached-electrode siliding-mode TENG was firstly simulated by finite element method (FEM) operated under external load resistance of 100 MΩ, starting from (*Q*, *V*) = (0, 0). The parameters of this attached-electrode sliding-mode TENG was shown in Table 7.1. From the *V*-*Q* plot, we noticed that the operation of the TENG will go to its steady state after only a few periods (Figure 7-1b), and thus we can directly focus on the output of the steady-state operation. Because the steady-state output signal of TENG is periodic in responding to the mechanical triggering, the *V*-*Q* plot should be a closed loop. As indicated by Equation 7.1, the output energy per cycle *E* can be calculated as the encircled area of the closed loop in the *V*-*Q* curve. The steady-state *V*-*Q* plots for this TENG were also simulated by FEM under various external loads, as shown in Figure 7-1c. From the encircled areas of these *V*-*Q* curves, we noticed that the output energy per cycle *E* can be optimized by applying a matched load resistance.[25] The cycles given here can be named as “cycles for energy output” (CEO). For each CEO, the

difference between the maximum and the minimum transferred charges in its steady-state is defined as the total cycling charge Q_C, as marked in Figure 7-1b.

Table 7.1. Parameters used to simulate the attached-electrode sliding-mode TENG.

Dielectric effective thickness d_0	90.8 μm
Triboelectrification Area A (Length l × Width w)	8.5 cm × 7.9 cm
Maximum displacement x_{max}	3.5 cm
Surface charge density σ	12 μC m^{-2}

7.1.3 Cycle of maximized energy output

From Figures 7-1 b and c, it is noticed that for each CEO, the total cycling charge Q_C was always less than the maximum transferred charges $Q_{SC,max}$, especially for cycles with large external load resistances. If we could maximize the Q_C to be $Q_{SC,max}$ for these cycles, the output energy per cycle E would be further enhanced. Having noticed that the $Q_C = Q_{SC,max}$ occurs at short-circuit condition, following repeated steps are designed to achieve instantaneous short-circuit conditions during operations, with the use of a switch in parallel with the external load (as shown in Figure 7-1d): step 1, triboelectric layers displace relatively from $x = 0$ to $x = x_{max}$ at switch off; step 2, turn the switch on to enable $Q = Q_{SC,max}$, and then turn the switch off; step 3, triboelectric layers displace relatively from $x = x_{max}$ to $x = 0$ at switch off; step 4, turn the switch on to enable $Q = 0$, and then turn the switch off. Therefore, the maximized total cycling charge $Q_C = Q_{SC,max}$ was enabled by the instantaneous short-circuit conditions in steps 2 and 4, as controlled by the switch. The simulation results with respect to various external load resistances were plotted as Figure 7-1e. These cycles can be named as "cycles for maximized energy output" (CMEO). Clearly, benefited from the maximized total cycling charges, the output

energy per cycle of the CMEO was always higher than that of the CEO with the same load resistance *R*, as observed in the encircled areas in Figures 7-1 c and e.

We noticed that for the CMEO, higher output energy per cycle can be achieved with larger external load resistance *R* (Figure 7-1e). So the maximized output energy per cycle can be achieved at $R = +\infty$, which is the open-circuit condition. We simulated this maximized output energy by simply removing the external load and operating the remaining part of the circuit the same as that for the steps in the CMEO case as stated above. The corresponding *V*-*Q* curve was plotted as the CMEO with infinite load resistance as shown in Figure 7-1e. This CMEO has a trapezoid shape, the vertices of which are determined by the maximum short-circuit transferred charge $Q_{SC,max}$, the maximum open-circuit voltage $V_{OC,max}$, and the maximum achievable absolute voltage V'_{max} at $Q = Q_{SC,max}$. It can be easily proven that the *V*-*Q* plots for all kinds of the TENG operations are limited inside the four edges of this trapezoid as following:

We only consider the charge Q with $0 \leq Q \leq Q_{SC,max}$ since the motion part only operates between $x = 0$ and $x = x_{max}$. $0 \leq Q \leq Q_{SC,max}$ represents two of the four boundary lines.

At arbitrary displacement *x*, the capacitance was fixed at $C(x)$. Therefore, as the electrical potential superposition of the open-circuit voltage and the voltage drop due to the charge transfer, the total voltage was derived as:

$$V = -\frac{1}{C(x)}Q + V_{OC}(x) \quad (7.2)$$

Here we defined a variable $V'(x)$, which is the absolute voltage value when $Q = Q_{SC,max}$ at displacement *x*. So from the definitions, at fixed *x*, (*Q*, *V*) plots (Equation 7.2)

should include points of ($Q_{SC}(x)$, 0), (0, $V_{OC}(x)$) and ($Q_{SC,max}$, -V'(x)). By putting these points into Equation 7.2 we can get:

$$V'(x) = \left| -\frac{Q_{SC,max}}{C(x)} + V_{OC}(x) \right| = \frac{Q_{SC,max}}{C(x)} - V_{OC}(x) = \frac{Q_{SC,max} - Q_{SC}(x)}{C(x)} \qquad (7.3)$$

Then the relationship among $Q_{SC}(x)$, $V_{OC}(x)$, $C(x)$ and $V'(x)$ can be shown as:

$$C(x) = \frac{Q_{SC}(x)}{V_{OC}(x)} = \frac{Q_{SC,max} - Q_{SC}(x)}{V'(x)} \qquad (7.4)$$

If we replace $C(x)$ in Equation 7.2 by Equation 7.4, we can get:

$$\frac{V}{V_{OC}(x)} + \frac{Q}{Q_{SC}(x)} = 1 \qquad (7.5a)$$

$$-\frac{V}{V'(x)} + \frac{Q_{SC,max} - Q}{Q_{SC,max} - Q_{SC}(x)} = 1 \qquad (7.5b)$$

$V_{OC}(x)$ and $Q_{SC}(x)$ always increase with the increase of x. Therefore, at x = 0, $V_{OC}(x)$ and $Q_{SC}(x)$ should achieve their minimum value $V_{OC}(0) = 0$ and $Q_{SC}(0) = 0$; and at $x = x_{max}$, $V_{OC}(x)$ and $Q_{SC}(x)$ should achieve their maximum value $V_{OC}(x_{max}) = V_{OC,max}$ and $Q_{SC}(x_{max}) = Q_{SC,max}$. Therefore, $0 \le Q_{SC}(x) \le Q_{SC,max}$, $0 \le V_{OC}(x) \le V_{OC,max}$.

We noticed if we define a new displacement $x' = x_{max} - x$, and redefine the MACRS in this new coordinate system as $V_{OC}'(x') = 0$ and $Q_{SC}'(x') = 0$ at $x' = 0$. There would be $Q_{SC}'(x') = Q_{SC,max} - Q_{SC}(x)$ and $C'(x') = C(x)$ from the definitions. Therefore,

$$V'(x) = \frac{Q_{SC,max} - Q_{SC}(x)}{C(x)} = \frac{Q'_{SC}(x')}{C'(x')} = V'_{OC}(x') \qquad (7.6)$$

So as the open-circuit voltage at this new charge reference state, $V_{OC}'(x') = V'(x)$ should achieve the minimum value 0 at $x' = 0$ and the maximum value V'_{max} at $x' = x_{max}$. Then there would be $0 \le V'(x) \le V'_{max}$.

So for arbitrary (Q, V) with displacement x and satisfying Equation 7.5:

When $V \geq 0$, $\frac{V}{V'(x)} + \frac{Q}{Q_{\mathrm{SC,max}}} \geq 0$ is always valid, and we also have,

$$\frac{V}{V_{\mathrm{OC,max}}} + \frac{Q}{Q_{\mathrm{SC,max}}} \leq \frac{V}{V_{\mathrm{OC}}(x)} + \frac{Q}{Q_{\mathrm{SC}}(x)} = 1 \qquad (7.7a)$$

When $V < 0$, $\frac{V}{V_{\mathrm{OC,max}}} + \frac{Q}{Q_{\mathrm{SC,max}}} < \frac{Q}{Q_{\mathrm{SC,max}}} \leq 1$ is always valid, we also have,

$$\frac{V}{V'_{\mathrm{max}}} + \frac{Q}{Q_{\mathrm{SC,max}}} = \frac{V}{V'_{\mathrm{max}}} - \frac{Q_{\mathrm{SC,max}} - Q}{Q_{\mathrm{SC,max}}} + 1 \geq \frac{V}{V'_{\mathrm{max}}} - \frac{Q_{\mathrm{SC,max}} - Q}{Q_{\mathrm{SC,max}} - Q_{\mathrm{SC}}(x)} + 1 = 0 \quad (7.7b)$$

Therefore, for any (Q, V) in any states of the TENG, we can derive that:

$$V \leq V_{\mathrm{OC,max}} - V_{\mathrm{OC,max}} \frac{Q}{Q_{\mathrm{SC,max}}} \quad (7.7c)$$

$$-V \leq V'_{\mathrm{max}} \frac{Q}{Q_{\mathrm{SC,max}}} \quad (7.7d)$$

Equation 7.7 represents the other two of the four boundary lines. Then the four boundary lines of the V-Q curves were fixed.

Thus, with the largest encircled area, this cycle has the largest possible output energy per cycle, which can be calculated using the following equation:

$$E_{\mathrm{m}} = \frac{1}{2} Q_{\mathrm{SC,max}} \left(V_{\mathrm{OC,max}} + V'_{\mathrm{max}} \right) \qquad (7.8)$$

E_{m} is demonstrated to be the largest possible output energy per cycle: For TENG under arbitrary operations, energy per cycle $E = \oint V \mathrm{d}Q$, we can divide the route into two parts:

Part 1: when $V \geq 0$, $\mathrm{d}Q/\mathrm{d}t = I = V/R \geq 0$, so Q will always increase at $V \geq 0$ (assume it is from $Q_{1\mathrm{min}}$ to $Q_{1\mathrm{max}}$);

Part 2: when $V < 0$, $\mathrm{d}Q/\mathrm{d}t = I = V/R < 0$, so Q will always decrease at $V < 0$ (assume it is from $Q_{2\mathrm{max}}$ to $Q_{2\mathrm{min}}$);

So: $E = \oint V\mathrm{d}Q$

= (Part 1: $V \geq 0$) $\int_{Q_{1,\min}}^{Q_{1,\max}} V\mathrm{d}Q$ + (Part 2: $V < 0$) $\int_{Q_{2,\max}}^{Q_{2,\min}} V\mathrm{d}Q$

= (Part 1: $V \geq 0$) $\int_{Q_{1,\min}}^{Q_{1,\max}} V\mathrm{d}Q - $ (Part 2: $V < 0$) $\int_{Q_{2,\min}}^{Q_{2,\max}} V\mathrm{d}Q$

$\leq$ (Part 1) $\int_{Q_{1,\min}}^{Q_{1,\max}} \left(V_{\mathrm{OC,max}} - \frac{V_{\mathrm{OC,max}}Q}{Q_{\mathrm{SC,max}}}\right)\mathrm{d}Q$ + (Part 2) $\int_{Q_{2,\min}}^{Q_{2,\max}} V'_{\max}\frac{Q}{Q_{\mathrm{SC,max}}}\mathrm{d}Q$

$\leq \int_{0}^{Q_{\mathrm{SC,max}}} \left(V_{\mathrm{OC,max}} - \frac{V_{\mathrm{OC,max}}Q}{Q_{\mathrm{SC,max}}} + V'_{\max}\frac{Q}{Q_{\mathrm{SC,max}}}\right)\mathrm{d}Q$

$= \frac{1}{2}Q_{\mathrm{SC,max}}\left(V_{\mathrm{OC,max}} + V'_{\max}\right) = E_{\mathrm{m}}$

7.1.5 Experimental realization of the operation cycles

Here we also demonstrated that the CEO and the CMEO can be easily achieved experimentally. An AES mode TENG with parameters close to that in Table 7.1 was fabricated. An aluminum (Al) foil was used as one electrode and the motion part. The copper (Cu) layer deposited on the fluorinated ethylene propylene (FEP) film was utilized as the other electrode. The Al foil and the FEP film are the pair of triboelectric layers. Firstly, the *V*-*Q* plot of CEO was demonstrated by using an external load resistance of 250 MΩ, as shown in Figure 7-2a. We noticed that the steady-state of the CEO was achieved only after a few periods of operation. And then, controlled by a switch in parallel, the *V*-*Q* plot of CMEO with external load resistances of 250 MΩ and infinite were also demonstrated, as shown in Figures 7-2 b and c, respectively. All of the features of the three *V*-*Q* plots are very consistent with the simulated results as shown in Figure 7-1. We found that the trends of the characteristics with the varied resistances of these plots are very consistent with that of the simulated results. We can easily conclude from the encircled areas that the output energy per cycle of the CMEO with infinite external load

resistance was the highest one in that of these cycles. The output energy per cycle was calculated using Equation 7.1, as shown in Table 7.2. These results demonstrated and further confirmed that the experimental-achievable CMEO can harvest the maximized output energy per cycle. In fact, the instantaneous discharging TENG with a switch triggered by the motion of TENG, which was actually operated in CMEO, has been demonstrated to have gigantic enhanced instantaneous power compared to the traditional TENG operated in CEO.[47]

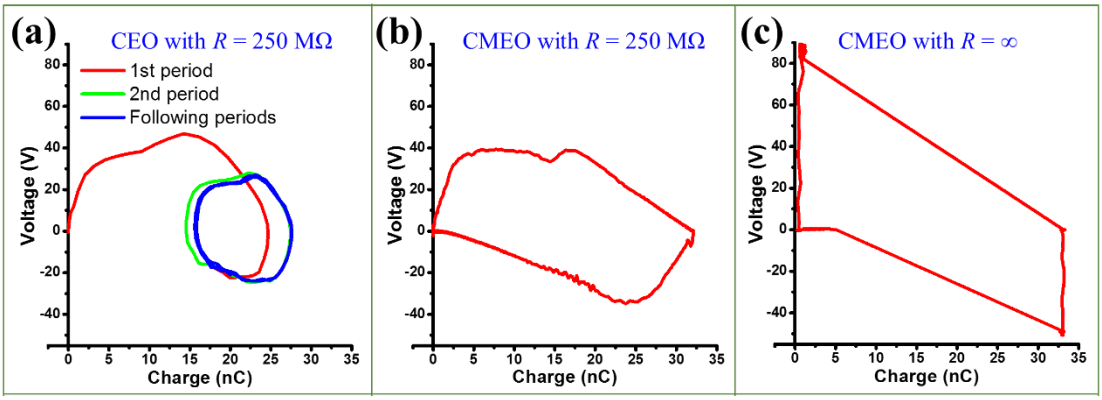

Figure 7-2. Experimental results of the *V*-*Q* plot of (a) the CEO with external load resistance of 250 MΩ; (b) the CMEO with external load resistance of 250 MΩ; (c) the CMEO with infinite external load resistance. Reproduced with permission from Nature Publication Group.[47]

Table 7.2. Output energy per cycle for the three cycles operated in the attached-electrode sliding-mode TENG.

Cycle type	Output energy per cycle
CMEO with $R = +\infty$	1.99 μJ
CMEO with $R = 250$ MΩ	1.48 μJ
CEO with $R = 250$ MΩ	0.47 μJ

7.2 Figure-of-Merits of triboelectric nanogenerators

For the TENG operating in CMEO with infinite load resistance, the period *T* includes two parts of time. One part is from the relative motion in TENG, and the other

part is from the discharging process under short-circuit condition. With the minimal resistance in short-circuit condition, the second part of T can be short enough so that it can be omitted (less than 0.4 ms experimentally as reported[48]). Thus, the average output power $\bar{P}$ at CMEO should satisfy:

$$\bar{P} = \frac{E_{\mathrm{m}}}{T} \approx \frac{E_{\mathrm{m}}\bar{v}}{2x_{\max}} \qquad (7.9)$$

where, $\bar{v}$ is the average velocity value of the relative motion in TENG, which depends on the input mechanical motions. In this equation, $E_{\mathrm{m}}/x_{\max}$ is the only term that depends on the characteristics of the TENG itself.

On the other hand, the energy conversion efficiency of the TENG can be expressed as (at CMEO with $R = +\infty$):

$$\eta = \frac{E_{\mathrm{out}}}{E_{\mathrm{in}}} = \frac{E_{\mathrm{m}}}{E_{\mathrm{m}} + E_{\mathrm{dissipation}}} = 1/\left[1 + 1/\left(\frac{E_{\mathrm{m}}}{2\bar{F}x_{\max}}\right)\right] \qquad (7.10)$$

Here, $\bar{F}$ stands for the average dissipative force during the operation of the TENG. This force can be frictional force, air resistance force or others.

Therefore, from both Equations 7.9 and 7.10 we conclude that the term $E_{\mathrm{m}}/x_{\max}$ determines both the average power and the energy conversion efficiency from the characteristics of TENG itself. We also notice that as indicated in Equation 7.8, E_{m} contains $Q_{\mathrm{SC,max}}$ that is proportional to the triboelectrification area S. Therefore, to exclude the effect of the TENG size on the output energy, the area A should be placed in denominator of this term. Due to the reasons stated above, we confirm that the term $E_{\mathrm{m}}/Sx_{\max}$ determines the merits of TENG.

We notice that in Equation 7.8, $Q_{\mathrm{SC,max}}$, $V_{\mathrm{OC,max}}$ and $V'_{\max}$ are all proportional to the surface charge density σ. Therefore, E_{m} is proportional to the square of the surface

charge density σ. Then we can define a dimensionless structural FOM (FOM_S) of TENG, as the factor only depends on the structural parameters and x_{max}:

$$FOM_S = \frac{2\varepsilon_0}{\sigma^2}\frac{E_m}{Sx_{max}} \qquad (7.11)$$

Here, ε_0 is the permittivity of the vacuum. This structural FOM represents the merit of the TENG from the structural design. And then the performance FOM (FOM_P) of TENG can be defined as:

$$FOM_P = FOM_S\sigma^2 = \frac{2\varepsilon_0 E_m}{Sx_{max}} \qquad (7.12)$$

in which the σ^2 can be the material FOM (FOM_M), which is the only component related to the material properties. The performance FOM can be considered as the universal standard to evaluate varieties of TENGs, since it is directly proportional to the greatest possible average output power and related to the highest achievable energy conversion efficiency, regardless of the mode and the size of the TENG.

7.3 Structural figure-of-merit: calculation and simulation

Currently, several basic modes of TENGs have been developed for various applications.[49,50] To compare these TENGs from the structural design's point of view, the structural FOM of AEC mode, AES mode, single-electrode contact (SEC) structure in SE mode, sliding freestanding triboelectric-layer (SFT) and contact freestanding triboelectric-layer (CFT) structures in FT mode TENGs, were calculated by their analytical formulas and simulated by FEM, with the same surface charge density σ and area A.

The detailed simulation method is described in following: We assume that each TENG takes surface charge density σ. All the electrodes have the size of area (A) = length (l) × width (w). The sliding direction in AES and SFT structures is along the length direction. The maximum displacement of the motion part is x_{max}, and the effective thickness of the dielectric layer is defined as $d_0 = \Sigma_i d_i/\varepsilon_{ri}$ in which d_i and ε_{ri} represent the thickness and dielectric constant of each dielectric layer, respectively. The capacitances between different electrodes and triboelectric surfaces are marked in Figure 7-3, and $C_{Total}(x)$ is the total capacitance, which is the capacitance between two electrodes. The parameters for each structure of TENG were listed in Figure 7-3 and Table 7.3.

Table 7.3. Parameters used in simulation for different structures of TENG

Structure		AEC	AES	SEC	SFT	CFT
Dielectric		Effective thickness $d_0 = \Sigma d_i/\varepsilon_{ri}$ = 50 μm				
Air		Relative dielectric constant ε_r = 1				
Electr-odes	Size	Area A = Length l × Width w = 0.1 m × 0.1 m = 0.01 m^2				
	Thickness	d_m = 1 μm				
Triboelectric surface charge density		σ = 10 μC m^{-2}				
Displacement x_{max}		0~0.2 m	0~0.1 m	0~1 m	0~0.101 m	0~0.01 m
Gap between electrodes g		-	-	1 cm	1 mm	1 cm

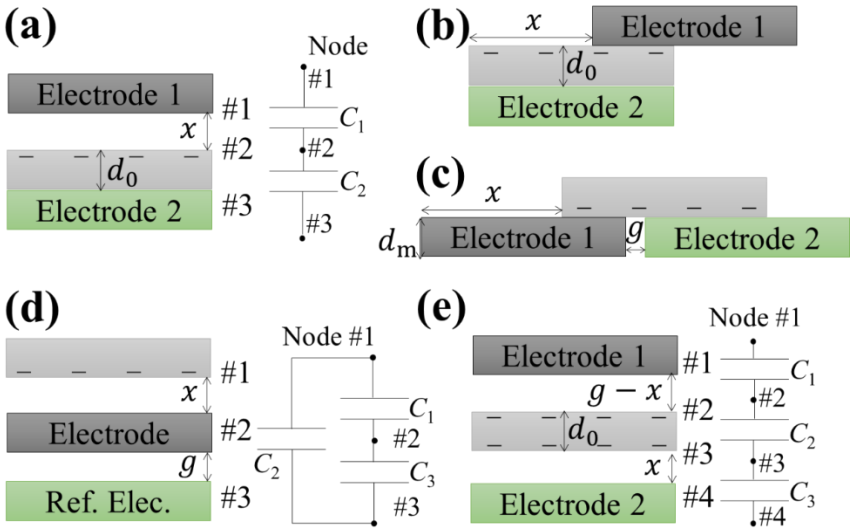

Figure 7-3. Illustration of symbols in 5 structures of TENG. (a) Attached-electrode contact-mode (AEC) TENG with capacitance $C_1(x)$ between electrode 1 (node #1) and triboelectric surface of the dielectric layer (node #2), and capacitance C_2 between node #2 and electrode 2 (node #3); (b) Attached-electrode sliding-mode (AES) TENG; (c) Sliding freestanding triboelectric-layer (SFT) structure TENG; (d) Single-electrode contact (SEC) structure TENG with capacitance $C_1(x)$ between triboelectric surface of the dielectric layer (node #1) and the electrode (node #2), capacitance $C_2(x)$ between node #1 and the reference electrode (node #3), and capacitance $C_3(x)$ between nodes #2 and #3. These capacitances are "virtual" capacitances as described in Reference [26]; (e) Contact freestanding triboelectric-layer (CFT) structure TENG with capacitance $C_1(x)$ between electrode 1 (node #1) and the top triboelectric surface of the dielectric layer (node #2), capacitance C_2 between node #2 and the bottom triboelectric surface of the dielectric layer (node #3), and capacitance $C_3(x)$ between nodes #3 and electrode 2 (node #4). Reproduced with permission from Nature Publication Group.[47]

The analytical formulas of $V_{OC,max}$ and $Q_{SC,max}$ in AEC, AES, SEC and CFT structures have been given in previous chapters. For these structures, the V'_{max} can also be derived by the models in the previous section. The AES structure with $x_{max} > 0.95l$ and SFT structure were not calculated due to the lack of analytical formulas. That is because in the both cases, the capacitances C_{Total} are between two fully misaligned parallel plates, which currently don't have appropriate analytical formulas. And besides, the analytical formulas of $Q_{SC}(x)$ cannot be derived, either, since they are strongly related to the side effects.

And then, the largest possible output energy per cycle E_m was calculated by Equation 7.8 and the structural FOM with respect to different x_{max} was calculated by Equation 7.11.

The calculated structural FOMs for the five structures with respect to varied maximum displacement x_{max} were plotted and compared in Figure 7-4. For AEC, SEC and CFT structures, the non-ideal parallel capacitances considering both one-side (1S) and two-side (2S) edge effects were used for calculations by analytical formulas, while in the FEM simulation only one-side (1S) edge effect was considered. The calculated results from the analytical formulas fit the FEM simulation results very well. We can extract the maximum value of the structural FOM ($FOM_{S,max}$) from FEM simulations as a standard criterion for evaluating the structures. As shown in Figure 7-4f and Table 7.4, we found for $FOM_{S,max}$:

CFT >AES > SFT > AES > SEC

Table 7.4. The simulated maximum structural FOM ($FOM_{S,max}$).

Structure	$FOM_{S,max}$
CFT	6.81
AEC	0.98
SFT	0.45
AES	0.15
SEC	0.022

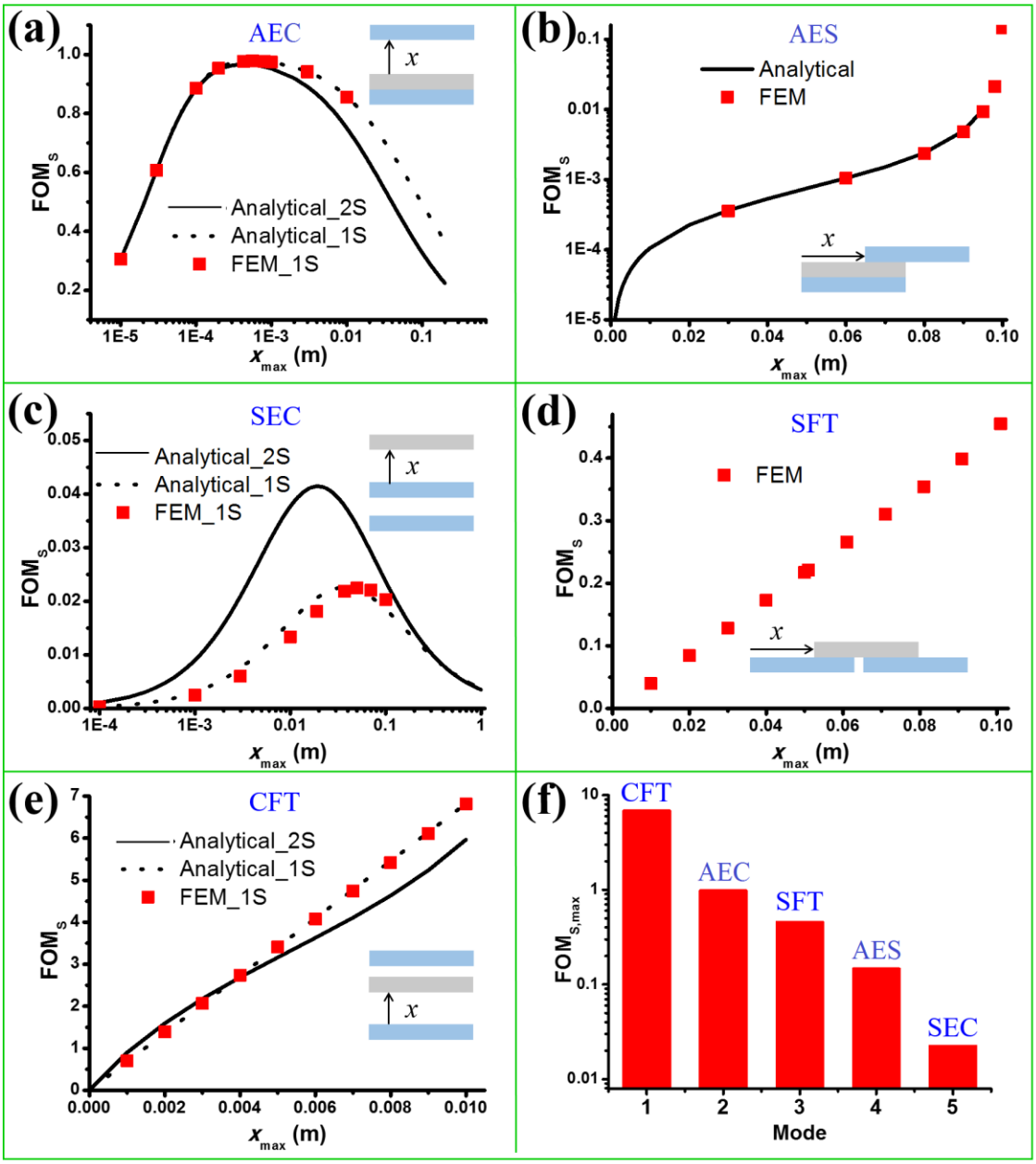

Figure 7-4. FOM_S versus x_{max} for different TENG structures. (a) ~ (e) FOM_S for attached-electrode contact-mode (AEC), attached-electrode sliding-mode (AES), single-electrode contact (SEC) structure, sliding freestanding triboelectric-layer (SFT) structure and contact freestanding triboelectric-layer (CFT) structure calculated by analytical formulas and FEM simulation. The insets show the corresponding schematic diagrams of the corresponding structures. 1S and 2S stand for calculations and simulations considering 1-side and 2-side side effects of the non-ideal parallel-plate capacitor; (f) The maximum structural FOM ($FOM_{S,max}$) of different structures extracted from FEM simulations. Reproduced with permission from Nature Publication Group[47].

Here we can make several general conclusions. Firstly, the performance of the paired-electrode TENGs is dramatically better than that of single-electrode TENGs with the same size and materials, due to the limited transferred charges and suppressed built-in voltages in single-electrode TENG, which has been discussed in Chapter 3.[26] Secondly, the performance of TENG triggered by contact-separation action is better than that of TENG triggered by sliding (assuming the triboelectric charge densities created by contact-separation and sliding are the same), because to achieve the same $V_{OC,max}$, a much higher x_{max} of TENG triggered by sliding is required compared with that of TENG triggered by contact-separation, resulting in a smaller $FOM_{S,max}$. Finally, the freestanding configuration enhances the performance by dramatically decreasing the capacitance between electrodes. The high $FOM_{S,max}$ of CFT structure is also benefited by the large transferred charges induced by the double-side triboelectrification of the middle dielectric layer during operation (as shown in Figure 7-3e).

7.4 Measurement of material figure-of-merit

The triboelectric surface charge density σ is the only material-related parameter in performance FOM as shown in Equation 7.12. The optimization of σ would enhance the performance of TENG significantly since the performance FOM is proportional to σ^2. This surface charge density was determined by the triboelectric performance of the materials in contact. Since the existing triboelectric series is a qualitative measure of the materials' triboelectric performances,[49] a quantitative measuring matrix is required for TENGs.

Current studies of the triboelectric performance are influenced by the low contact intimacy induced by the nanometer-to-micrometer-level surface roughness in solid materials.[12,51,52] Therefore, the measured surface charge density by solid-solid contact was not able to reach its highest possible value. To overcome this limitation of the solid surface and to build the measuring matrix for triboelectric performance of materials, we can utilize liquid metals such as liquid gallium (Ga, melting point: 29.8 ^{o}C), galinstan (a eutectic alloy consisting of 68.5 wt% gallium, 21.5 wt% indium and 10 wt% tin, melting point: -19 ^{o}C), and mercury (melting point: -38.8 ^{o}C) as one triboelectrification material. It is expected that, by using these liquid metals, the contact intimacy could be greatly enhanced since the liquid metals are shape-adaptive to the solid surfaces.[53,54]

7.4.1 Measurement of triboelectric surface charge density

Tang *et al.* develop the liquid-metal-based triboelectric nanogenerator (LM-TENG) using mercury for surface charge density measurement. The LM-TENG is composed of two parts, as schemed in Figure 7-5a. One part is a slice, composed of friction material and its induction electrode, and the other is the liquid metal. The friction material could be any insulating material with different electron-attractive ability compared to the liquid metal, such as polyimide (Kapton), polytetrafluoroethylene (PTFE), polyethylene terephthalate (PET), and so on. The induction electrode's one end is fully covered by the friction material, avoiding any shortcut between the induction electrode and the liquid metal.

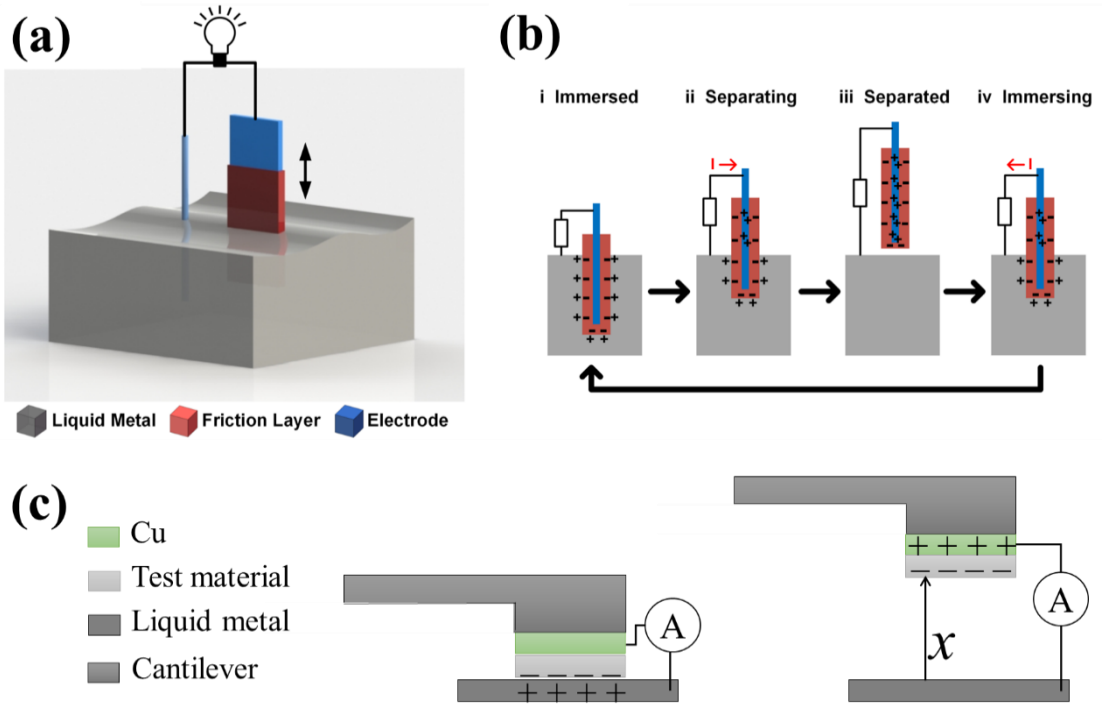

Figure 7-5. Methods of triboelectric surface charge measurement. (a) Schematic illustration showing the first method of measurement setup. (b) Step-by-step illustration showing the working principle of the first method of measurement. (c) The structure and the working principle of the second method of measurement. Reproduced with permission from Wiley[52] and Nature Publication Group.[47]

Figure 7-5b depicts the working principle of the LM-TENG step by step, which can be explained as a result of triboelectrification and electrostatic induction. When the slice is partly immersed into the liquid metal, the friction material makes contact with the liquid metal. Due to their different abilities in attracting electrons, the electrons will be injected from the liquid metal to the surface of the friction layer, so that there will be net negative charges on the surface of the friction layer and net positive charges on the interface of the liquid metal (Figure 7-5b-i). As the slice moves out of the liquid, the tribo-charges in the interface regions are separated, which will induce a higher potential in the liquid metal than the induction electrode; thus the electrons in the induction electrode will be driven to flow to the liquid metal through an external load (form a

current flow in the reverse direction, Figure 7-5b-ii). In this process, electrons keep flowing until the slice is fully taken out, which is represented by Figure 7-5b-iii. At this moment, both the induced potential difference and the amount of transferred charges between the induction electrode and the liquid metal reach the maximum values. As the slice moves back into the liquid metal, the potential difference will drop with the increase of the slice's wetting area. As a result, the electrons will flow back in the opposite direction from the liquid metal to the induction electrode (Figure 7-5b-iv). Thus, the entire process will result in an alternating-current pulse output. By using this method and assuming the short-circuit charge transfer is the total triboelectric charge created in the surface, the charge densities of different materials respect to mercury are measured as shown in Figure 7-6b.

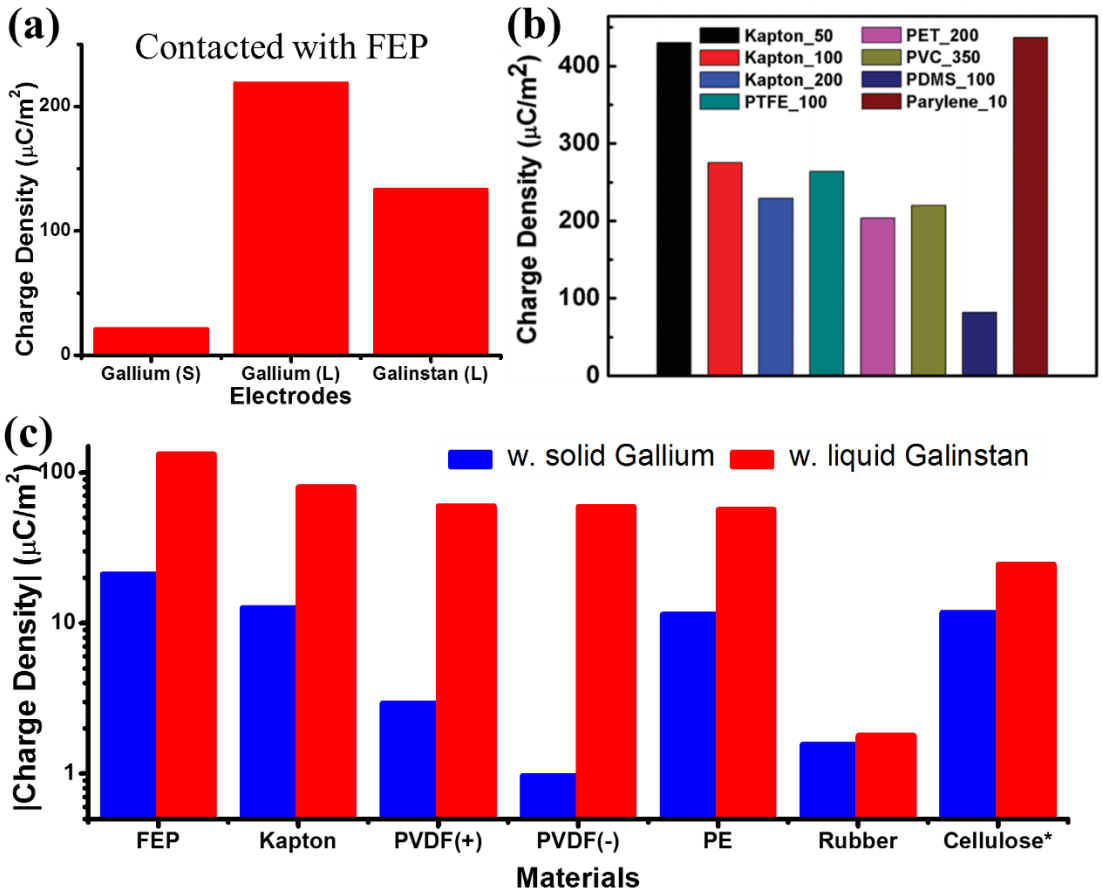

Figure 7-6. The standard σ measured by liquid metal as one electrode. (a) The charge density measured by contacting FEP with solid gallium, liquid gallium and galinstan; (b) The charge density measured by contacting different materials with mercury; (c) The absolute charge density measured by contacting different materials with solid gallium and liquid galinstan. Among them, cellulose was measured to be more positive than galinstan (as marked by *). Reproduced with permission from Wiley[52] and Nature Publication Group.[47]

We reported charge density measurement by liquid gallium and gallium alloy. Here the non-toxic liquid gallium and galinstan were utilized in experiments. To prevent them from being oxidized that would happen very fast for all the liquid metals containing gallium [53-56], the experiments were performed in a glove box with argon environment and the fixed condition of room temperature, 1 atm and 0.006% relative humidity (RH).

The setup of the measurement experiment is shown in Figure 7-5c. Firstly the tested material was deposited with Cu thin film as one electrode, and the liquid galinstan (from rotometals) or liquid gallium (from VWR) was used as the other electrode. When the material surface was contacted with the liquid metal surface, the charges were created on both the material and liquid metal surfaces by triboelectrification effect. And then, after the material along with the Cu electrode was lifted above the liquid metal surface for a height much larger (over 100 times) than the thickness of the materials, the charges induced by triboelectrification would be approximately fully transferred to the Cu electrode in short-circuit condition. The transferred charges were measured as the triboelectric charges, and then the charge density was calculated by the charges over the area of the triboelectrification surface. To make comparisons, solid gallium was also utilized to replace liquid metals as one electrode for charge density measurements. The good repeatability of charge transfer was observed during multiple contact-separation process. The tested materials included FEP, Kapton, polarized polyvinylidene fluoride (PVDF), polyethylene (PE), nature rubber, and cellulose. All of the measurement results are shown in Figures 7-6 a and c. When the tested material is more negative than the liquid metal, the measured charge density is recorded as a positive value; when the material is more positive than liquid metal, the measured charge density is recorded as a negative value (such as cellulose).

7.4.2 Quantified triboelectric series based on normalized charge density and dimensionless surface charge density

As we noticed from the results, the measured charge densities by contacting tested materials with a liquid metal are always larger than that by contacting the material with the corresponding solid metal. This is because with liquid metals used as one contact, the contact intimacy can be greatly enhanced. In fact, by using liquid mercury as the contact, even higher surface charge densities can be achieved.[52] The varied charge densities measured by contacting the same material with different liquid metals might be due to the different capabilities of the liquid metals to absorb the electrons. The triboelectric order as derived from our measurement is: (most negative) FEP-Kapton-PVDF-PE-Nature Rubber-Galinstan-Cellulose (most positive), which are consistent with existing triboelectric series as reported.[49] Triboelectric performance of each material can be standardly quantified using the triboelectric surface charge density with respect to a certain liquid metal. For example, the triboelectric performance of FEP can be quantified as $\sigma_{\text{FEP/galinstan}}$ = 133.24 μCm^{-2} with respect to galinstan, or $\sigma_{\text{FEP/Ga(L)}}$ = 218.64 μCm^{-2} with respect to liquid gallium. FEP (Teflon) is usually considered as the most triboelectric negative material; galinstan should be about in the middle position of the triboelectric series since it is close to nature rubber and it is more negative than cellulose. Therefore, we can consider the surface charge densities while contacting FEP with galinstan as the reference triboelectric charge densities. Then the normalized triboelectric charge density σ_{N} and dimensionless material figure-of-merit FOM_{DM} for triboelectrification (with respect to the charge density of FEP contacting with galinstan) can be defined as:

$$\text{FOM}_{\text{DM}} = {\sigma_{\text{N}}}^2 = \frac{{\sigma_{\text{Material/Galinstan}}}^2}{{\sigma_{\text{FEP/Galinstan}}}^2} \qquad (7.19)$$

Then the normalized triboelectric charge densities and dimensionless material FOM of measured materials are listed in Table 7.5. For a certain material, if $\sigma_{\text{N}} < 0$, then

the material is more positive than the reference liquid metal; if $0 < \sigma_N < 1$, then this material is more negative than the reference liquid metal and more positive than FEP; if $\sigma_N > 1$, then this material is more negative than FEP.

Table 7.5. σ_N and FOM_{DM} of different materials. These results are respect to the charge density of contacting FEP with galinstan.

Materials	Normalized triboelectric charge density	Dimensionless material figure-of-merit	Position in triboelectric series
FEP	1	1	Most –
Kapton	0.60	0.36	
PVDF	0.45	0.20	
PE	0.43	0.18	
Nature Rubber	0.0135	0.000183	
Galinstan	0	0	About middle
Cellulose	-0.185	0.0342	+

CHAPTER 8

INTEGRATED TRIBOELECTRIC NANOGENERATOR BASED SELF-POWERED SYSTEMS

In the above sections, we have discussed all the theoretical basis of TENGs, and now it is the time that we apply the optimization techniques and design the first integrated triboelectric nanogenerator based energy harvesting systems.[57] The system includes a TENG, a power management circuit, and a low leakage energy storage device. We perform system-level optimization to ensure the collaborative work of all the system components. Especially a power management circuit is designed to solve the impedance mismatch problem, which can achieve 90% board efficiency and 60% total efficiency, about two orders of magnitude improvement compared to direct charging. Driven by palm tapping, the power unit can provide a continuous DC electricity of 1.044 mW on average power in a regulated and managed manner (330 times improvement from previous work[58]) that can be universally applied as a standard power source for continuously driving numerous conventional electronics, such as a thermometer, a heart rate monitor (electrocardiograph/ECG system), a pedometer, a electronic watch, a scientific calculator, and a wireless radio-frequency communication system. We demonstrate the first power unit that utilizes widely accessible biomechanical energy source to sustainably drive a broad range of commercial mobile electronic devices.

This integrated human-motion driven self-powered system hierarchy is shown in Figure 8-1a, including a human-motion powered self-charging power unit and functional

circuits for different applications. The TENG scavenges the human biomechanical energy and converts it to AC electricity. Then this AC electricity is converted to a DC electric output that matches to the input of the energy storage unit by the power management circuit. Finally, the energy storage unit provides DC electricity to the whole functional circuits, including sensors, data processors, displays, and wireless transmitters. The signals from sensors and data processors are either visualized on an LCD displayer or sent out remotely through a wireless transmitter.

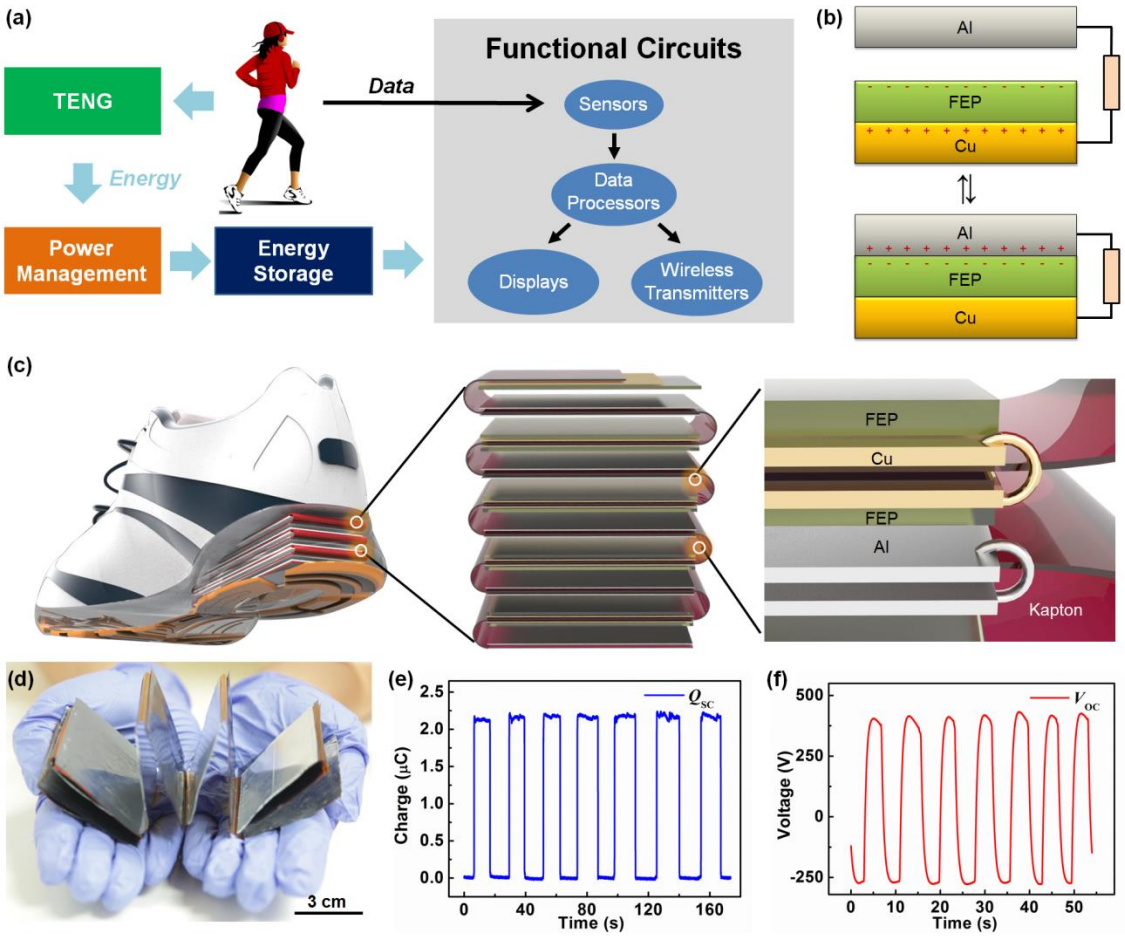

Figure 8-1. Structure design of a completely self-powered system that is driven exclusively by human biomechanical energy. (a) System diagram of a TENG-based self-powered system. (b) Working mechanism of an attached-electrode contact-mode TENG. (c) Structure of the designed multilayer TENG. (d) Photo of an as-fabricated TENG. (e-f) (e) Short-circuit current output and (f) open-circuit voltage output of the as-fabricated TENG. Reproduced with permission from Nature Publishing Group.[57]

The TENG is first designed and optimized to efficiently harvest human biomechanical energy. A multilayered attached-electrode contact-mode TENG is chosen to effectively collect the energy from human walking and running. The basic working principle of attached-electrode contact-mode TENGs is shown in Figure 8-1b, as discussed in Chapter 2. As shown in Figure 8-1c, a Kapton film is shaped into a zigzag structure with 10-15 layers. For each layer, a thin Aluminum foil and FEP (Fluorinated ethylene propylene) layer are utilized as the triboelectric materials. The Al foil also serves as one electrode. Copper is evaporated at the backside of the FEP layer as the other electrode. As shown in Figure 8-1d, the as-fabricated TENG has small volume and light weight (5.7 cm x 5.2 cm x 1.6 cm/29.9 g for a 10-layer TENG and 5.7 cm x 5.2 cm x 2.4 cm/43.6 g for a 15-layer TENG). Embedded in the shoe insoles, a human walking can drive this TENG to generate about 2.2 μC short-circuit transferred charge and about 700 V voltage output, as shown in Figure 8-1e and f.

From theoretical understanding of TENG charging characteristics discussed in Chapter 5, we designed the following charging strategy for maximized energy storage efficiency. First, a small temporary capacitor (C_{temp}) is charged by the TENG from 0 V. Once its voltage reaches V_{opt} (impedance match condition is reached), the energy stored in C_{temp} begins to be transferred to the final energy storage unit (a large capacitor or a battery) to maximize the theoretical total efficiency η_{total}. When the energy transfer finishes, the voltage of C_{temp} drops back to close to 0, and then C_{temp} is recharged by the TENG to reach V_{opt} again. With this optimized charging cycle, η_{total} can theoretically reach 75%.

This theoretical charging cycle can be realized by a two-stage power management circuit, as shown in Figure 8-2a. At the first stage, a temporary capacitor C_{temp} is charged by a TENG through a bridge rectifier. The second stage is for energy transfer from C_{temp} to the final energy storage unit. Since transferring electrostatic energy directly from a small capacitor to a large capacitor (or a battery) results in huge energy loss, two automatic electronic switches (controlled by a logic control unit, the power of both switches and their logic control unit is supplied from the final energy storage unit) and a coupled inductor are utilized in the second stage.[59] The detailed operation process is shown below to achieve efficient energy transfer in this stage. First, both the switches J_1 and J_2 are open to avoid interference of the charging process of C_{temp}. When V_{temp} reaches V_{opt}, the electronic switch J_1 closes. As a result, the energy starts to transfer from C_{temp} to inductor L_1 and V_{temp} starts to drop. When the energy is thoroughly transferred to L_1, the switch J_1 opens and J_2 closes. As a consequence, the current of L_1 falls to 0 instantaneously. Besides, since the total magnetic flux linkage in the coupled inductance cannot change abruptly, the current of L_2 will suddenly rise up, corresponding to the energy transfer from L_1 to L_2. Finally, the energy stored in L_2 will automatically transfer to the final energy storage unit because of the closure of J_2. When the energy stored in L_2 is thoroughly sent out, J_2 is open again and another charging cycle begins.

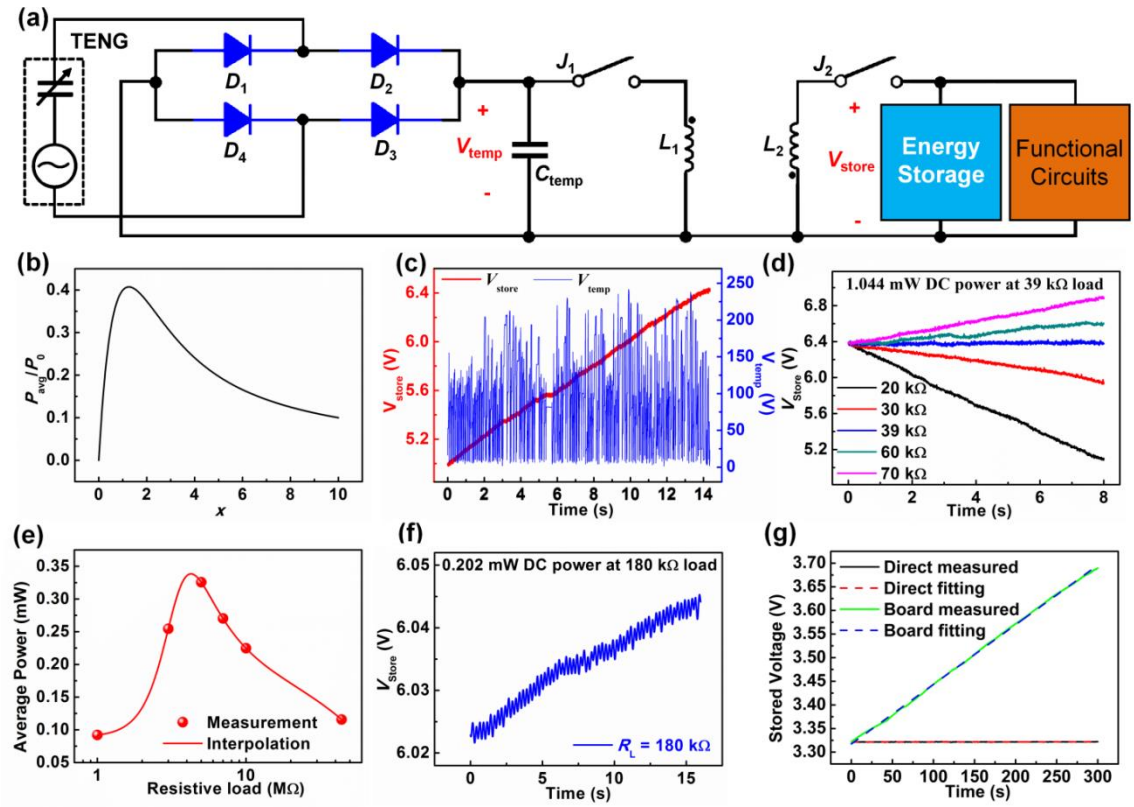

Figure 8-2. Design of the power management part for converting a "random" AC output from TENG to a regulated and managed power for directly driving electronics. (a) Circuit diagram of the power management circuit. (b) Theoretical calculation of the optimized charging time to demonstrate the design of the power management circuit. (c) Board efficiency measurement results. (d) Measurement of the maximum DC power of this system driven by human biomechanical energy. (e-f) Total efficiency measurement results. (e) Measurement of the AC harvested power from a resistor. (f) Measurement of the DC harvested power from the power management circuit. (g) Comparison of the charging current between direct charging and board charging. Reproduced with permission from Nature Publishing Group [57].

The operation of such a power management system is shown in Figure 8-2c-g. Figure 8-2c shows the voltage profiles of both temporary capacitor (V_{temp}) and final storage capacitor (V_{store}) when one 15-layer TENG and a 1 mF Al-electrolyte capacitor were utilized as the energy harvester and the energy storage unit (C_{store}), respectively. While the TENG is driven by palm tapping, C_{temp} is charged by the TENG and discharged through the energy transfer network, resulting in an oscillation of V_{temp} between 230 V

and 0 V. During the drop phase of V_{temp}, V_{store} is raised up by the transferred energy from C_{temp}. Note that if there was no mechanical energy input (from 5.4 s to 5.7 s in Figure 8-2c), both V_{temp} and V_{store} will decrease slowly because of the system leakage current and the power consumption of the electronic switches. The performance of the energy transfer network can be evaluated by the board efficiency (η_{board}), which is defined as the ratio of the total energy stored in C_{store} to the total energy transferred out from C_{temp}. From the data shown in Figure 8-2c, the total energy sent out from C_{temp} is calculated as 9.160 mJ, while the total energy stored in C_{store} is calculated as 8.243 mJ. So this energy transfer network has η_{board} = 90.0%, which is hugely improved in comparison to that of one-step direct energy transfer process.

To measure the DC power delivered to the load by the system as driven by palm tapping, a load resistor R_L is connected in parallel with the storage capacitor. The storage capacitor C_{store} is charged by two 15-layer as fabricated TENGs and then provides DC power for R_L. As shown in Figure 8-2d, when R_L is high, the power consumption of R_L is lower than the power provided by TENG, so V_{store} has a positive slope with time. As the load resistance R_L decreases, the load power consumption increases and the charging slope of V_{store} decreases. When the charging slope reduces to 0 (39 kΩ in Figure 8-2d), the power delivered from palm tapping is the same as the power consumed on the load, which is calculated as 1.044 mW (7.34 Wm^{-3}). When R_L continues to decrease (20 kΩ), the power delivered from palm tapping is not enough to compensate the energy consumption on the load, and the charging slope becomes negative.

The most important parameter of the power management circuit is the total efficiency η_{total}, which is defined as the ratio of the maximum DC power stored into the

storage unit to the maximum AC power delivered to a resistive load. To measure η_{total}, first the maximum AC power delivered to a resistive load can be extracted by the TENG resistance matching measurement. As shown in Figure 8-2e, the maximum AC energy generated by TENG is 0.3384 mW at an optimum load resistance of 4.26 MΩ. Second, the maximum DC power delivered through the power management board can be measured using the method shown above, which is 0.2023 mW (Figure 8-2f) under the same mechanical triggering (from an electric motor). Therefore, η_{total} is calculated as 59.8%.

Compared with direct charging, the power management board shows a huge enhancement of the charging efficiency. In another supercapacitor charging experiment, the net supercapacitor charging current is 13.82 nA through direct charging and 15.14 μA through the designed power management board, which is improved by as high as 1096 times! Note that a transformer shows even worse performance than direct charging. Under the same experimental condition, the charging current of a supercapacitor cannot even compensate the leakage current when a 10:1 transformer is utilized as the impedance match network.

This human-motion charged power unit have wide applications in realizing self-powered human-activity sensors, which makes them self-sufficient without any external power sources. Several applications have been demonstrated by utilizing this self-charged unit to sustainably drive various commercial electronic systems (Figure 8-3a). In the first demo, this human-motion charged power unit was connected to a commercial temperature sensor (Figure 8-3b). This temperature sensor utilizes a thermal couple to sense the external environment temperature. Then the sensing analog signal is digitalized

through an analog-digital converter (ADC). Finally, the digital signal is shown on a LCD display to fulfill the visualization of the output. Even under very gentle 1.6 Hz palm tapping (palm tapping is utilized mainly for easier filming purpose, other kinds of human-motion, such as foot tapping is also suitable for the application), this human-motion charged power unit could supply enough power to maintain continuous operation of the temperature sensor. There were not any external power sources/batteries inside to power any parts of the whole functionalized system.

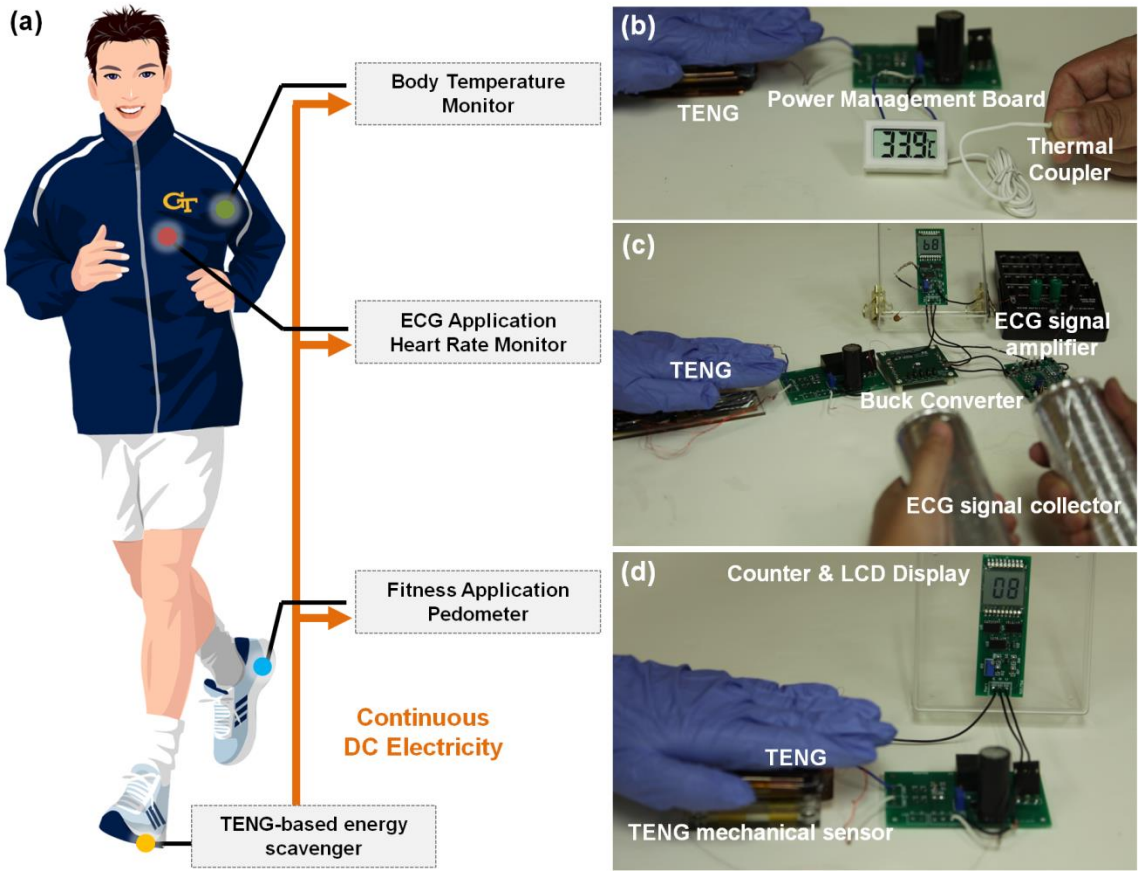

Figure 8-3. Application of this self-charging unit in self-powered wearable human activity sensors. (a) System configuration of self-powered human activity sensors. (b) Demonstration of a self-powered temperature sensor. (c) Demonstration of a self-powered heart-rate monitor (ECG) system. (d) Demonstration of a self-powered pedometer. Reproduced with permission from Nature Publishing Group [57]

This kind of power unit can also serve as power source for human health monitoring. As a typical example, we realized a self-powered electrocardiograph system (ECG system, Figure 8-3c). The bioelectricity signal across human left-hand and right-hand was first collected through the ECG signal collector (two conducting Al rods), and then amplified and filtered through an ECG signal amplifier (AD8232, Analog devices). After that, an ADC was utilized to convert the analog signal to digital signal, which was then captured by a digital counter. Finally the output of the digital counter was shown on the LCD display to visualize the signal. Besides, a buck converter was utilized to solve the supply voltage mismatch between the ECG signal amplifier (2 V - 3.3 V) and the LCD display (>4.5 V).[59] The number on the LCD display increased by 1 every time the heartbeat. At the same time, the storage capacitor voltage maintained a positive slope, which showed that the power provided from palm tapping was high enough to power the whole ECG system.

This kind of mechanical power source is also capable of being utilized in various fitness applications. For example, a self-powered pedometer system was realized (Figure 8-3d). In this system, the mechanical sensing part was realized by another attached-electrode TENG. When pressure was applied, this attached-electrode TENG could generate a voltage peak, which made this mechanical sensor consume zero electric power. Similar to the above heart rate signal, this voltage peak signal can be captured by an ADC and a digital counter and then visualized on the LCD display. The number on the LCD display increased by 1 every time pressure was applied on the mechanical sensor. Besides, while the pedometer maintained its normal function, V_{store} increased quickly

from the initial value of 5.02 V to 5.67 V. This fast increase is from the ultralow system power consumption due to the utilization of the self-powered TENG mechanical sensor.

Besides the self-powered human-activity sensors, this kind of mechanical power unit also has broad applications for other personal electronics. First, its application in wearable electronics is demonstrated through a self-powered wearable watch with mathematical calculation function (Figure 8-4a). A very slow and gentle palm tapping (1 Hz) could drive this wearable watch with full functionality: accurately recording time and calculating square root as an example. Under even irregular palm tapping (have irregular interval between the palming), this wearable watch still remains its normal function as long as the average power provided by human motion is larger than its power consumption. In addition, more complicated data processing work can also be finished with the power provided by palm tapping. For example, a scientific calculator is a commonly-used complicated data-processing system, containing clock generators, registers, read-only memories (ROMs), arithmetic logic units (ALUs), and a LCD display (Figure 8-4b). Such an advanced scientific calculator could be easily powered by the mechanical energy from palm tapping. All of the advanced calculation, such as trigonometric function, exponent function and logarithm function could be realized without existence of any batteries. Finally, this power unit is applicable in wireless communication system as well. As a typical demo, a remote keyless entry (RKE) module was connected with this power unit and utilized to wirelessly control a car that was about 50 meters away. The RKE module is a complicated radio-frequency system, mainly containing a microcontroller and a radio-frequency transmitter (Figure 8-4c). Once the button on the RKE module is pressed, the microcontroller processes and encrypts the

signal and transfers the encrypted 64 – 128 bit data to the radio-frequency transmitter. Then the 433.92 MHz radio-frequency transmitter can send out the code remotely with a data transfer rate about 2 – 20 KHz. This power unit could charge the storage capacitor from 5.9 V to 6.4 V in about 3 – 5 seconds. Once the storage capacitor's voltage reached 6.4 V, this RKE unit could functionalize and send out the encrypted signal and the storage capacitor's voltage went back to about 5.9 – 6.2 V. After receiving this radio-frequency signal, the receiver inside the car could process, decode, and respond to this command (unlocking its door and lighting up its low beam light), clearly showing the success of remote wireless transmission. Then the storage capacitor was charged by this power unit to reach 6.4 V again.

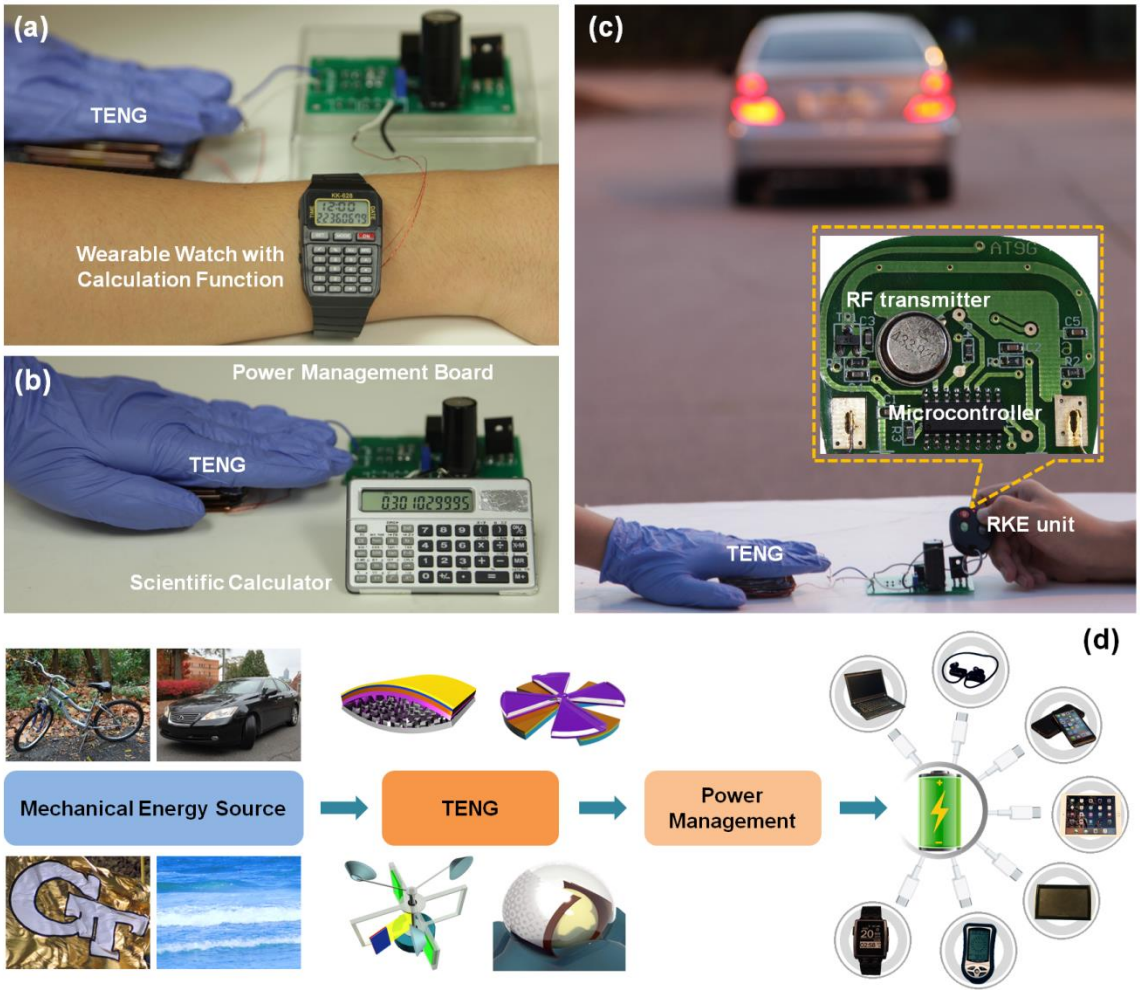

Figure 8-4. Application of the self-charging unit in self-powered data processing and transmission system. (a) Demonstration of a self-powered wearable watch and calculator. (b) Demonstration of a self-powered scientific calculator. (c) Demonstration of a self-powered remote keyless entry system. (d) Extension of this TENG-based self-charging unit for various applications as a universal adaptable power source. Reproduced with permission from Nature Publishing Group [57].

The demos presented above have covered all of the fundamental parts of mobile and wearable systems, including sensors, microcontrollers, memories, arithmetic logic units, displays, and even wireless transmitters, which have broad applications in personal sensor systems and internet of things. Besides human biomechanical energy, this kind of designs and concepts can also be extended to other mechanical energy sources, such as rolling wheels, moving cars and trains, blowing wind, and surging waves, by applying

various available TENG designs. If high frequency mechanical agitations are utilized to drastically improve the TENG output power, such system will have a potential to serve as a universal standard power source for sustainably driving more complicated electronic system, including smart watches, cellphones, navigation system, tablets, personal computers, and sensor nodes in internet of things (Figure 8-4d).

CHAPTER 9

CONCLUSION

In the previous chapters, I have presented my main research about the fundamental triboelectric nanogenerator theory and integrated triboelectric nanogenerator based self-powered system. My major goal is to solve the existing limitation of the nanogenerator technology for harvesting the ambient mechanical energy. And to understand this limitation, I first unveil the fundamental theory and simulation method for triboelectric nanogenerators, which introduces the complex coupling between electrostatic induction and circuit simulation. Then based on this fundamental theory, I developed the optimization technologies to improve the output of triboelectric nanogenerators. Finally, I utilized all my developed optimization technologies into real triboelectric nanogenerator systems. Through careful optimization, the output characteristics improved nearly by 330 times. In this chapter, I will summarize my major research achievements, and several suggestions on future works are provided for those who will continue investigations in triboelectric nanogenerators.

9.1 Triboelectric nanogenerator theory and simulation method

Although triboelectric nanogenerators are invented by our group in 2012, a systematical understanding of the core working mechanism is still not clear and their output characteristics have never been unveiled yet. Triboelectric nanogenerators are based on contact electrification and electrostatic induction. Therefore, they have inherent

capacitive behavior and their governing equation is their *V-Q-x* relationship. There are two capacitance formed between the tribo-charged dielectric surface and the two metal electrodes, respectively. The ratio of these two capacitances changes with the position of this dielectric surface, inducing electrons to transfer between the metal electrodes under short-circuit conditions. This is the core working mechanism of triboelectric generators. When triboelectric generators are connected with resistive loads, a "three-working-region" behavior is shown because of the impedance match between the generator and the load. Besides, when triboelectric generators are utilized to charge a capacitor with a bridge rectifier in multiple motion cycles, it is equivalent to utilizing a DC voltage source in series with an internal resistance to charge the capacitor. There also exists an optimum load capacitance that is linearly proportional to the charging time and an optimum charging voltage that is completely independent of load capacitance. Therefore, the optimizing TENG charging cycles is deducted, which is the theoretical basis of the first effective TENG power management circuit.

All fundamental modes of triboelectric generators are thoroughly analyzed to show their different output characteristics. The attached-electrode contact-mode and sliding-mode triboelectric nanogenerators need to maintain the minimum gap size to be much smaller than the effective dielectric thickness. The electrostatic shield effect of the primary electrode is the main design consideration of single-electrode triboelectric generators. Contact-mode freestanding triboelectric generators have superior linear characteristics and sliding-mode freestanding triboelectric generators have excellent height tolerance. For the most-complicated attached-electrode grating structure, increasing the number of grating units to get a finer pitch will generally improve the

output performance. However, when the pitch is very fine, the edge effect begins to dominate, resulting in degradation of performance when the number of units continues to increase. Thus, there exists an optimum number of grating units, and an optimum unit aspect ratio.

We also developed the standard and figure-of-merits for quantifying the TENG performance. Starting from the built-up voltage V – transferred charge Q plot, the CMEO with infinite load resistance was derived to have the maximized output energy per cycle, which represents the maximum energy production of TENG, similar to the Carnot cycle in heat engines. Based on the maximum output energy per cycle, and considering both the maximized energy conversion efficiency and the maximized average output power, the performance figure-of-merit (FOM) was derived to evaluate each TENG design, composed by a structural FOM and a material FOM. The structural FOMs for different structures of TENGs were simulated by analytical formulas and FEM, respectively, showing the maximum value of structural FOM for each TENG structure. The standard evaluation of the material FOM was also demonstrated by measuring triboelectric surface charge density via contacting the materials with liquid metals, and then the normalized triboelectric charge density and dimensionless material FOM were defined and derived for various materials.

9.2 Development of the first integrated triboelectric nanogenerator based self-powered system

Prior to my research, although there are several triboelectric nanogenerator based self-powered system existing. Since they just directly put the triboelectric nanogenerator

and energy storage element together, the output characteristics is not optimized and the DC power output is only 3 μW even under 10 Hz motor-driven mechanical motion, which is still far away from any practical applications. In my research, utilizing all the previously-designed theoretical method and optimization techniques, I have developed the first genuine self-powered system to meet mW requirement of personal electronics. The system includes a TENG, a power management circuit with 60% total efficiency, and a low leakage energy storage device. Our power management circuit provides the total efficiency that is about two magnitudes higher than the traditional direct charging. And the total system performance is 330 times higher than the state-of-art designs. Driven by palm tapping, this power unit can provide a continuous DC electricity of 1.044 mW on average power in a regulated and managed manner that can be universally applied as a standard power source for continuously driving numerous conventional electronics, such as a thermometer, a heart rate monitor (electrocardiograph/ECG system), a pedometer, a wearable electronic watch, a scientific calculator, and a wireless radio-frequency communication system. Our study demonstrates the first power unit that utilizes widely accessible biomechanical energy source to sustainably drive a broad range of commercial mobile and wearable electronic devices. This self-charging unit is a paradigm shift towards infinite-lifetime energy sources that can never be achieved solely by batteries.

9.3 Future works

Although huge advancements have been made in my research for this triboelectric nanogenerator technology, there exists some problem that remains to be solved to make. To assist future research, the suggested investigation topics are summarized as follows.

1. The theoretical basis of triboelectric effect/contact electrification still needs investigation. Experiments have shown that when two materials contact with each other, there will be charge transfer between them. However, the underlying physics of this phenomenon is still not clear, which limits the material optimization of this triboelectric nanogenerator technology. We should continue doing this and use this as an guideline to find two materials that can generated highest triboelectric charges.

2. For the theoretical modeling, the 2nd-order effect should be considered that can help to understand even more for triboelectric nanogenerators. In my research, I mainly provide the 1st-order equivalent circuit model for triboelectric nanogenerators. However, the 2nd-effect, including the parasitic resistance and capacitance may have an influence on the output characteristics that requires further investigation.

3. Advanced material is required to increase the triboelectric charge density. Since the power density of triboelectric nanogenerators is proportional to the square of tribocharges density. So it is hugely important to find materials that can provide the highest possible number. Also, surface treatment technology is important to further improve the power density of the device to make it even close to practical applications.

REFERENCES

1 Goldemberg, J. Ethanol for a sustainable energy future. *Science* **315**, 808-810, (2007).

2 Li, G. *et al.* High-efficiency solution processable polymer photovoltaic cells by self-organization of polymer blends. *Nat. Mater.* **4**, 864-868, (2005).

3 Wang, Z. L. & Song, J. H. Piezoelectric nanogenerators based on zinc oxide nanowire arrays. *Science* **312**, 242-246, (2006).

4 Beeby, S. P. *et al.* A micro electromagnetic generator for vibration energy harvesting. *J. Micromech. Microeng.* **17**, 1257-1265, (2007).

5 Lo, H. W. & Tai, Y. C. Parylene-based electret power generators. *J. Micromech. Microeng.* **18**, 104006, (2008).

6 Suzuki, Y. Recent Progress in MEMS Electret Generator for Energy Harvesting. *IEEJ Trans. Electr. Electron.* **6**, 101-111, (2011).

7 Lal, A., Duggirala, R. & Li, H. Pervasive power: A radioisotope-powered piezoelectric generator. *IEEE Pervas. Comput.* **4**, 53-61, (2005).

8 Roundy, S. *et al.* Improving power output for vibration-based energy scavengers. *IEEE Pervas. Comput.* **4**, 28-36, (2005).

9 Fan, F. R., Tian, Z. Q. & Wang, Z. L. Flexible triboelectric generator. *Nano Energy* **1**, 328-334, (2012).

10 McCarty, L. S. & Whitesides, G. M. Electrostatic charging due to separation of ions at interfaces: Contact electrification of ionic electrets. *Angew. Chem. Int. Ed.* **47**, 2188-2207, (2008).

11 Horn, R. G. & Smith, D. T. Contact Electrification and Adhesion between Dissimilar Materials. *Science* **256**, 362-364, (1992).

12 Baytekin, H. T. *et al.* The Mosaic of Surface Charge in Contact Electrification. *Science* **333**, 308-312, (2011).

13 Zhu, G. *et al.* Triboelectric-Generator-Driven Pulse Electrodeposition for Micropatterning. *Nano Lett.* **12**, 4960-4965, (2012).

14 Wang, S. H., Lin, L. & Wang, Z. L. Nanoscale Triboelectric-Effect-Enabled Energy Conversion for Sustainably Powering Portable Electronics. *Nano Lett.* **12**, 6339-6346, (2012).

15 Zhu, G. *et al.* Linear-Grating Triboelectric Generator Based on Sliding Electrification. *Nano Lett.* **13**, 2282-2289, (2013).

16 Wang, S. H. *et al.* Sliding-Triboelectric Nanogenerators Based on In-Plane Charge-Separation Mechanism. *Nano Lett.* **13**, 2226-2233, (2013).

17 Lin, L. *et al.* Segmentally Structured Disk Triboelectric Nanogenerator for Harvesting Rotational Mechanical Energy. *Nano Lett.* **13**, 2916-2923, (2013).

18 Yang, Y. *et al.* A Single-Electrode Based Triboelectric Nanogenerator as Self-Powered Tracking System. *Adv. Mater.* **25**, 6594-6601, (2013).

19 Zhu, G. *et al.* Self-Powered, Ultrasensitive, Flexible Tactile Sensors Based on Contact Electrification. *Nano Lett.* **14**, 3208-3213, (2014).

20 Zhu, G., Chen, J., Zhang, T. J., Jing, Q. S. & Wang, Z. L. Radial-arrayed rotary electrification for high performance triboelectric generator. *Nat. Commun.* **5**, 3426, (2014).

21 Xie, Y. N. *et al.* Grating-Structured Freestanding Triboelectric-layer Nanogenerator for Harvesting Mechanical Energy at 85% Total Conversion Efficiency. *Adv. Mater.* **26**, 6599-6607, (2014).

22 Wang, S. H., Xie, Y. N., Niu, S. M., Lin, L. & Wang, Z. L. Freestanding Triboelectric-Layer-Based Nanogenerators for Harvesting Energy from a Moving Object or Human Motion in Contact and Non-contact Modes. *Adv. Mater.* **26**, 2818-2824, (2014).

23 Lin, L. *et al.* Noncontact Free-Rotating Disk Triboelectric Nanogenerator as a Sustainable Energy Harvester and Self-Powered Mechanical Sensor. *ACS Appl. Mater. Inter.* **6**, 3038-3045, (2014).

24 Niu, S. M. *et al.* Theory of Sliding-Mode Triboelectric Nanogenerators. *Adv. Mater.* **25**, 6184-6193, (2013).

25 Niu, S. M. *et al.* Theoretical study of contact-mode triboelectric nanogenerators as an effective power source. *Energy Environ. Sci.* **6**, 3576-3583, (2013).

26 Niu, S. M. *et al.* Theoretical Investigation and Structural Optimization of Single-Electrode Triboelectric Nanogenerators. *Adv. Funct. Mater.* **24**, 3332-3340, (2014).

27 Niu, S. M. *et al.* Simulation method for Optimizing the performance of an integrated triboelectric nanogenerator energy harvesting system. *Nano Energy* **8**, 150-156, (2014).

28 Stoer, J. & Bulirsch, R. *Introduction to numerical analysis*. 3rd edn, (Springer, 2002).

29 Niu, S. M. *et al.* Theory of freestanding triboelectric-layer-based nanogenerators. *Nano Energy* **12**, 760-774, (2015).

30 Saurenbach, F., Wollmann, D., Terris, B. D. & Diaz, A. F. Force Microscopy of Ion-Containing Polymer Surfaces - Morphology and Charge Structure. *Langmuir* **8**, 1199-1203, (1992).

31 Lee, L. H. Dual Mechanism for Metal-Polymer Contact Electrification. *J. Electrostat.* **32**, 1-29, (1994).

32 Zhou, Y. S. *et al.* Nanometer Resolution Self-Powered Static and Dynamic Motion Sensor Based on Micro-Grated Triboelectrification. *Adv. Mater.* **26**, 1719-1724, (2014).

33 Zhu, G. *et al.* A Shape-Adaptive Thin-Film-Based Approach for 50% High-Efficiency Energy Generation Through Micro-Grating Sliding Electrification. *Adv. Mater.* **26**, 3788-3796, (2014).

34 Niu, S. M. *et al.* Optimization of Triboelectric Nanogenerator Charging Systems for Efficient Energy Harvesting and Storage. *IEEE Trans. Electron Devices* **62**, 641-647, (2015).

35 Niu, S. M. & Wang, Z. L. Theoretical systems of triboelectric nanogenerators. *Nano Energy* **14**, 161-192, (2015).

36 Niu, S. M. *et al.* A Theoretical Study of Grating Structured Triboelectric Nanogenerators. *Energy Environ. Sci.* **7**, 2339-2349, (2014).

37 Li, Y., Li, Y. H., Li, Q. X. & Zi, Y. Y. Computation of electrostatic forces with edge effects for non-parallel comb-actuators. *J. Tsinghua Univ. (Sci. & Tech.)* **43**, 1024-1026, (2003).

38 Wang, S. H., Niu, S. M., Yang, J., Lin, L. & Wang, Z. L. Quantitative Measurements of Vibration Amplitude Using a Contact-Mode Freestanding Triboelectric Nanogenerator. *ACS Nano* **8**, 12004-12013, (2014).

39 Curzon, F. L. & Ahlborn, B. Efficiency of a Carnot engine at maximum power output. *American Journal of Physics* **43**, 22-24, (1975).

40 Giordano, N. *College Physics: Reasoning and Relationships*. (Cengage Learning, 2009).

41 Sebald, G., Lefeuvre, E. & Guyomar, D. Pyroelectric energy conversion: Optimization principles. *IEEE Trans. Ultrason., Ferroelect., Freq. Control*, **55**, 538-551, (2008).

42 Alpay, S. P., Mantese, J., Trolier-McKinstry, S., Zhang, Q. & Whatmore, R. W. Next-generation electrocaloric and pyroelectric materials for solid-state electrothermal energy interconversion. *MRS Bulletin* **39**, 1099-1111, (2014).

43 Tritt, T. M. & Subramanian, M. A. Thermoelectric Materials, Phenomena, and Applications: A Bird's Eye View. *MRS Bulletin* **31**, 188-198, (2006).

44 Rowe, D. M. *CRC Handbook of Thermoelectrics*. (Taylor & Francis, 2010).

45 Green, M. A. *Solar cells: operating principles, technology, and system applications*. (Prentice-Hall, 1982).

46 Nelson, J. *The Physics of Solar Cells*. (Imperial College Press, 2003).

47 Zi, Y. L. *et al.* Standards and figure-of-merits for quantifying the performance of triboelectric nanogenerators. *Nat. Commun.* **6**, 8376, (2015).

48 Cheng, G., Lin, Z.-H., Lin, L., Du, Z.-l. & Wang, Z. L. Pulsed Nanogenerator with Huge Instantaneous Output Power Density. *ACS Nano* **7**, 7383-7391, (2013).

49 Wang, Z. L. Triboelectric Nanogenerators as New Energy Technology for Self-Powered Systems and as Active Mechanical and Chemical Sensors. *ACS Nano* **7**, 9533-9557, (2013).

50 Wang, Z. L. Triboelectric nanogenerators as new energy technology and self-powered sensors - Principles, problems and perspectives. *Faraday Discussions* **176**, 447-458, (2014).

51 Burgo, T. A. L. *et al.* Triboelectricity: Macroscopic Charge Patterns Formed by Self-Arraying Ions on Polymer Surfaces. *Langmuir* **28**, 7407-7416, (2012).

52 Tang, W. *et al.* Liquid-Metal Electrode for High-Performance Triboelectric Nanogenerator at an Instantaneous Energy Conversion Efficiency of 70.6%. *Adv. Funct. Mater.* **25**, 3718-3725, (2015).

53 Chiechi, R. C., Weiss, E. A., Dickey, M. D. & Whitesides, G. M. Eutectic Gallium–Indium (EGaIn): A Moldable Liquid Metal for Electrical Characterization of Self-Assembled Monolayers. *Angew. Chem. Int. Ed.* **47**, 142-144, (2008).

54 Dickey, M. D. *et al.* Eutectic Gallium-Indium (EGaIn): A Liquid Metal Alloy for the Formation of Stable Structures in Microchannels at Room Temperature. *Adv. Funct. Mater.* **18**, 1097-1104, (2008).

55 Xu, Q., Oudalov, N., Guo, Q., Jaeger, H. M. & Brown, E. Effect of oxidation on the mechanical properties of liquid gallium and eutectic gallium-indium. *Physics of Fluids (1994-present)* **24**, 063101, (2012).

56 Tingyi, L., Sen, P. & Chang-Jin, K. in *Micro Electro Mechanical Systems (MEMS), 2010 IEEE 23rd International Conference on* 560-563 (IEEE, Wanchai, Hong Kong, 2010).

57 Niu, S. M., Wang, X. F., Yi, F., Zhou, Y. S. & Wang, Z. L. A universal self-charging system driven by random biomechanical energy for sustainable operation of mobile electronics. *Nat. Commun.* **6**, 8975, (2015).

58 Wang, S. H. *et al.* Motion Charged Battery as Sustainable Flexible-Power-Unit. *ACS Nano* **7**, 11263-11271, (2013).

59 Erickson, R. W. & Maksimović, D. *Fundamentals of power electronics*. 2nd edn, (Kluwer Academic, 2001).

VITA

SIMIAO NIU

SIMIAO NIU was born in Inner Mongolia, P. R. China. He works as a graduate research assistant in Material Science and Engineering at the Georgia Institute of Technology, under the supervision of Dr. Zhong Lin Wang. He earned his Master of Science degree in the School of Electrical and Computer Engineering at the Georgia Institute of Technology in August 2015 and Bachelor of Engineering degree in the Institute of Microelectronics at Tsinghua University in July 2011. His research interests include theoretical and experimental studies on: mechanical energy harvesting by triboelectric nanogenerators and high-performance piezotronic sensors based on piezoelectric nanowires. He has co-authored over 50 peer-reviewed journal publications on *Nature*, *Nature Photonics*, *Nature Communications*, *Advanced Materials*, *Nano Letters*, *Energy & Environmental Science*, etc. Simiao Niu has received several prestigious awards, including 2015 Material Research Society Graduate Student Silver Award, 2011 Tsinghua University Outstanding Bachelor Thesis Award, 2011 Beijing City and Tsinghua University Outstanding Bachelor Student Award, and 2010 Chinese National Scholarship.